

2014

## **Experimental assessment of expandable casing technology as a solution for microannular gas flow**

Darko Kupresan

*Louisiana State University and Agricultural and Mechanical College*

Follow this and additional works at: [https://repository.lsu.edu/gradschool\\_theses](https://repository.lsu.edu/gradschool_theses)



Part of the [Petroleum Engineering Commons](#)

---

### **Recommended Citation**

Kupresan, Darko, "Experimental assessment of expandable casing technology as a solution for microannular gas flow" (2014). *LSU Master's Theses*. 1265.

[https://repository.lsu.edu/gradschool\\_theses/1265](https://repository.lsu.edu/gradschool_theses/1265)

This Thesis is brought to you for free and open access by the Graduate School at LSU Scholarly Repository. It has been accepted for inclusion in LSU Master's Theses by an authorized graduate school editor of LSU Scholarly Repository. For more information, please contact [gradetd@lsu.edu](mailto:gradetd@lsu.edu).

EXPERIMENTAL ASSESSMENT OF EXPANDABLE CASING TECHNOLOGY AS  
A SOLUTION FOR MICROANNULAR GAS FLOW

A Thesis

Submitted to the Graduate Faculty of the  
Louisiana State University and  
Agricultural and Mechanical College  
in partial fulfillment of the  
requirements for the degree of  
Master of Science

in

The Department of Petroleum Engineering

by  
Darko Kupresan  
B.S., University of Belgrade, 2011  
May 2014

## ACKNOWLEDGEMENTS

I would first like to express my profound gratitude to Dr. Mileva Radonjic for her endless support, mentoring, guidance and utmost patience during the course of my studies. I thank my committee members Dr. Andrew Wojtanowicz, Dr. Mayank Tyagi and James Heathman for their help and guidance while serving on my thesis committee.

I thank all of my friends and colleagues from the Sustainable Energy and Environmental Research (SEER) group for their help and support during this research. I am immensely grateful to Shell E&P for sponsoring this project and the industry advisors: William Portas, Bruce Selby, Mounia Bensouda. Other members of Shell personnel whose help is greatly appreciated are Richard Littlefield, Rodney Pennington, David Brisco and Daniele di Crescenzo. I sincerely appreciate the resourcefulness of Gerry Masterman, Wayne Manuel, Chris Carver (LSU PERTT Lab), Janet Dugas, Jeanette Wooden (LSU Administrative Coordinators), Maureen Hewitt (LSU International Cultural Center Manager), Rick Young (LSU Rock Mechanics Lab), Roy Hernadnez and Roy Keller (LSU Facility Services), Paul Rodriguez (LSU Chemical Engineering Machine Shop), and Barry Savoy and Dan Colvin (LSU Mechanical Engineering Machine Shop). I also thank Tim Quirk (now with Chevron), Richard Dubois (Halliburton) and Bill Carruthers (LaFarge), for providing the necessary materials, Dr. Dongmei Cao (LSU Material Characterization Center), Dr. Kyungmin Ham and Dr. Amitava Roy (CAMD), and Wanda LeBlanc (LSU Geology and Geophysics Lab Researcher) for their help with material characterization.

Lastly, I would like to express my deepest gratitude to my parents, Slavko and Spomenka Kupresan, my brother Bojan and Nicole Mumphrey for their love and support.

## TABLE OF CONTENTS

ACKNOWLEDGEMENTS .....	ii
LIST OF TABLES .....	vi
LIST OF FIGURES .....	ix
NOMENCLATURE .....	xiv
ABSTRACT .....	xv
CHAPTER 1: INTRODUCTION .....	1
1.1 Background of Wellbore Integrity Issues .....	1
1.2 Objective .....	2
1.3 Methodology .....	3
CHAPTER 2: LITERATURE REVIEW .....	4
2.1 Wellbore Cements .....	4
2.1.1 The Role of Wellbore Cements .....	9
2.2 Microannular Gas Flow .....	10
2.2.1 Wellbore Integrity Issues .....	10
2.2.2 Sustained Casing Pressure .....	14
2.3 Expandable Casing Technology .....	18
2.3.1 Pipe Expansion (Plastic Deformation) .....	18
2.3.2 Solid Expandable Tubulars .....	20
CHAPTER 3: EXPERIMENTAL METHODOLOGY .....	24
3.1 Expansion Fixture .....	25
3.1.1 Hydraulic Power Unit .....	25
3.1.2 Control Switch .....	25
3.1.3 Hydraulic Cylinder .....	27
3.1.4 Upper and Lower Housing .....	27
3.1.5 Expansion and Retaining Mandrel .....	27
3.1.6 Load Cell .....	28
3.1.7 Expansion Cones .....	28
3.2 Composite Sample .....	29
3.2.1 Metal Components .....	29
3.2.2 Cement Slurry Design and Preparation .....	32
3.3 Measuring Devices .....	33
3.4 Microhardness Tester .....	34
3.5 Experimental Procedure .....	35
3.5.1 Expansion Fixture Assembly, Testing and Calibration .....	35
3.5.2 Expansion Experiments .....	36

3.5.3 Force Measurements, Stress and Pressure Calculations .....	40
3.5.4 Post-expansion Investigation .....	41
3.5.5 Optical Microscopy.....	42
3.5.6 Thermogravimetric Analysis .....	42
3.5.7 Microhardness Test.....	43
3.5.8 Flow-through Experiments .....	46
CHAPTER 4: RESULTS .....	51
4.1 Visual Observations During and Post-expansion .....	51
4.2 Optical Microscopy.....	53
4.3 Thermogravimetric Analysis (TGA) of Cement.....	56
4.4 Microhardness Test.....	61
4.5 Mechanical Effects of Expansion on Pipe (Casing) .....	63
4.6 Gas Flow-through Experiments .....	65
4.6.1 Gas Flow-through Test I – Control Sample.....	66
4.6.2 Gas Flow-through Test II – 2% Expansion.....	67
4.6.3 Gas Flow-through Test III – 2% Expansion .....	69
4.6.4 Gas Flow-through Test IV – 4% Expansion .....	70
4.6.5 Gas Flow-through Test V – 8% Expansion .....	71
4.6.6 Gas Flow-through Test VI – 8% Expansion .....	73
CHAPTER 5: DISCUSSION.....	75
CHAPTER 6: CONCLUSIONS AND RECOMMENDATIONS .....	82
6.1 Conclusions.....	82
6.2 Recommendations.....	83
REFERENCES .....	84
APPENDIX A.....	89
APPENDIX B .....	93
B.1 Gas Flow-through Test II – 2% Expansion .....	93
B.2 Gas Flow-through Test III – 2% Expansion.....	96
B.3 Gas Flow-through Test IV – 4% Expansion .....	98
B.4 Gas Flow-through Test V – 8% Expansion.....	101
B.5 Gas Flow-through Test VI – 8% Expansion .....	103
APPENDIX C .....	106
APPENDIX D.....	107
APPENDIX E .....	110

APPENDIX F.....	113
APPENDIX G.....	114
APPENDIX H.....	115
APPENDIX I .....	116
VITA.....	117

## LIST OF TABLES

Table 2.1: Nine categories of API cement classification [13]. .....	8
Table 3.1: Dimensions of expansion cones.....	28
Table 4.1: Results of the ICP mass spectroscopy conducted on fluid samples collected during expansion at 4% and 8% expansion ratios. High concentrations of $K^+$ and $Na^+$ suggest that free cement pore water is being squeezed out of the sample. Large increase in concentration of $Ca^{2+}$ , $Fe^{3+}$ , $Mg^{2+}$ and $S^{6+}$ with expansion ratio indicates dissolution of certain minerals within the cement. ....	51
Table 4.2: Microscopy images of cement sample’s horizontal thin sections pre and post-expansion (4% and 8% expansion ratio). Images of expanded samples showing collapse of large air voids (AB) and precipitation of portlandite (P) within the pores. Fractures (F) were also observed within the matrix as a result of stresses during expansion. ....	54
Table 4.3: Microscopy images of cement sample’s vertical thin sections pre and post-expansion (4% and 8% expansion ratio). Images of expanded samples showing collapse of the air voids and precipitation of portlandite crystals on the walls and within collapsed pores, as well as fracturing (F) of cement matrix. ....	55
Table 4.4: Temperature ranges with endothermal peaks of different minerals which can be found in cement [5]......	56
Table 4.5: Summary table (average) of the main numerical results for cement samples six days post-expansion. Hardness and Young’s modulus show decrease for all expansion ratios with 30% decrease being the highest for 4% and 8% expansion.....	62
Table 4.6: Summary table (average) of the main numerical results for cement samples six months post-expansion. Hardness and Young’s modulus show increase in hardness in all samples post-expansion. ....	62
Table 4.7: Expansion and pipe parameters. Decrease in the wall thickness and increase in OD/t affected the collapse rating, decreasing it up to 20% for the 8% expansion ratio. ....	63
Table 4.8: Force measurements obtained during pipe expansion and calculated axial stresses. Values are for expansions with pipe only ( $F_e$ , $\sigma_z$ – pipe) and for composite cement sample ( $F_e$ , $\sigma_z$ – sample). ....	64
Table 4.9: Gas flow-through experiments data. The time lag represents the time elapsed between recordings of the two transducers. Stabilized inlet ( $P_{in}$ ) and outlet ( $P_{out}$ ) pressures used in the calculation of effective permeability of the microannulus ( $K_{ef}$ ). After expansion with the 2% expansion ratio cone, the microannular flow of 2.11 D permeability was successfully remediated. The size of the microannulus (w) was found to have been 5 microns. ....	68
Table 4.10: Gas flow-through experiments data. The time lag represents the time elapsed between recordings of the two transducers. Stabilized inlet ( $P_{in}$ ) and outlet ( $P_{out}$ ) pressures used in the calculation of effective permeability of the microannulus	

( $K_{ef}$ ), the size ( $w$ ) of 5.2 microns. After expansion with the 2% expansion ratio cone, the microannular flow of 2.31 D permeability was successfully remediated. ....	70
Table 4.11: Gas flow-through experiments data. The time lag represents the time elapsed between recordings of the two transducers. Stabilized inlet ( $P_{in}$ ) and outlet ( $P_{out}$ ) pressures used in the calculation of effective permeability of the microannulus ( $K_{ef}$ ). After expansion with the 4% expansion ratio cone, the microannular flow of 0.14 D permeability was successfully remediated. The size of the microannulus ( $w$ ) was found to have been 1.2 microns. ....	71
Table 4.12: Gas flow-through experiments data. The time lag represents the time elapsed between recordings of the two transducers. Stabilized inlet ( $P_{in}$ ) and outlet ( $P_{out}$ ) pressures used in the calculation of effective permeability of the microannulus ( $K_{ef}$ ), with the size ( $w$ ) of 9.1 microns. After expansion with the 8% expansion ratio cone, the microannular flow of 7.04 D was decreased to 300 nD immediately after expansion. Gas flow-through tests 24 hours and 60 days after expansion showed complete seal of the microannular flow. ....	73
Table 4.13: Gas flow-through experiments data. The time lag represents the time elapsed between recordings of the two transducers. Stabilized inlet ( $P_{in}$ ) and outlet ( $P_{out}$ ) pressures used in the calculation of effective permeability of the microannulus ( $K_{ef}$ ), which had the size ( $w$ ) of 2.8 microns. After expansion with the 8% expansion ratio cone, the microannular flow of 0.66 D permeability was successfully remediated. ....	74
Table 5.1: A summary of the volume calculations of compressed cement. The cement sheath was expanded to a length of 11 in. (28 cm) and the largest volume of cement displaced by the pipe ( $V$ ) occurred during the 8% expansion (10% of the initial volume of the cement). ....	78
Table A.1: Detailed indentation results of the control sample. The hardness was highest on the third indent (middle of the cement sheath), while the lowest value was located on the outer pipe side of the cement sheath. ....	89
Table A.2: Detailed indentation results of the sample expanded with the 2% expansion ratio cone. The hardness was highest on the first indent (closest to the inner pipe side of the cement sheath), while the lowest value obtained was in the middle of the cement sheath. ....	89
Table A.3: Detailed indentation results of the sample expanded with the 4% expansion ratio cone. The hardness was highest on the first indent (closest to the inner pipe side of the cement sheath), while the lowest value obtained was on the second indent. ....	90
Table A.4: Detailed indentation results of the sample expanded with the 8% expansion ratio cone. Hardness was highest on the fifth indent (closest to the outer pipe side of the cement sheath), while the lowest value was obtained in the middle of the cement sheath. ....	90
Table A.5: Detailed indentation results of the sample six months post-expansion at 2% expansion ratio. The hardness was highest on the fifth indent (closest to the outer pipe side), while the lowest value obtained was in the middle of the cement sheath. ....	91



Table A.6: Detailed indentation results of the sample six months post-expansion at 4% expansion ratio. The hardness was highest on the third indent (middle of the cement sheath), while the lowest value obtained was on the outer pipe side of the cement sheath. ....	91
Table A.7: Detailed indentation results of the sample six months post-expansion at 8% expansion ratio. Hardness was highest on the fourth indent (middle of the cement sheath), while the lowest value was obtained on point closest to inner pipe side of the cement sheath. ....	92
Table E.1: Results of force and stress calculations during expansion of the composite sample. Contact force and stress ( $F_c$ , $\sigma_c$ ) are used in calculations of radial force and stress ( $F_r$ , $\sigma_r$ ). ....	111
Table E.2: Results of force and stress calculations during expansion of the inner pipe only. Contact force and stress ( $F_c$ , $\sigma_c$ ) are used in calculations of radial force and stress ( $F_r$ , $\sigma_r$ ). ....	112
Table E.3: The difference in radial forces and stresses accounted for the cement sheath behind the pipe. ....	112
Table H.1: Results of the used class H cement clinker analysis performed by LaFarge. ....	115

## LIST OF FIGURES

Figure 2.1: Pore size distribution for hydrated cement is determined by a w/c ratio and the degree of hydration [8]. Permeability and strength are influenced by larger pores (over 50 nm), while the smaller pores of under 50 nm are mostly influencing drying shrinkage and creep..... 6

Figure 2.2: Cross-section of 7-1/2-in. (19.05 cm) casing cemented in 9-5/8-in. (24.5 cm) casing. Fractures and debonding observed after pressure and thermal cyclic loads [20]. ..... 11

Figure 2.3: True stress-strain curve of metals with effects of loading and unloading. Expansion region represents the stress-strain curve during pipe expansion. Graph showing material under loading beyond elastic limit (yield point, B). During reloading, new yield point (F) is reached and with further loading, the stress–strain curve proceeds along FG, virtually as a continuation of the curve BC (adapted from Chakrabarty, 2006). ..... 18

Figure 2.4: Installation sequence for Expandable Openhole Liner System. Expandable cone is run with the liner in the open hole and pulled after primary cement job. Pulling of expansion mandrel expands the pipe all the way to the hanger joint, latching it into place [62]. ..... 22

Figure 3.1: Schematic of experimental fixture and auxiliary equipment (not to scale). Hydraulic power unit is powered by turning the switch of the power source. Control switch controls hydraulics and operates the hydraulic cylinder which results in retaining or extending the expansion mandrel. Integrated load cell, which measures axial forces during expansion, is located between the piston rod of the hydraulic cylinder and the expansion mandrel. Force measurements are recorded and monitored in real time with the data acquisition system. The expansion cone is placed onto the end of the expansion mandrel and held in place with the retaining mandrel. Upper, middle and lower connector hold the assembly of the expansion fixture together (3D image of the expansion fixture courtesy of Paul Rodriguez, LSU). ..... 26

Figure 3.2: a. expansion cones with 2%, 4% and 8% expansion ratio; b. side view of 2% expansion ratio cone. All cones have 14° cone angle and are made from AISI D2 grade alloy steel which was heat treated to the hardness of 60 RC. .... 29

Figure 3.3: Composite sample schematic. Top view shows the cement (red color) between inner (a) and outer pipe (b). The arrow points the direction of expansion. Bottom view shows the steel plate ring (c) welded to outer pipe and pipe coupling. Inner pipe is screwed into the coupling (the scale is in inches)..... 30

Figure 3.4: Metal components of the bottom part of the composite sample:  
a. quarter-inch steel plate ring; b. 2.5-inch (6.35-cm) OD steel pipe coupling; c. pipe coupling welded onto steel plate ring; d. threaded part of the inner pipe being screwed into the pipe coupling; e. finished assembly. Final part of the composite sample is the outer pipe which is placed at the end and welded for the steel plate ring on the outer region. .... 31

Figure 3.5: a. 2D composite sample schematic. Expansion cone (shown in red) is pulled through the inner pipe, expanding its diameter and compressing the cement sheath (blue arrows point expansion direction). Pipe coupling, which was welded for the steel plate ring at the bottom of the composite sample, allowed screwing of the inner pipe into place. This pipe rotation enabled the inner pipe to be turned during first 24 hours of cement hydration in order to create the microannulus; b. 3D composite sample schematic showing the microannulus (red color, not to scale). ..... 37

Figure 3.6: Setup and expansion process (front view). a. the expansion mandrel is retained (white arrow showing direction) in order to clear the lower housing for placement of the composite sample; b. the composite sample is placed in the lower housing and the expansion mandrel is fully elongated (black arrow showing direction) through the inner pipe; c. the expansion cone is slipped onto the expansion mandrel and it is held in place with the retaining mandrel which is screwed onto the end of the expansion mandrel; d. the retaining mandrel guide is screwed into the lower connector to complete the assembly and the rig is ready for expansion (blue tape showing the expansion limit); e. the expansion mandrel is retained (white arrow showing direction) and the expansion cone is pulled through the inner pipe (end of expansion stroke). ..... 38

Figure 3.7: Setup and expansion process (top view): a. the expansion mandrel is retained (red arrow shows the direction) in order to clear the lower housing for placement of the composite sample; b. the composite sample is placed in the lower housing and the expansion mandrel is fully elongated through the inner pipe; c. the expansion cone is slipped onto the expansion mandrel. Magnified view shows the expansion cone being held in place with the retaining mandrel; d. the expansion mandrel is retained and the expansion cone is pulled through the inner pipe (red arrow shows the direction of expansion)..... 39

Figure 3.8: Hardness (H) and elastic modulus (E) are determined through load/displacement curve. A power-law fit through the upper third to half of the unloading data line intersects the depth axis at  $h_t$ . The stiffness S, is given by the slope of this line (adapted from Alexis Celestin)..... 44

Figure 3.9: Composite sample flow-through schematic. Bottom view shows manifold with Swagelok fittings and Teflon tubing. Cross-sectional view shows location of the inlet and outlet ports with respect to the pre-manufactured microannulus between the inner pipe and cement sheath. Epoxy was added to prevent nitrogen flow from venting to atmosphere. .... 48

Figure 3.10: Flow-through experimental setup. The flow meter (FM) controls nitrogen gas flow (red arrows) throughout the experiment. Gas flows and enters the composite sample on the inlet manifold where the inlet pressure transducer (PT-1) records the inlet pressure. Gas flows through the sample's pre-manufactured microannulus and the pressure recording on the outlet manifold's pressure transducer (PT-2) provides the information of whether there is a connectivity and microannular gas migration through the composite sample. Pressure transducers are connected to the data acquisition system (DAQmax) and pressures are monitored and recorded in real time on the computer screen (LabView software). Magnified view shows installation of the Swagelok fittings which were sealed by Teflon tape to prevent any

nitrogen leakage (gas flow-through composite sample schematic previously shown on Figure 3.5).....	49
Figure 4.1: Photo of a composite sample after expansion with the 8% expansion ratio cone. Fully hydrated cement, with a paste-like consistency, has been squeezed out from the holes on the outer pipe together with free cement pore water. The magnified view showing cement paste squeezed out from larger holes. ....	52
Figure 4.2: a. a cross-section of the composite sample immediately after 8% expansion exhibiting the cement sheath with softer consistency; b. drilled cement mini-cores from the composite sample were easily crushed under very small forces (between fingertips); c. a cross-section of the same composite sample five days after expansion. The cement regained its strength and there was no fracturing and deformation upon visual inspection. The width of the cement sheath was 0.51 in. (1.3 cm). ....	53
Figure 4.3: Plot of TGA for 7-month old control sample. The green (upper) line is showing weight percentage lost, while the blue line shows endothermal peaks (°C) of the weight percentage lost per unit of heat. In the range of 167-302°F (75-150°C), the total weight loss was 6.5%. This loss corresponds to the amount of moisture, and mineral phases of gypsum, ettringite and C-S-H in the sample. The next endothermal peak at 797°F (425°C) is portlandite peak. The weight loss of 5.7% indicates that there was initially approximately 23% portlandite in the control sample. Last endothermal peak at 1202°F (650°C) is calcite peak and small weight loss of 0.64% indicates minor presence of calcite. ....	57
Figure 4.4: TGA plot of cement sample after 2% expansion and six months of rehydration. The green (upper) line is showing weight percentage lost, while the blue line shows endothermal peaks (°C) of the weight percentage lost per unit of heat. The peak observed in the range of 167-302°F (75-150°C), correspond to the weight loss of moisture and mineral phases of gypsum, ettringite and C-S-H (9%). The portlandite peak at 788°F (420°C) showed weight loss of 5.77% indicating that there was approximately 23.6% portlandite in the sample expanded with 4% expansion ratio cone. Last endothermal peak at 1202°F (650°C), corresponding to the calcite peak, showed weight loss of 2.9%, indicating increased presence of calcite six months after expansion, compared to the control sample. ....	58
Figure 4.5: TGA plot of cement sample six months after 4% expansion. The green (upper) line is showing weight percentage lost, while the blue line shows endothermal peaks (°C) of the weight percentage lost per unit of heat. The distinctive peak observed in below 302°F (150°C), correspond to the weight losses of moisture (8%) and mineral phases of gypsum, ettringite and C-S-H (5%). The portlandite peak at 788°F (420°C) showed weight loss of 4% indicating that there was 17% portlandite in the sample expanded with 4% expansion ratio cone. Last endothermal peak at 1202°F (650°C), corresponding to the calcite peak, showed weight loss of 0.77%, indicating minor presence of calcite due to carbonation of the cement sample during preparation. ....	59
Figure 4.6: TGA plot for cement sample six months post-expansion at 8% expansion ratio. The green (upper) line is showing weight percentage lost, while the blue line	

shows endothermal peaks ( $^{\circ}\text{C}$ ) of the weight percentage lost per unit of heat. In the range of 167-302 $^{\circ}\text{F}$  (75-150 $^{\circ}\text{C}$ ), weight loss of 9.55% corresponds to the larger amount of moisture within the sample, and also mineral phases of gypsum, ettringite and C-S-H. The next endothermal peak at 788 $^{\circ}\text{F}$  (420 $^{\circ}\text{C}$ ) showed portlandite weight loss of 6% indicating initial concentration of 24%. Last endothermal peak at 1202 $^{\circ}\text{F}$  (650 $^{\circ}\text{C}$ ) showed 1.31% weight loss of calcite. .... 60

Figure 4.7: Indentation points of the cement sample. Indents range from the inner pipe side of the sample (Indent 1) to the outer pipe side of the sample (Indent 5)..... 61

Figure 4.8: Plot showing decrease in collapse and burst pressure ratings after expansion with 2%, 4% and 8% expansion ratio cones. Calculations of burst rating showed a decrease of 10% for the 8% expansion ratio, while the collapse rating decreased over 20% for the same expansion ratio. .... 64

Figure 4.9: Plot of axial forces recorded during expansion with 2%, 4% and 8% expansion ratio cones. The increase in forces during expansion of composite samples accounts for the presence of the cement sheath behind the pipe and transfer of stress into cement..... 65

Figure 4.10: Multi-rate gas flow-through test data plot recorded on control sample without pre-manufactured microannulus. After a gradual increase of 25 psi (172 kPa) in inlet pressure on the gas cylinder every five minutes from 25 psi (172 kPa) to 100 psi (690 kPa), there was no recorded pressure on the outlet pressure transducer, confirming that there was no microannular gas flow..... 66

Figure 5.1: Expansion experiment with pigmented cement. The left image is a magnified view of the cross-section at the interface between pigmented and regular cement. The red cement pore water propagated through the sample ahead of the cone and was observed in the paste squeezed out through the holes on the outer pipe (right magnified view). .... 75

Figure 5.2: An illustration of the expansion process (not to scale). The cement sheath images were obtained with X-ray computer tomography (CT) and processed to fit the schematic. a. the pre-expansion illustration shows microannulus between the inner pipe and the cement sheath; b. during expansion the cone is being pulled (arrow showing direction) and the cement sheath is being compressed behind the pipe, altering its structure; c. after expansion at 8% expansion ratio, the compressed cement sheath is shown without the microannulus. .... 77

Figure B.1: Gas flow-through test data plot pre-expansion showing registered pressures on the inlet and outlet pressure transducers. The starting inlet pressure on the gas cylinder was 15 psi (103 kPa), and the flow was kept constant in the period from 7-10 minutes of the flow-through test. The inlet pressure was increased to 50 psi (345 kPa), which resulted in a spike of both pressures on the inlet and outlet ports, confirming the microannular gas flow through the composite sample..... 93

Figure B.3: Multi-rate gas flow-through test data plot recorded immediately after expansion with the 2% expansion ratio cone. After a gradual increase of 25 psi (172 kPa) in inlet pressure on the gas cylinder every five minutes from 25 psi

(172 kPa) to 100 psi (690 kPa), there was no recorded pressure on the outlet pressure transducer, indicating successful remediation of the microannular gas flow. .... 94

Figure B.2: Gas flow-through test data pre-expansion semi-log plot showing the pressure differential ( $\Delta P$ ) between pressures recorded on the inlet and outlet pressure transducers. The pressure differential in the first case was shown to have a relatively larger value, which after calculations indicated a microannulus with an effective permeability of 2.11 D. .... 94

Figure D.1: Plot of TGA for control sample. The green (upper) line is showing weight percentage lost, while the red line shows endothermal peaks ( $^{\circ}C$ ) of the weight percentage lost per unit of heat. In the range of 122 $^{\circ}F$ -302 $^{\circ}F$  (50-150 $^{\circ}C$ ), the total weight loss was 6.5%. This loss corresponds to the amount of moisture, and mineral phases of gypsum, ettringite and C-S-H in the sample. The next endothermal peak at 797 $^{\circ}F$  (425 $^{\circ}C$ ) is portlandite peak. The weight loss of 5% indicates that there was initially 21% portlandite in the control sample. Last endothermal peak at 1191 $^{\circ}F$  (644 $^{\circ}C$ ) is calcite peak and small weight loss of 0.6% indicates minor presence of calcite due to carbonation of the sample. .... 107

Figure D.2: TGA plot of cement sample after 4% expansion. The green (upper) line is showing weight percentage lost, while the blue line shows endothermal peaks ( $^{\circ}C$ ) of the weight percentage lost per unit of heat. Two distinctive peaks observed in the range of 122-302 $^{\circ}F$  (50-150 $^{\circ}C$ ) correspond to the weight losses of moisture (8%) and mineral phases of gypsum, ettringite and C-S-H (5%). The portlandite peak at 790 $^{\circ}F$  (421 $^{\circ}C$ ) showed weight loss of 4% indicating that there was 17% portlandite in the sample expanded with 4% expansion ratio cone. Last endothermal peak at 1202 $^{\circ}F$  (650 $^{\circ}C$ ), corresponding to the calcite peak, showed weight loss of 0.77%, indicating minor presence of calcite due to carbonation of the cement sample during preparation. .... 108

Figure D.3: TGA plot for cement sample expanded at 8% expansion ratio. The green line is showing weight percentage lost, while the blue line shows endothermal peaks ( $^{\circ}C$ ) of the weight percentage lost per unit of heat. In the range of 122-302 $^{\circ}F$  (50-150 $^{\circ}C$ ), significant weight loss of 45% corresponds to the large amount of moisture within the sample, and also mineral phases of gypsum, ettringite and C-S-H. The next endothermal peak at 847 $^{\circ}F$  (453 $^{\circ}C$ ) showed portlandite weight loss of 3.2% indicating decrease of the mineral from 25% to 13% after expansion with 8% expansion ratio cone. .... 109

Figure E.1: Forces applied on the pipe during expansion.  $F_e$  represents the expansion force,  $F_c$  the contact force, and  $F_r$  the radial force. .... 110

Figure G.1: Sample preparation for cement thin sections and microindentation.  
a. cutting of the composite sample into disks; b. cut disk into quarters and removing the cement sheath out of the composite disk; c. orientation of the horizontal (top) cut for thin sections; d. orientation for side (vertical) thin section cut; e. five indentation spots for microhardness measurements. .... 114

## NOMENCLATURE

$\sigma_z$ – axial stress [psi, Pa]	$F_a$ – axial force [lbf, N]
$D$ – outside diameter [in, cm]	$d$ – inner diameter [in, cm]
$t$ – wall thickness [in, mm]	$Y_p$ – yield strength [psi, Pa]
$P_c$ – collapse pressure [psi, Pa]	$P_{br}$ – burst pressure [psi, Pa]
$q$ – nitrogen flow rate [Mcf/day, ml/min]	$A, B, C$ – empirical coefficients
$K_{ef}$ – microannulus effective perm. [D]	$r_{Iout}$ – outer diameter of inner pipe [ft, cm]
$r_{Oinn}$ – inner diameter of outer pipe [ft, cm]	$Z$ – gas deviation factor
$\mu$ – gas viscosity [cP]	$\Delta L$ – distance between P transducers [ft, cm]
$T$ – temperature [°F, °R, °C]	$P_{outlet}$ – outlet pressure [psi, Pa]
$P_{inlet}$ – inlet pressure [psi, Pa]	$P_{max}$ – maximum load [lbf, N]
$w$ – size of the microannulus (in, $\mu\text{m}$ )	$A_C$ – contact area [ $\text{in}^2$ , $\text{m}^2$ ]
$H$ – hardness (Vickers, MPa)	$h_{max}$ – maximum displacement [in, $\mu\text{m}$ ]
$A_C$ – projected contact area [ $\text{in}^2$ , $\text{m}^2$ ]	$S$ – stiffness
$h_C$ – contact depth [in, $\mu\text{m}$ ]	$\nu$ – Poisson coefficient of the sample
$E$ – Young’s modulus of the sample	$\nu_i$ – Poisson coefficient of the indenter
$E_i$ – Young’s modulus of the indenter	$E_r$ – reduced modulus

## ABSTRACT

Microannular gas flow in the wellbore is known to be one of the major reasons for Sustained Casing Pressure (SCP). Low success rate (under 50%) of costly remedial cementing operations and increasing difficulty in sealing off problematic areas motivated the industry to look for more practical remediation solutions. Expandable casing technology is one of those new proposed techniques.

A bench-scale physical model tested the potential of expandable casing technology for remediation of microannular gas migration. The composite samples with pipe-inside-pipe cemented annulus were designed to simulate a wellbore system including a pre-manufactured microannulus on the inner pipe/cement interface. Multi-rate flow-through tests with nitrogen gas first evaluated the permeability and the size of the pre-manufactured microannulus. The post-expansion flow-through experiments tested the ability of pipe expansion in sealing the microannular gas flow. The effects of expansion on properties and structure of the cement were investigated by microindentation, optical microscopy, thermogravimetric analysis (TGA) and inductively coupled plasma (ICP) mass spectrometry.

As observed with optical microscopy, the dissolution of unhydrated clinker grains during expansion is coupled with pore collapse within the cement sheath. Information obtained by microindentation showed that the cement sheath loses the integrity initially after expansion but regains most of the mechanical properties after a period of rehydration. Most important, multi-rate gas flow-through experiments showed that all three expansion ratios of 2%, 4% and 8% were successful in sealing the microannular gas flow. The seal was confirmed immediately and then 24 hours and 60 days after expansion.



The findings in this research give solid support to the potential of expandable casing technology for remediation of microannular gas migration. Cement pore water propagation is the most likely driving force behind a successful expansion, one that is not an obstacle in subsurface conditions and also makes an ideal environment for cement rehydration post-expansion. Cement integrity should not be compromised by pipe expansion after certain period of rehydration. Finally, the research showed that expansion technology could be used during all operations in vertical and horizontal wells, whether injection or production wells, to mitigate well leaks caused by gas migration.

## CHAPTER 1: INTRODUCTION

### 1.1 Background of Wellbore Integrity Issues

Adequate design and delivery of a cement system for well operations must produce a system that can withstand extreme stresses over time from spud to abandonment of the well, including, for example, perforating operations and the extreme pressures created by hydraulic fracturing.

Cement is an intricate construction component of a stable wellbore. Placed between the casing and the formation, the cement sheath's primary purpose is to provide an effective zonal isolation, which is essential for safe and economic field operations. This function depends on the optimum placement of the cement slurry, the design of the cement slurry, and its compatibility with the environment. An inadequate cement sheath can result in microannular gas flow, a chronic problem in a wellbore which interrupts production altogether for costly remedial cementing treatments. At worst, cement failure can indirectly cause total loss of the well and associated reserves.

Cement can undergo one or more failure mechanisms during the life of a well, from construction to abandonment, all possibly leading to well leakage-related problems. One of the first cementing problems is inadequate cement slurry design. Furthermore, poor cement slurry placement may occur during drilling operations if drilling fluid (mud) or drilling cuttings were not properly displaced from the wellbore before pumping cement. During well completion, when lightweight completion fluid replaces the drilling fluid, the negative pressure differential created can cause debonding at the casing-cement and/or cement-formation interfaces. The cement sheath must withstand the continuous impact of the drillstring during the drilling phase of the well construction, which is a particular

concern in directional wells. Production cycling in many deep, high-pressure/high-temperature (HPHT) wells can create extreme pressure and temperature events that increase the chance of cement sheath damage and eventual casing failure. Problems involving cement sheath failure occur also as a result of temperature- and pressure-induced stresses created by completion and well intervention operations such as perforating, hydraulic fracturing, and work-over. In addition, cement sheath design should address stresses created by the subsidence, especially in unconsolidated formations such as the Gulf of Mexico.

Causes for cement sheath failure and well leakage include gas flow through fractured cement sheath or through microannuli on either or both of the interfaces. Limits of cement evaluation technologies do not allow identification of a possible microannulus. That may give a false claim of good well condition after plugging and abandonment (P&A) operations, in which case unexpected leakage may occur in the near future or years later [1]. The average cost of plugging and abandoning the well is close to one million dollars [2], and most of these wells are plugged at the lowest possible cost following the minimum set requirements.

## **1.2 Objective**

The objective of this research was to provide an experimental approach to investigate the potential of expandable casing technology as a new remediation tool for microannular gas migration. The first goal was to design, develop, assemble, and calibrate a bench-scale expansion fixture (physical model) in order to accurately simulate tubular expansion under field-like conditions. The main objective was to successfully apply this physical model to research the ability of this technique to seal gas leakage through a

purposefully created microannulus. Gas migration has been identified as one of the main causes of Sustained Casing Pressure (SCP); recently reported by SPE to affect 30-35% of the wells globally.

### **1.3 Methodology**

The main part of the experimental methodology is the 30,000 lbf (133.5 kN) expansion fixture. This instrument, alongside custom-made expansion cones, was used to expand the 24-in. inner pipe of the cement composite sample. Class H LaFarage<sup>®</sup> cement, Halliburton D-Air 3000L<sup>™</sup> defoaming agent, bentonite, and deionized water were used in mixing of the cement slurry at a water-cement ratio of 0.87 to achieve the desired density of 13.1 lb/gal (1.57 g/cm<sup>3</sup>). This cement slurry design was used for cementing the composite samples. An integrated load cell was used in the recording of axial forces during expansion. These forces were then utilized in expansion stress analysis and pipe burst and collapse calculations. In order to reach the main objective, multi-rate flow-through experiments with nitrogen gas were run pre- and post-expansion on composite samples with pre-manufactured microannulus. The effective permeability of the microannulus was calculated using the linear Darcy flow equation for gas. Inlet and outlet pressure transducers recorded the pressure differential pre- and post-expansion, which was the main parameter in calculations of effective permeability; based on which the microannulus size was estimated.

## CHAPTER 2: LITERATURE REVIEW

### 2.1 Wellbore Cements

Wellbore cementing is a part of drilling and completion operations during the life of a well, and it can be classified as primary and secondary (remedial) cementing. Primary cementing involves pumping cement slurry into the annular space between the casing and the formation. The appropriate cement slurry design has to be selected to achieve the hydraulic seal between the cement-casing and cement-formation interface, while at the same time preventing fluid channeling. Secondary cementing is a process of placing a cement slurry into the wellbore under hydraulic pressure when remediation of an inadequate primary cement job is required. Plug cementing is an operation of secondary cementing and it involves placement of cement slurry at a desired part of the wellbore to create a plug or seal.

Most cements in the oil industry are Portland cements. They are a product of finely ground clinker, mainly consisting of a proportioned mixture of argillaceous and calcareous minerals [4]. After pulverizing and screening the raw materials, the mix is fed into a rotary kiln and heated to 2642°F (1450°C) to produce the cement clinker [5]. The typical clinker composition consists of about 67% CaO, 22% SiO<sub>2</sub>, 5% Al<sub>2</sub>O<sub>3</sub>, 3% Fe<sub>2</sub>O<sub>3</sub> and 3% of other components, and normally consists of four major minerals: alite (C<sub>3</sub>S), belite (C<sub>2</sub>S), aluminate (C<sub>3</sub>A) and ferrite (C<sub>4</sub>AF) [6].

Alite or tricalcium silicate (3CaO•SiO<sub>2</sub>), a critical mineral for strength development of Portland cement, makes 50-70% of cement clinkers and reacts quickly with water. Belite or dicalcium silicate (2CaO•SiO<sub>2</sub>) accounts for 15-30%, while aluminate or tricalcium aluminate (3CaO•Al<sub>2</sub>O<sub>3</sub>) constitutes 5-10% of Portland cement clinkers. These

components may cause undesirably rapid setting if gypsum is not added during the mixing process. Finally, ferrite phase or tetra-calcium aluminoferrite ( $4\text{CaO}\cdot\text{Al}_2\text{O}_3\cdot\text{Fe}_2\text{O}_3$ ) makes up 5-15% of Portland cement clinkers; its reactivity with water is initially high but very low in later years.

Mechanical properties, especially hardness and elastic modulus, of cement clinker phases have been previously determined with nanoindentation and documented in a paper by Velez et al. (2001) [7]. The elastic moduli of  $\text{C}_3\text{S}$ ,  $\text{C}_2\text{S}$ ,  $\text{C}_3\text{A}$ ,  $\text{C}_4\text{AF}$  were found to be similar and range between 125 and 145 GPa. The hardness of calcium silicate ( $\text{C}_3\text{S}$ ,  $\text{C}_2\text{S}$ ) and calcium aluminoferrite ( $\text{C}_4\text{AF}$ ) was similar (between 8 and 9.5 GPa), but lower than the hardness of  $\text{C}_3\text{A}$  (10.8 GPa).

When cement reacts with water it forms calcium-silicate-hydrate (C-S-H) ( $3\text{CaO}\cdot 2\text{SiO}_2\cdot 3\text{H}_2\text{O}$ ). This semicrystalline, nanoporous composite material with a large surface area can make up to 70% of hydrated cement paste and is the most responsible for cement strength. The second most common mineral in hydrated cement is calcium hydroxide, also referred to as portlandite ( $\text{Ca}(\text{OH})_2$ ); its concentration in hydrated cement paste is up to 25%. Its crystals form hexagonal plates of indeterminate shape that may be intimately intergrown with C-S-H [6].

In the third large mineral group in hydrated cements, the aluminoferrite group, the major mineral of this phase group is ettringite ( $\text{Ca}_6\text{Al}_2(\text{SO}_4)_3(\text{OH})_{12}\cdot 26\text{H}_2\text{O}$ ). Ettringite, which can make up to 20% of a hydrated cement paste, is formed in the early hydration stages, often presenting as hexagonal rods.

The permeability of neat fully hydrated cement pastes can range from the nanodarcy (nD) region, for cements with a water-cement ratio of 0.3 [8], to the millidarcy (mD) region for cement pastes with 0.7 water-cement ratio. The porosity of the hydrated cement paste obtained with mercury intrusion porosimetry was shown to have values from under 15% for cement pastes with 0.3 water-cement ratio [9], to over 40% for cement pastes with 0.7 water-cement ratio [10].

The pore size of the cement paste is usually determined by either mercury intrusion or nitrogen adsorption isotherms. The pore diameter in hydrated cement can range from several nanometers to a couple of hundred micrometers, which is associated with air bubbles created during cement mixing. Most of the capillary porosity in fully hydrated cement paste ranges from 10 to 100 nm, as shown in Figure 2.1 [8].

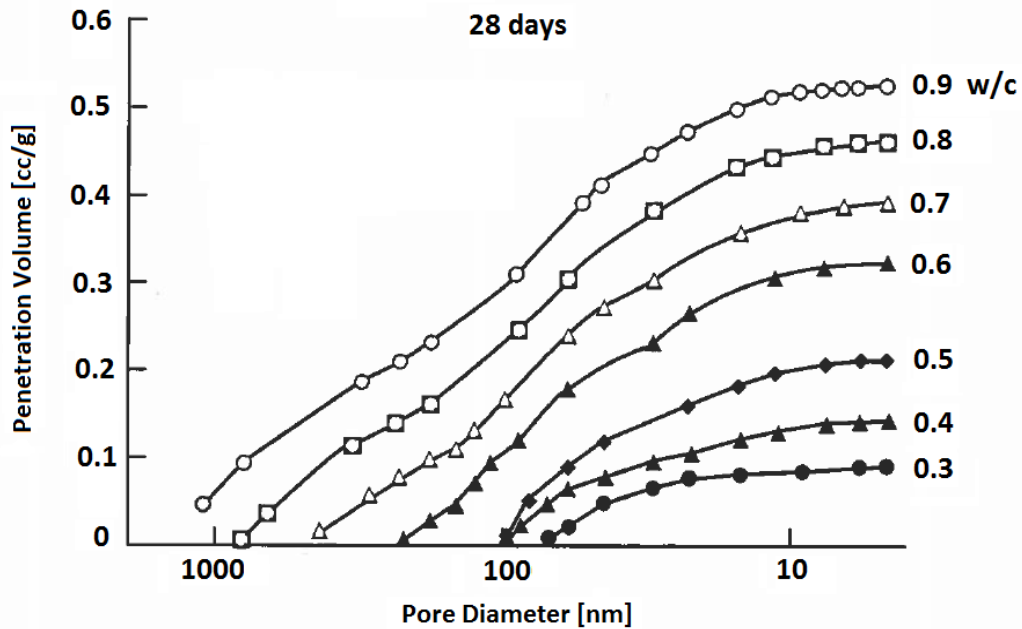


Figure 2.1: Pore size distribution for hydrated cement is determined by a w/c ratio and the degree of hydration [8]. Permeability and strength are influenced by larger pores (over 50 nm), while the smaller pores of under 50 nm are mostly influencing drying shrinkage and creep.

Mechanical properties of hydrated cement pastes such as hardness, are influenced by water to cement ratio. Glinicki and Zielinski (2004) documented a linear relationship between Vickers hardness and different w/c ratios using indentation [11]. Their results were that after 28 days, 0.3 w/c ratio hydrated cement paste had hardness of over 550 MPa, 0.5 w/c ratio cement paste had hardness of 375 MPa, while cement paste with highest w/c ratio of 0.7 produced hardness of 200 MPa, clearly showing an inverse relationship.

Entrapped air or gas can cause various problems during cementing operations, including lowering slurry density and inadequate cement mixing. Defoaming agents are chemicals which are added to cement slurries usually in small quantities, 0.1% to 0.3% by weight of cement (BWOC), with the purpose of removing most of the entrapped air and minimizing the foaming from the mixture [12]. These additives will not affect fluid loss, thickening time, or compressive strength.

API recommended practices classify cement into nine different categories (A through J, as shown in Table 2.1). These classifications of cement were made in order to optimize the slurries for hotter and deeper downhole conditions. The difference in cements lies in the fineness of the grind of the cement, in manufacturing additives, and impurities in the water. Class H cement, the most commonly used cement in the United States, is intended for use as a basic cement for depths of up to 8,000 ft (2440 m). Able to be used with accelerators and retarders, no additions other than calcium sulfate and water are added to it during the manufacturing process [13].



Table 2.1: Nine categories of API cement classification [13].

<b>API Cement</b>	<b>General Use</b>	<b>Temperature (neat cement)</b>
A	From surface to 6,000 ft (1830 m) depth, when special properties are not required.	Surface and shallow application
B	From surface to 6,000 ft (1830 m) depth, when conditions require moderate sulfate-resistance.	110°F (43°C)
C	From surface to 6,000 ft (1830 m) depth, when conditions require high early strength.	140°F (60°C)
D	From 6,000 to 10,000 ft (1830 to 3050 m) depth, under conditions of moderate HPHT.	170 to 230°F (77 to 110°C)
E	From 10,000 to 14,000 ft (1830 to 3050 m) depth, under conditions of HPHT.	230 to 290°F (110 to 143°C)
F	From 10,000 to 16,000 ft (1830 to 4880 m) depth, under conditions of extreme HPHT.	230 to 320°F (110 to 160°C)
G	As basic cement from surface to 8,000 ft (2440 m) depth as manufactured. More range with additives.	80 to 200°F (27 to 93°C)
H	As basic cement from surface to 8,000 ft (2440 m) depth as manufactured. More range with additives.	80 to 200°F (27 to 93°C)
J	From 10,000 to 16,000 ft (1830 to 4880 m) depth as manufactured, under conditions of extreme HPHT.	230 to 320°F (110 to 160°C)

Various cement designs with additives are used in certain challenging environments. Conventional Portland cement systems are not suitable for freezing conditions since they will freeze before developing sufficient compressive strength. Several types of cement design can be successful in this environment: gypsum-Portland cement blends with sodium chloride which develop strength rapidly at freezing temperatures [14]; calcium aluminate cements also develop strength rapidly, and fly ash is often added to reduce cement's heat of hydration [15]; ultrafine Portland cement which has an accelerated reaction rate due to greater surface area of the cement grains [16].

Diverse Blast Furnace Slag (BFS) cement systems are used for a variety of cementing applications in different environments. They can be used alone as a cementitious material or blended with Portland cement, often referred to as “slag cement” [3]. Among other applications, they can be used for squeeze cementing, salt-zone cementing, corrosive environments, HPHT wells, and steam injection wells. Slag cements are more resistant to sulfate attack, have slower diffusion of chloride through the cement matrix, and have lower set-cement permeability.

### **2.1.1 The Role of Wellbore Cements**

Complete and durable zonal isolation is the main goal of any good primary cement job and a stable wellbore. The cement sheath should also provide casing support and protect it from corrosive environments. For proper placement of optimum cement slurry, certain well parameters such as pressure, temperature, and formation type have to be obtained or estimated during the design process of well completion.

In order to achieve its major functions of isolating geologic structures from fluid migration, protecting the casing from corrosion, and providing the support for the weight of the casing, a hydraulic seal must be created on the cement/casing and cement/formation interfaces [3]. This impermeable seal is crucial for a stable wellbore during the entire drilling and producing life of the well.

To maintain wellbore integrity, placement of fluids and maximize the mud removal in the wellbore must be optimized, meaning that various cement slurry properties (mixability, rheology, thickening time, etc.) should be taken carefully into account. The cementitious material should withstand the various stresses occurring during the life of the well [17]. In order to provide total zonal isolation, the cement matrix should be free of any

channels, microannuli, or fractures. Unfortunately, in most cement jobs this is not the case and wellbore cements are linked to many types of problems and failures.

## **2.2 Microannular Gas Flow**

### **2.2.1 Wellbore Integrity Issues**

Wellbore cement sheaths are subjected to many types of failure, such as debonding at the cement-formation and cement-casing interface and fracturing/cracking of the cement matrix. According to Nelson & Guillot (2006), pressure and temperature oscillations caused by completion and production operations contribute to the development of fractures and microannuli within the cement matrix [3]. Debonding is caused by casing movement, gradual pressure decrease, and cement shrinkage, while incomplete mud removal can result in poor bonding of cement to the formation rock. Shear failure, the last type of failure, is caused normally by effective stress increase around the wellbore (rock subsidence and movement). If the cement is not allowed to set adequately before further drilling, cement integrity at the casing shoe might fail.

With usage of heavier mud for extended casing setting depth drilling, the migration of formation fluids through unset cement from high pressure to low pressure formation can create channels in the upper part of the open hole due to mechanisms such as fluid loss, slurry gelation, and bulk shrinkage. Cement integrity can also be damaged by pressurizing the casing in order to test the seal during drilling and completion operations; even a 2% expansion might be enough to create channels and cracks in the cement sheath.

Both tensile and shear failure of the cement sheath have been shown to have a strong relationship to wellbore pressure and wellbore temperature [18]. Cement fractures created due to the expansion of casing caused by internal pressures generally cause loss of

annular zonal isolation in the lower quarter to third of the well, while fracturing due to large temperature changes occurs in the upper third to half of the well [19].

Heathman and Beck (2006) created a model of conventionally cemented casing which was subjected to pressure and thermal cyclic loads while monitoring the integrity of the cement-casing bond [20]. A closer look at their model's cross-section after longitudinal pressure testing with water and nitrogen showed visible debonding and sheath cracks which clearly represent preferential pathways for migrating fluid (Figure 2.2).

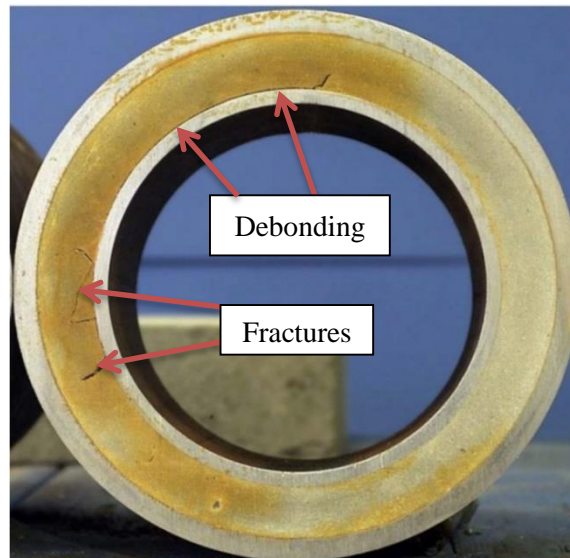


Figure 2.2: Cross-section of 7-1/2-in. (19.05 cm) casing cemented in 9-5/8-in. (24.5 cm) casing. Fractures and debonding observed after pressure and thermal cyclic loads [20].

Due to cement's low permeability, no significant gas flow can occur within the cement matrix unless there are preferential flow paths, degradation of the material, or the material was not formed properly during the emplacement process and hydration [21]. Boukhelifa et al. (2004) ran permeability tests through a mechanically manipulated cement sheath [22]. The cement sheath was placed between the central core, which would expand and compress, and the outer pipe under confined pressure of 43.5 psi (300 kPa). Among other findings, they observed that casing compression can create a microannulus and

significantly increase the cement sheath permeability, while casing pressurization can cause initiation of radial cracks in cement matrix once the tensile stresses exceeded the tensile strength of the material. Due to high Young's modulus and low tensile strength (compared to compressive strength), the cement sheath is more likely to fail in tension than in compression [23].

Bachu and Bennion (2009) measured an effective permeability of less than  $10^{-6}$  mD in the case of perfect bonding between cement and casing [24]. The effective permeability was five to six orders of magnitude higher, reaching 1 mD, once poor bonding between the cement and the casing was created intentionally and radial cracks and microannuli were induced. The most typical short-term effect, which is related to drilling and completion, is the creation of microannuli and channels filled with mud and gas [25]. Medium to long-term effects are related to completion and stimulation operations. There is an increase in methane emission due to increase in hydraulic fracturing operations, which may pose a great environmental risk and dictate future climate change [26].

Possible preferential leakage pathways in an existing producing or abandoned well include flow-paths along the cement-formation interface, along the cement-casing interface, and through degraded materials. Time is an important factor to take into account when analyzing cement degradation. Severe environmental consequences and well failures can occur if wells exceed their designed life [27]. Though there are certain old producing wells (over a century old) that have not leaked, HPHT, thermal-cycled, and corrosive environment wells may have a short well life of less than a decade before permanent P&A is required [28]. The main objective of well abandonment operations or well plugging is to prevent cross-flow between different horizons and, in particular, contamination of

groundwater resources [29]. If there are leaks, the abandonment operation is unsuccessful and poses an environmental risk and company liability.

The analysis conducted by Watson and Bachu (2009) of 315,000 oil, gas and injection wells in Alberta, Canada, also showed that wellbore deviation, well type, abandonment method, whether or not cement is present, and the quality of cement are the key factors contributing to, and are indicative of potential well leakage in the shallower part of the well [30]. Another study of a smaller fragment of 20,500 wells, showed 15% exhibited well leakage, out of which 14.5% were cased wells [31].

In his dissertation, Xu (2002) discusses how, besides channels within the cement matrix, the path between cement and casing or cement and formation (microannulus) and gas flow through cement matrix can be described as a linear gas flow with a changing rate at cement top and constant pressure at the gas-source formation [32]. There are different approaches to calculating/estimating the flow of gas through such imperfections. In order to quantify flow through the microannulus, Darcy's law for linear gas flow can be used. Equivalent permeability which can be related to the microannulus ( $K^*$ ) can be obtained from the following Equation 2.1 [33]:

$$K^* = \frac{1424q\mu ZT\Delta L}{\pi(r_w^2 - r_{cas}^2)} \cdot \frac{1}{(P_i^2 - P_{wf}^2)} \quad (2.1)$$

$q$  – flow rate [Mcf/day]

$r_{cas}$  – casing radius [ft]

$\mu$  – gas viscosity [cP]

$T$  – reservoir temperature [°R]

$P_i$  – reservoir pressure [psi]

$K^*$  – equivalent permeability [mD]

$r_w$  – well radius [ft]

$Z$  – gas deviation factor

$\Delta L$  – reservoir thickness [ft]

$P_{wf}$  – flowing bottom hole pressure [psi]

The approximate size of the microannulus ( $w$ ) can be obtained knowing the value of the equivalent permeability ( $K^*$ ) by the following correlation [33]:

$$K^* = 5.4 \cdot 10^{10} \cdot w^2 \quad (2.2)$$

$w$  – size of the microannulus (in.)      $K^*$  – equivalent permeability [mD]

The approximation of the slot size from permeability is correlated from Buckingham's equation which is shown in the Appendix F.

### **2.2.2 Sustained Casing Pressure**

Any of the aforementioned cement failures can result in flow paths as a form of conductive fractures or microannuli. Even a small microannulus can result in high effective permeability along the cement sheath allowing gas migration and the occurrence of Sustained Casing Pressure (SCP) at the wellhead. The microannulus width of  $4.3 \cdot 10^{-5}$  in. (1.1  $\mu\text{m}$ ) would correspond to an equivalent permeability of 120 mD [33]. If the well is shut in and remains at the same steady-state condition, then the casing pressure should remain zero. If the casing pressure returns when the choke valve is closed, then the casing is diagnosed with SCP, and in some cases the pressure can reach dangerously high values [34]. SCP occurs due to the loss of the well's external integrity, causing gas inflow from a high-pressure formation into the well's annulus. Xu (2002) discusses how gas migrates upward in the outer casing strings, outside of the production casing, through a leaking cement sheath and percolates through the mud column, accumulating above the liquid level [32].

One of the main parameters which indicates the quality of the cement job is its permeability, since it controls the early stage of SCP buildup rate, an overall measure of the annular seal performance of the well. Diagnostic testing is required in any well exhibiting sustained casing pressure and the results of the test determine if immediate SCP removal could be temporarily waived (departure permit) and continuing operation of the well permitted [35].

Studies from field operations in the Gulf of Mexico indicate that 56% of incidents that lead to a loss of well control are linked to cementing operations. Furthermore, approximately 45% of 14,927 operational wells in 2004 had SCP problems, and about 33% of the SCP problems were linked to the cementing process [36]. The casing strings which are most affected by SCP are production (50%) and surface (30%) casings [34].

Considerable numbers of producing and abandoned wells with SCP constitute a potential new source of continuous natural gas emission from failed casingheads due to poor cementing and external gas migration [37]. There are more than 27,000 abandoned oil and gas wells in the Gulf of Mexico. The oldest of the wells were abandoned in the late 1940s, raising the prospect that many deteriorating sealing jobs are already failing (AP). The Associated Press investigation further uncovered a particular concern with 3,500 of the neglected wells – those characterized in federal government records as "temporarily abandoned."

SCP may increase and become more hazardous over time as a result of such factors as: increasing microannuli on both interfaces, damage to primary cement caused by mechanical manipulations, thermal cracking caused by different expansion properties of



cement and casing, dissolution of cement in acidic formation brine, and condensation of hydrocarbons in the micro fractures [38].

When a well persists in exhibiting pressure buildup, it presents an extremely unsafe environment. Pressure changes during production might induce a failure of the production casing, which can lead to very dangerous situations. For instance, the outer casing strings, which are weaker than the production casing, may also fail, potentially resulting in an underground blowout of flow rate sufficient to jeopardize the production platform. According to Bourgoyne et al. (1999) the principle concern for wells that exhibit SCP is that a down-hole situation is developing or has developed the conditions which can result in an underground blowout, without always showing symptoms and warning signs [39]. Once casing diagnostic tests show that SCP exceeds the maximum allowable wellhead operating pressure (MAWOP), remediation operations are necessary by regulation [40].

Remedial cementing is an operation in which different designs of cement help in solving a variety of wellbore integrity problems. This operation can be divided into two major categories: plug cementing (usually used for abandonment) and squeeze cementing (mainly need to repair a poor primary cement job) [3].

When the SCP is diagnosed to have affected production and outer casing strings, the rig method usually involves the squeeze cementing operation. In order to perform these operations, a workover rig is required or, in some cases, a coiled tubing unit is moved on site. These procedures involve perforating or cutting the affected casing string and injecting cement slurry under pressure through perforations in the casing or liner to plug the channel or microannulus [41].

Wojtanowicz et al. (2001) emphasize that the success rate of these types of remedial operations is low (less than 50%) due to the difficulty in establishing an injection from the wellbore into the annular space of the casing with SCP and getting complete circumferential coverage by the cement [42]. Prevention of flow after cementing has been approached in two ways: either by formulating special cement slurries or by using mechanical concepts such as modifications of slurry rheology, downhole installations, or placement procedures [43]. The success rate increases when circulation is possible through the channels, when isolation is used for cement injection, and when the workers who perform the procedure are experienced. Certain operations during squeeze cementing can significantly affect its success such as plugged perforations, lost circulation problems encountered during drilling, and strong water cross flows [44]. Such SCP remedial operation has an even lower probability of success when cracks and channels on the micro-scale are present in the cement sheath.

There have been unsuccessful attempts to use squeeze cementing with a special cement design in order to plug small diameter cracks and fissures in the cement sheath. Halliburton's Microbond cement was used at the beginning in the 1990s. It was expected that after a five-day curing time Microbond would expand and seal the cracks. The majority of these operations failed, as either no surface effect was noticed or very little pressure reduction was realized [45]. There was, however, recent success in this area using class G cement, which is closest to API class H cement. Coil tubing squeeze cement jobs have been done successfully in Alaska with class G cement and have been proven to be very reliable for P&A and remedial squeeze work in long horizontal wells [46].

## 2.3 Expandable Casing Technology

### 2.3.1 Pipe Expansion (Plastic Deformation)

Tubular expansion occurs when the applied stresses are above the yield point but short of the ultimate strength limit of the material [47]. A metal may be regarded as macroscopically homogeneous and isotropic. As a result of plastic deformation, an initially isotropic material becomes anisotropic and this development with progressive cold work results in strain-hardening [48]. If the stress applied is below the yield strength (Figure 2.3, point B), the material, in this case metal, behaves elastically, and the original shape is regained on removal of the applied load [48]. The yield point is the limit at which the linear stress-strain relationship, known as Young's modulus, ceases to hold.

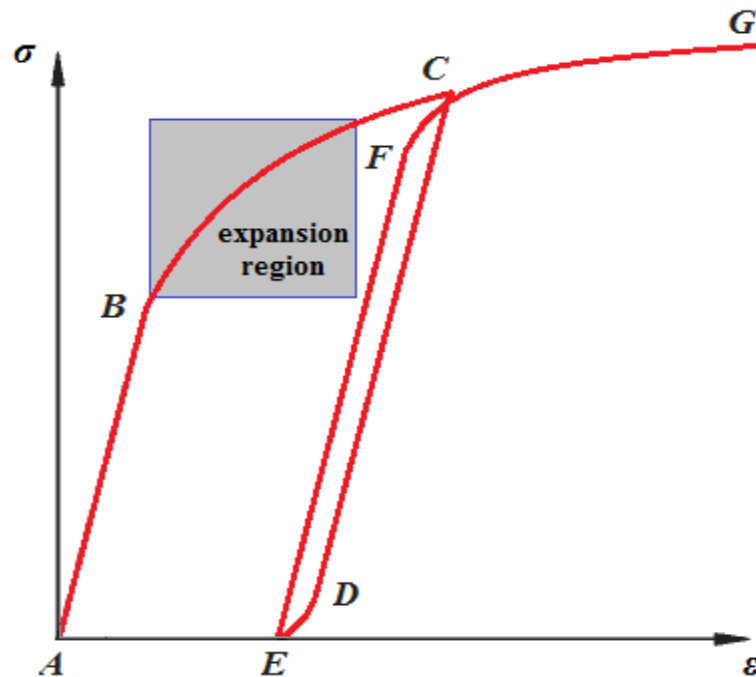


Figure 2.3: True stress-strain curve of metals with effects of loading and unloading. Expansion region represents the stress-strain curve during pipe expansion. Graph showing material under loading beyond elastic limit (yield point, B). During reloading, new yield point (F) is reached and with further loading, the stress-strain curve proceeds along FG, virtually as a continuation of the curve BC (adapted from Chakrabarty, 2006).

Beyond the yield point, the stress continually increases with further plastic strain, while the slope of the stress–strain curve (the rate of strain hardening) steadily decreases with increasing stress. If the material is stressed to some point C in the plastic range and the load is then released, there is an elastic recovery (line CD) and the remaining permanent strain is equal to AE. In the case of reloading, the specimen deforms elastically until a new yield point F is reached, and on further loading, proceeds into plastic range. The curve EFG may be regarded as the stress–strain curve of the metal when prestrained by the amount AE. Chakrabarty (2006) concludes that the greater the degree of prestrain, the higher the new yield point and the flatter the strain-hardening curve will be, resulting in higher strength of the material in loading direction [48].

If an initially stress-free body has been loaded into the plastic range, but short of collapse, and the loads are then reduced to zero, the stress field in the unloaded body does not in general vanish [49]. Asahi et al. (2005) declare that the proportional limit of a compressive stress-strain curve in the circumferential direction greatly decreases after pipe expansion due to the Bauschinger effect, while tensile strength increases and elongation tends to decrease [50].

When metal is yielded non-uniformly through an entire cross section, residual stresses remain in the cross section after the load is removed [51]. An overload produces residual stresses favorable to future loads in the same direction (additional casing expansion, burst pressure) and unfavorable to future loads in the opposite direction (collapse pressure). Jabs (2004) claims that the Bauschinger Effect is countering the final collapse rating of expanded metal, which is the effect that reduces the final collapse rating of the material as a result of stored residual stress following tensile plastic deformation.

During the expansion process when metal material goes from a pre- to post-expanded state, it is being strengthened or hardened by an increase of stress with plastic deformation (or cold-working) which is called isotropic or strain-hardening [49]. This hardening effect improves both the material's final tensile strength and burst capabilities, and the highest stress attained before unloading is the new yield point.

It is impossible, however, to achieve a constant recovery of collapse rating with the strain aging technique throughout the entire length of the post-expanded tubular. Therefore, this reduction in collapse rating must be factored into all expandable designs in order to prevent possible failures. No apparent effect of seam weld toughness on expansion was found when the seam weld quality is good. The ability of material to withstand the expansion process and the post-expansion characteristic of this material, such as good elongation properties balanced with final yield strength, is the main criteria for selecting a material for use in an expandable tubular system [52].

During expansion, while the pipe diameter ( $D$ ) is increasing, the pipe is decreasing in length, and wall thickness ( $t$ ) is being reduced. This increase in  $D/t$  ratio is one of the major causes for reduction in collapse pressure [53]. Mack (2005) concluded that the reduction in wall thickness will be 0.6 of the percentage of expansion (expansion ratio). Pervez (2010) has that number around 0.5, and the reduction in length at 0.2 of the percentage of expansion [54].

### **2.3.2 Solid Expandable Tubulars**

Expandable tubular technology reduces drilling cost, increases the production capability of tubing constrained wells, and increases the depth and reach capability of well designs to access the reservoirs that were difficult or impossible to reach using

conventional well designs. The study by Campo et al. (2003) showed the remarkable environmental and economic impact of solid expandable tubulars [47]. These benefits are the result of the reduction of emissions and consumption of natural resources, as well as reduction in required size of drilling vessels and overall cost of well construction. This technology has the potential to reduce cost, increase production, and provide access to new reserves [55]. Besides steel, expandable tubulars can also be manufactured from non-ferrous metals such as aluminum or titanium [56].

The first commercial installation of Solid Expandable Tubulars (SET) was performed by Chevron on a well in shallow waters of the Gulf of Mexico in November 1999 [57]. The current operating envelope for expandable tubulars encapsulates an inclination of 100° from vertical, temperature up to 400°F (205°C), mud weight to 19.8 lb/gal (2.37 g/cm<sup>3</sup>), a depth of 28,750 ft (8763 m), hydrostatic pressure of 23,300 psi (160.6 GPa) and a tubular length of 6,865 ft (2092 m) [58]. A typical expansion rate for solid expandable tubulars is approximately 7.8 ft/min (2.4 m/min) [59].

A common solid expandable tubular installation consists of an expandable anchor hanger and a pre-determined length of tubulars to be expanded. The expansion operation takes place hydraulically from the bottom up and usually takes place after the cement slurry has been pumped into the annulus [60]. SET technology can be applied in existing or new wells. It is extensively used in Extended Reach Drilling (ERD) wells in order to cut the drilling cost and preserve an optimum diameter at the pay zone.

The expansion of solid tubulars is accomplished by two main techniques; i.e. using a cone/swage or a rotary expansion tool. In its simplest form, cone expansion is performed by fixing one end of the tubular and forcing the swage toward the free end by mechanical

or hydraulic means [61]. The progress of the cone through the pipe expands it beyond its elastic limit while still keeping stresses below the yield stress.

Figure 2.4 shows the process of installing an expandable liner system in the wellbore. The openhole part should be first under-reamed and conditioned with mud. Expandable liner is then run into the wellbore and set up for a cementing operation. After cement placement, the liner is expanded into the hanger joint to make a sealed connection. This system can be used in both vertical and horizontal wells [62]. Using a solid expandable tubular system in the upper sections of the well design preserves hole size, thus contributing to drilling efficiency and minimizing the risk associated with small hole size in deeper sections of the wellbore [63].

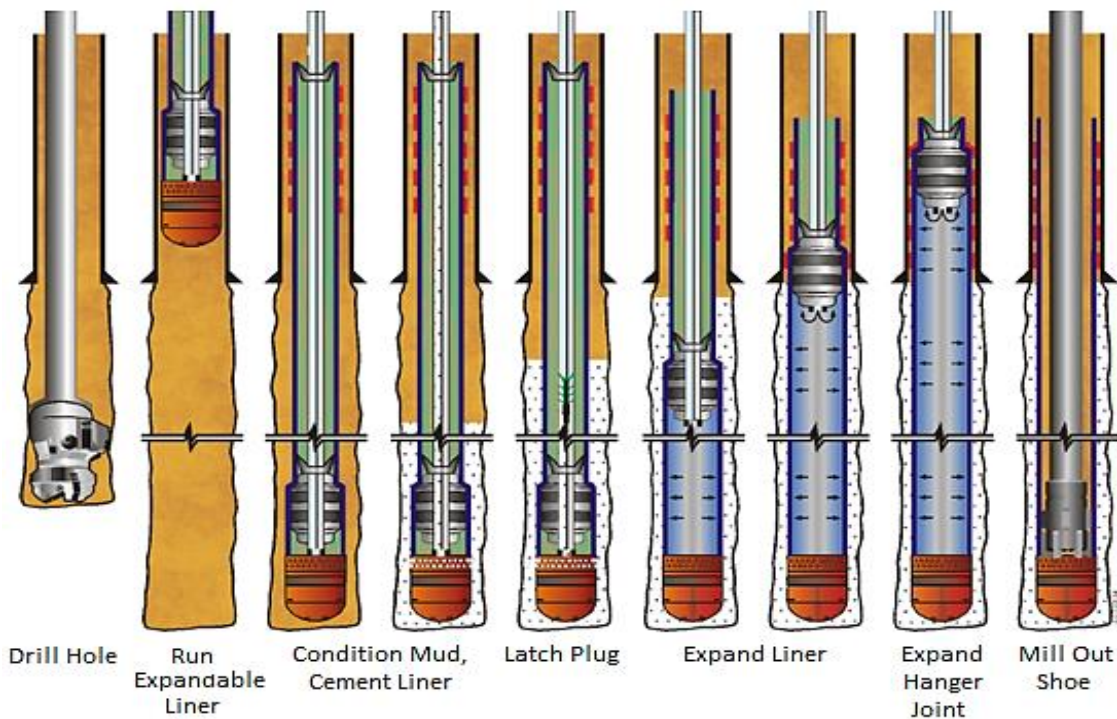


Figure 2.4: Installation sequence for Expandable Openhole Liner System. Expandable cone is run with the liner in the open hole and pulled after primary cement job. Pulling of expansion mandrel expands the pipe all the way to the hanger joint, latching it into place [62].

Expandables are not only used in drilling in order to keep the hole size; the use of expandable technology for casing repairs has also been documented. Two kinds of expandable casing remediation systems exist, one of which utilizes a solid tubular and expands every joint of the liner, while the other one is utilized at the top and bottom of the patch [64].

Cone optimization has also been a key to the success of expandable tubular technology. The result of multiple expansion experiments suggest that an optimized shaped cone is burnished evenly along the entire expansion surface. This design has eliminated the large contact pressure spikes that occurred with previous designs, and it substantially decreased the connection failures during expansion process [65]. Their study showed that axial forces exerted on the tubular are higher but much more evenly spread with a 2° optimized cone than a 10° cone. The expansion cones used in this research had a cone angle of 14°.



### CHAPTER 3: EXPERIMENTAL METHODOLOGY

To accurately simulate tubular expansion under field-like conditions, a unique bench-scale physical model was developed. The main part of this physical model was the custom-made expansion fixture. Special composite cement samples with steel pipes were designed in order to represent the casing/formation cemented annulus. Density of cement slurry used was 13.1 lb/gal (1.57 g/cm<sup>3</sup>), with w/c ratio of 0.87, and the samples were cured in the water bath at ambient conditions for minimum of 28 days.

Expansion cones with three designed expansion ratios (2%, 4%, and 8%) were used for pipe expansion, and integrated load cell measured axial forces during expansion. These force measurements were used for axial stress and contact pressure calculations. Multi-rate flow-through tests with nitrogen gas were run pre- and post-expansion to determine the success of pipe expansion in sealing the gas flow through the pre-manufactured microannulus. Pressure differentials, recorded with pressure transducers, were used as variables in calculations of microannulus effective permeability. This physical model investigated the potential of expandable casing technology as a new remediation tool for SCP that is caused by microannular gas migration.

All of the experiments were done in the lab (room no. 167) at LSU South Campus, located at 8000 GSRI Avenue, Baton Rouge, LA. The lab was set up specifically for this research and fills all the necessary safety requirements of both the LSU Safety Office and Shell project managers.

### **3.1 Expansion Fixture**

The focal point of the physical model is the expandable fixture (Figure 3.1) which was designed by David Brisco and manufactured at Shell's Westhollow Technology Center in Houston, TX. The 30,000 lbf (133.5 kN) hydraulic expansion system consists of: hydraulic power unit, control switch, hydraulic cylinder, upper and lower housing, expansion and retaining mandrel, integrated load cell, and expansion cones.

#### **3.1.1 Hydraulic Power Unit**

Parker® V-Pak variable displacement hydraulic power unit was utilized as the main driving component of the hydraulic system. Vertical 40-gallon (151-liter) tank was ideal for saving space in the lab and for quiet and leak-free operations. ISO 46 hydraulic oil was used and the maximum flow rate is 15 gal/min (57 l/min) at 2,140 psi (14.8 GPa) (unit's maximum pressure rating). This unit has a 3-phase, 230/460 V electric motor with 20 horsepower and 1800 rpm. A 3-phase current with both the power and safety switch was installed in the lab for this purpose. Parker power unit has an integrated relief valve as an additional safety feature.

#### **3.1.2 Control Switch**

Parker D3L1CN directional hydraulic control valve was used to manipulate the expansion mandrel by controlling the hydraulic cylinder. It is a 4-way, direct operated, lever controlled valve which enables safe running of expansion experiments. Maximum flow rate is 40 gal/min (151 l/min) and pressure rating is 5,000 psi (34.5 GPa).

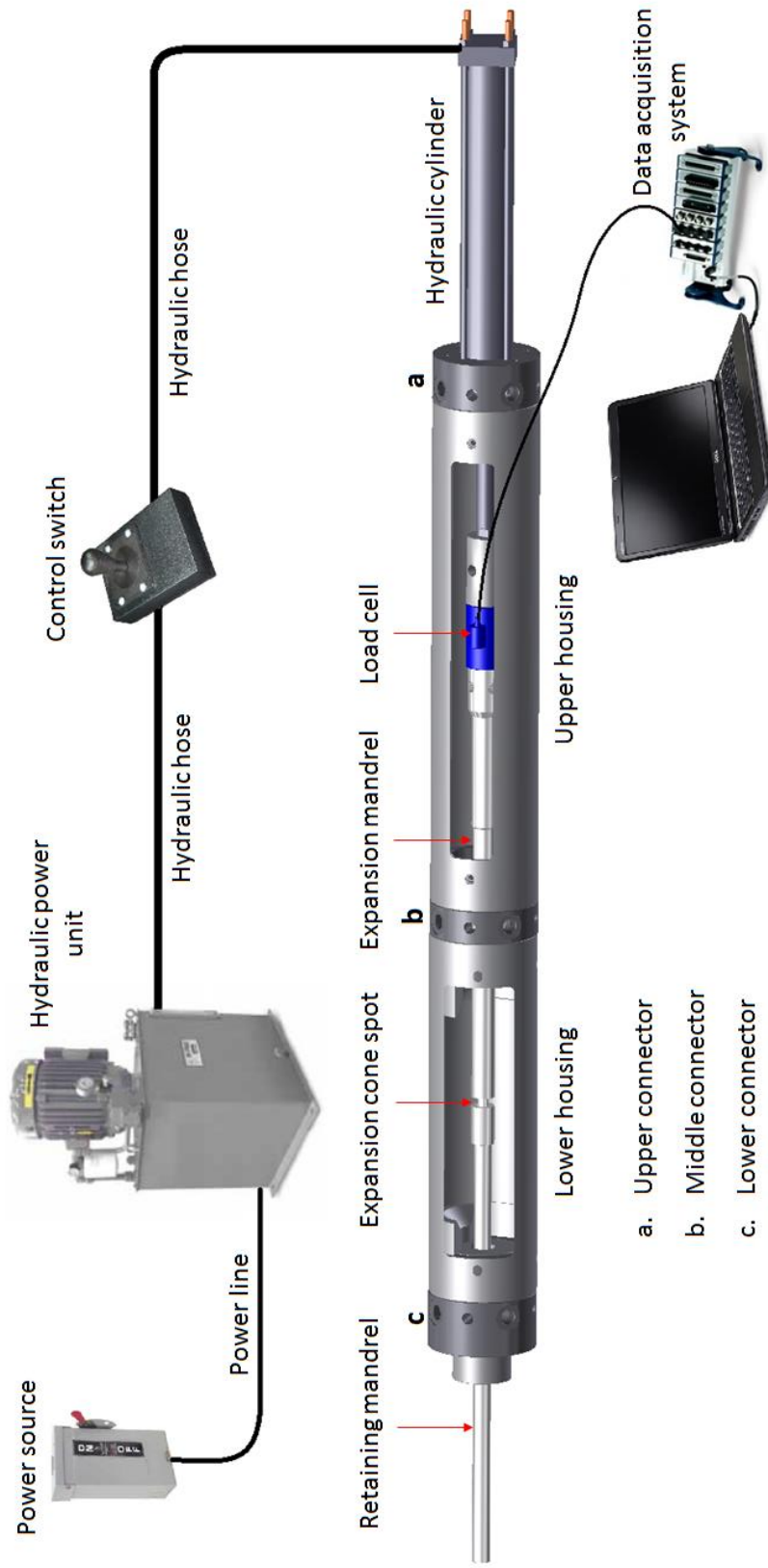


Figure 3.1: Schematic of experimental fixture and auxiliary equipment (not to scale). Hydraulic power unit is powered by turning the switch of the power source. Control switch controls hydraulics and operates the hydraulic cylinder which results in retaining or extending the expansion mandrel. Integrated load cell, which measures axial forces during expansion, is located between the piston rod of the hydraulic cylinder and the expansion mandrel. Force measurements are recorded and monitored in real time with the data acquisition system. The expansion cone is placed onto the end of the expansion mandrel and held in place with the retaining mandrel. Upper, middle and lower connector hold the assembly of the expansion fixture together (3D image of the expansion fixture courtesy of Paul Rodriguez, LSU).

### **3.1.3 Hydraulic Cylinder**

A hydraulic unit powered the Parker hydraulic cylinder with a 4-in. (10.16-cm) bore and 1.75-in. (4.4-cm) piston rod, rated for 30,000 lbf (133.5 kN) maximum compressive load. The cylinder, which has a nominal pressure of 3,000 psi (20.7 GPa), was bolted to the upper connector of the upper housing. It has a 28-in. (71-cm) stroke to allow the expansion mandrel to be completely retracted out of the lower housing when loading and unloading the composite sample. Furthermore, this enables the expansion cone to be completely pushed out of the test sample after the expansion test.

### **3.1.4 Upper and Lower Housing**

The main body of the machine is made of two pieces of 9.625 in. (24.4 cm), 43.5 lb/ft (64.7 kg/m) casing with three connectors: upper, middle and lower connector. The 32.75-in. (83.2-cm) lower housing has a 6.19-in. (15.7-cm) wide window through which the test sample can be inserted. The 42.75-in. (108.6-cm) upper housing has two 4-in. (10.16-cm) wide openings on the top and bottom through which the cable for the load cell can be run. All the parts were phosphate coated for corrosion protection.

### **3.1.5 Expansion and Retaining Mandrel**

The expansion mandrel, designed to withstand the load of 30,000 lbf (133.5 kN), is connected to the piston rod through connectors and it runs through a hole in the middle connector of the machine body and the test sample. The length of the expansion mandrel is 42.25 in. (107.3 cm) and the diameter of the section which goes through the lower housing is 2.106 in. (5.35 cm). The expansion cone is placed on the lower end of the expansion mandrel and held in place with the 41.75-in. (106-cm) long retaining mandrel.

The retaining mandrel extends through a hole in the lower connector and the retaining mandrel guide which is attached to the lower end of the lower connector and centralizes the lower end of the composite sample. Its upper end is centralized with a machined pocket in the lower end of the middle connector. The retaining mandrel is long enough to be removed from the expansion mandrel at the end of the expansion stroke if needed.

### 3.1.6 Load Cell

The Futek<sup>®</sup> LCM550 in line load cell with 10-ft (3-m) long 24 AWG 4 conductor shielded PVC cable was integrated in the expansion fixture. It is made from 17-4 stainless steel and male threads on both ends allowing the load cell to be connected to the piston rod with an adapter on one end and to the expansion mandrel with the connector on the other end. This integrated load cell has the capacity of measuring axial forces in tension of up to 50,000 lbf, and it has been calibrated with the hydraulic press in tension mode.

### 3.1.7 Expansion Cones

Expansion cones (Table 3.1, Figure 3.2) were made from AISI D2 grade alloy steel that was heat treated to the hardness of 60 RC. The expansion cone was slipped over the lower end of the expansion mandrel and held in place with the retaining mandrel.

Table 3.1: Dimensions of expansion cones.

<b>Expansion Ratio [%]</b>		<b>Cone OD [in.]</b>	<b>Cone Angle [°]</b>
<b>Designed</b>	<b>Actual</b>		
2	1.46	2.189	14
4	3.45	2.232	14
8	7.43	2.317	14

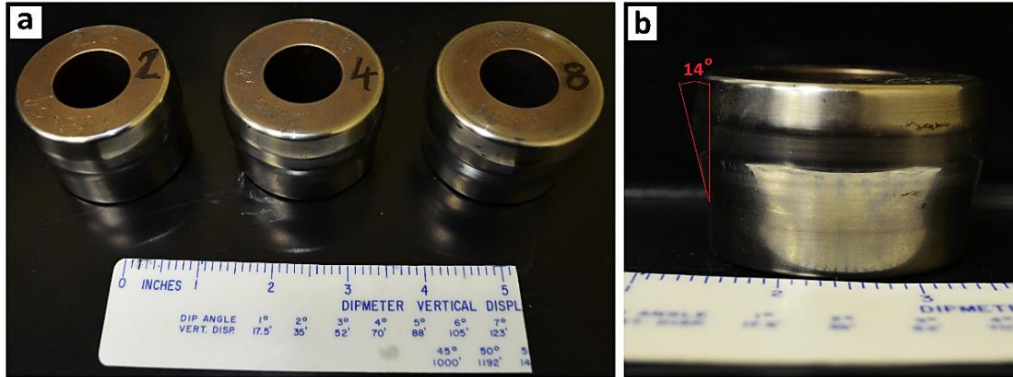


Figure 3.2: a. expansion cones with 2%, 4% and 8% expansion ratio; b. side view of 2% expansion ratio cone. All cones have 14° cone angle and are made from AISI D2 grade alloy steel which was heat treated to the hardness of 60 RC.

### 3.2 Composite Sample

Composite samples were designed to represent the casing/formation cemented annulus, consisting of “pipe inside pipe” metal components with cement filling the annular space. The primary focus of a selected cement slurry was on two different densities: 13.1 lb/gal (1.57 g/cm<sup>3</sup>) and 16.4 lb/gal (1.96 g/cm<sup>3</sup>).

#### 3.2.1 Metal Components

The 24-in. (61-cm) long sample, shown in Figure 3.3, consists of two ASTM A53 grade B electrically resisted welded (ERW) carbon steel pipes. The 23.5-in. (59.7-cm) outer pipe has a 4 in. (10.16 cm) outside diameter (OD) and 0.225 in. (5.7 mm) wall thickness, while the 24-in. (61-cm) inner pipe has a 2.375 in. (6 cm) OD and 0.109 in. (2.8 mm) wall thickness. Yield and tensile strength of the pipes are 35,000 psi (241.3 GPa) and 60,000 psi (413.7 GPa), respectively. The welding bead on the inside wall of the inner pipe has been machined out and a quarter-inch steel plate ring was welded at the end to seal the annulus between the two pipes. Outer pipes were coated with zinc anticorrosion spray, to prevent corrosion during the curing period. Prior to expansion, the inside wall of the inner pipe was coated with Houghto-Kote<sup>®</sup> lubricant for smooth running of the expansion cone.

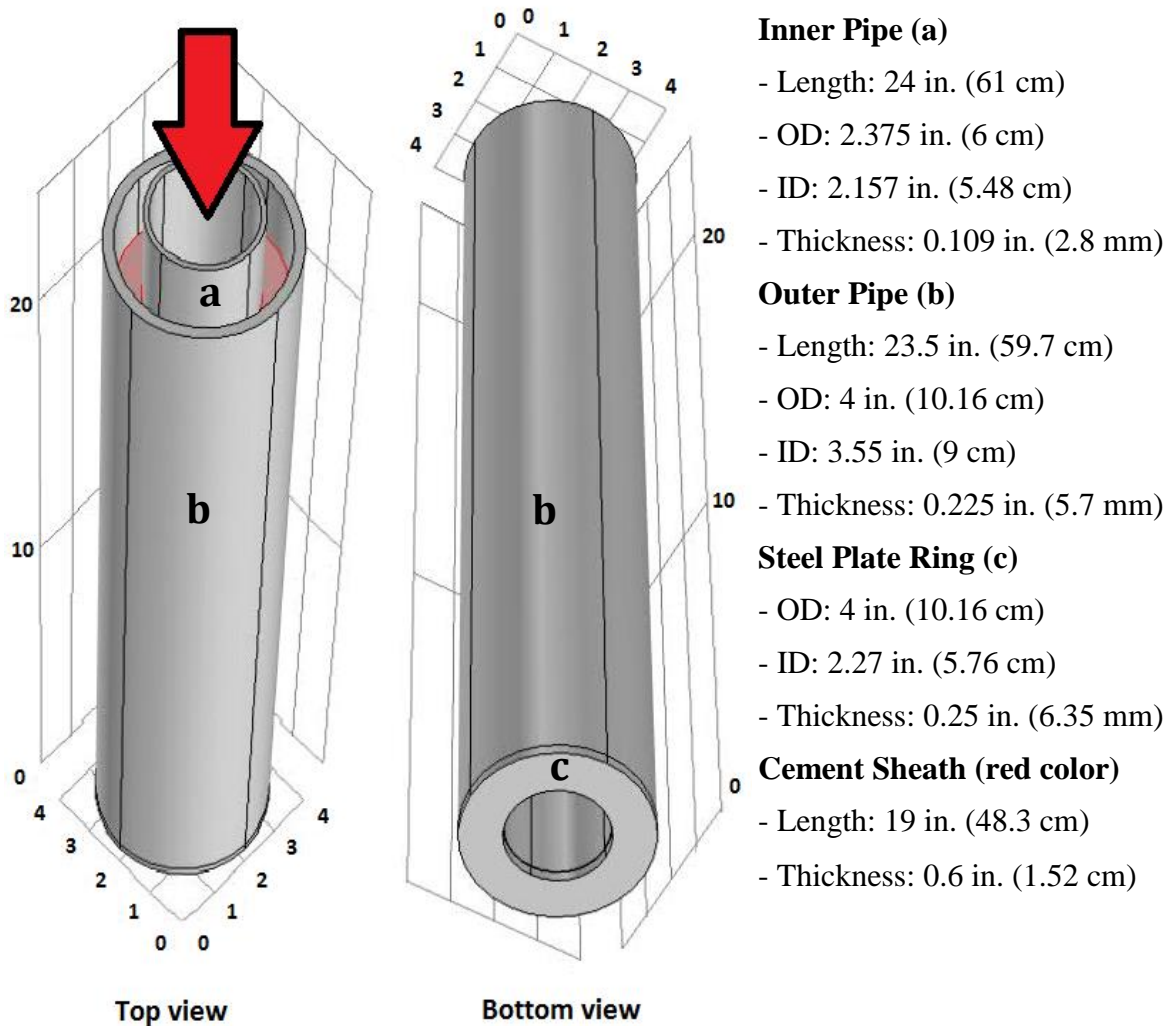


Figure 3.3: Composite sample schematic. Top view shows the cement (red color) between inner (a) and outer pipe (b). The arrow points the direction of expansion. Bottom view shows the steel plate ring (c) welded to outer pipe and pipe coupling. Inner pipe is screwed into the coupling (the scale is in inches).

Custom-made steel coupling with 2.5 in. (6.35 cm) OD was welded to the quarter-inch steel plate ring (Figure 3.4). Bottom part of the inner pipe was threaded to allow connection with the welded coupling. The outer pipe was then welded to the steel plate ring. Small holes of 3/32 in. (2.4 mm) were drilled in the outer pipe to allow the relief of pressure and excess free water from cement matrix during expansion process. The inner pipe is screwed into the coupling to finish the composite sample assembly.

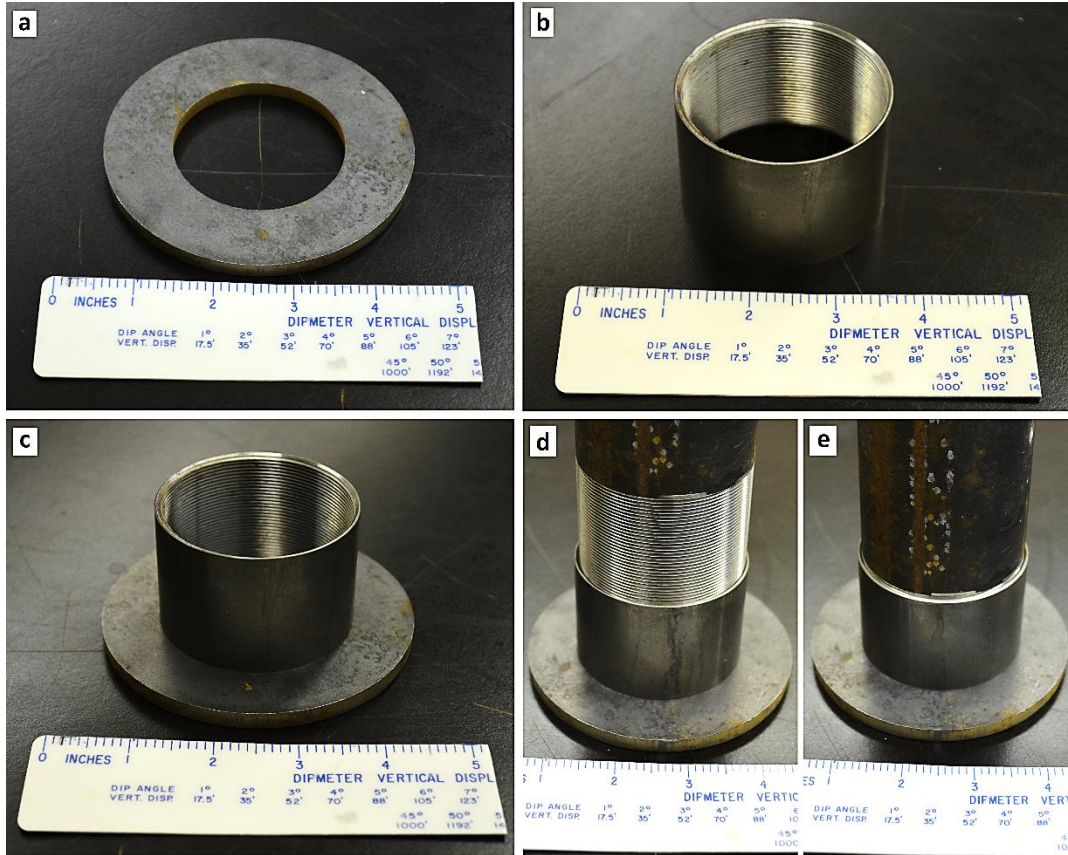


Figure 3.4: Metal components of the bottom part of the composite sample: a. quarter-inch steel plate ring; b. 2.5-inch (6.35-cm) OD steel pipe coupling; c. pipe coupling welded onto steel plate ring; d. threaded part of the inner pipe being screwed into the pipe coupling; e. finished assembly. Final part of the composite sample is the outer pipe which is placed at the end and welded for the steel plate ring on the outer region.

Four 11/32-in. (9 mm) holes for gas flow-through experiments were drilled 90° apart on each end of the outer pipe and threaded with 1/8 in. (3.2 mm) NPT threading tip from Grainger®. These threaded ports allowed connection with Swagelok® fittings and Teflon® tubing manifold assembly on the bottom (inlet) and top (outlet) side of the sample. Inlet and outlet ports, which were 16 in. (40.64 cm) apart, were used for connecting the gas manifold with the pressure transducers for pre- and post-expansion multi-rate flow-through experiments.



### 3.2.2 Cement Slurry Design and Preparation

There were two cement designs selected for preliminary experiments. The first design selected for testing was 16.4 lb/gal (1.96 g/cm<sup>3</sup>), 0.38 w/c ratio cement slurry. The second one was water-extended lightweight cement slurry of 13.1 lb/gal (1.57 g/cm<sup>3</sup>), 0.87 w/c ratio. The annulus between inner and outer pipes was cemented with the cement slurry which was cured in a water bath at ambient conditions for a minimum period of 28 days. The pH of the water bath was kept between 12 and 13 by mixing the water with Ca(OH)<sub>2</sub>. Halliburton D-Air 3000L™ defoaming agent and bentonite were used as additives for the API Class H cement from LaFarge Corporation. A 1.06-gal (four-liter), 3.75 horsepower Waring® laboratory blender was used for cement slurry preparation. Defoamers are used to minimize the foaming of cement slurries and get rid of the entrapped air in the mixture. Bentonite is used in order to increase the yield of the cement, decrease the cement density and decrease the fluid loss, but its addition increases the porosity of cement thus exposing the cement to corrosion due to acidic formation fluids [3].

For preparation of the 16.4 lb/gal (1.96 g/cm<sup>3</sup>) cement slurry, 2.75 lb (1250 g) of water was first poured into the blender. It was turned on low speed (15,800 rpm) after which 0.35 oz. (10 g) of defoamer and 7.25 lb (3290 g) of cement powder was poured into the blender and sheared for 40 seconds on high speed of 20,800 rpm. The cement slurry was then poured into the annulus between two pipes and covered with a wet cloth and plastic wrap. The cemented composite sample was left for 24 hours and then placed in the water bath for a minimum period of 28 days.

The lightweight water-extended cement slurry was prepared by first pouring three pounds (1350 g) of water into the blender and one ounce (30 g) of bentonite was pre-

hydrated for five minutes on low speed (15,800 rpm). After five minutes, 0.18 oz. (5 g) of defoamer and 1500 g of cement powder were poured into the blender and sheared for 40 seconds on high speed (20,800 rpm). The cement slurry was then poured into the annulus between two pipes and covered with a wet cloth and plastic wrap for a period of 24 hours. The sample was placed in the water bath next day for a minimum period of 28 days.

The connection between the pipe coupling and the inner pipe allowed the pipe rotation during first 26 hours of cement hydration, in order to create a microannulus at pipe-cement interface. A thin layer of baking spray was applied on the outer wall of the inner pipe prior to cementing. Six hours after the cement slurry was poured between the pipes, the inner pipe was rotated a quarter-turn back and forth every 15 minutes for the next 20 hours of cement hydration to prevent cement bonding with the inner pipe.

Prior to gas flow-through experiments, ½-in. (1.27-cm) layer of Loctite® epoxy was placed on the top of the cement sheath to prevent any leakage of nitrogen gas through the top side of the microannulus. Air Liquid's Alphagaz™ 1 nitrogen gas was used with total purity of 99.999%, and the following impurity specifications: H<sub>2</sub>O<3 ppm, O<sub>2</sub><2 ppm and THC<0.5 ppm.

### **3.3 Measuring Devices**

Two Omega® PX480A-200GV pressure transducers with a range of 0 to 200 psi were used for pressure recordings on the inlet (bottom) and outlet (top) sides of the composite sample. They have an accuracy of 0.3% BFSL maximum, and all the wetted parts are made of 316L stainless steel. The transducers were connected to the side part of a Swagelok cross fitting of the gas manifold.

Pressure transducers and load cell measurements were recorded by National Instruments (NI) cDAQ-9188 data acquisition package. Four NI-9219 chassis were installed and all the data was processed by NI LabVIEW™ Signal Express software. Output of the data was in mV which was converted using linear calibration to respective units for both types of device (lbf and psi). Data was displayed and monitored on the computer screen in real time.

Cole-Parmer® 65-mm variable area, correlated flow meter was used to keep the flow of nitrogen constant through each flow-through experiment. It consists of a heavy-walled glass flow tube mounted in an anodized aluminum frame with white acrylic back plate and a high precision valve, ideal for low-flow application. Maximum operating pressure is 200 psi (1.38 MPa), maximum nitrogen gas flow rate it can measure is 0.004 ft<sup>3</sup>/min (113 ml/min), and the accuracy is ±2% of the full scale.

### **3.4 Microhardness Tester**

The Nanovea® Micro/Macro Module, with loads from the mN range to 45 lbf (200 N), allowed micrometer-scale indentation testing. The sensitive loads of the micro range can be utilized for the characterization of softer and more fragile materials (material's coatings, ceramics, cement).

The Micro/Macro Module uses independent force and depth sensors to obtain depth-versus-load curves used in instrumented indentation. The microhardness tester is able to perform tests of penetration depths in the micrometer scale. Displacement measurements were done by a non-contact optical sensor with displacement resolution of  $0.39 \cdot 10^{-6}$  in. (10 nm). Maximum indenter range is 0.012 in. (300 μm), while the load range is 0-9 lbf (0-40 N) with normal load resolution of  $0.34 \cdot 10^{-3}$  lbf (1.5 mN).

### **3.5 Experimental Procedure**

Experimental procedure consisted of a few main activities, which included expansion experiments, measurements during expansion, post-expansion investigation of the cement sheath, and gas flow-through experiments.

#### **3.5.1 Expansion Fixture Assembly, Testing and Calibration**

Prior to the start of the experiments, the expansion fixture had to be assembled in the new lab. Two heavy duty welding tables, rated for 2000 lbs (907 kg) were placed in the middle of the lab onto which the expansion fixture was to be assembled. The expansion fixture was delivered in two crates, together with the hydraulic power unit and the hydraulic cylinder. A motor jack had to be used to lift the heavy parts of the equipment after which the assembly process was carried out on the welding tables. After installing all the parts, the hydraulics were connected and the machine was ready for expansion.

Upon assembly, the expansion fixture was tested at optimum hydraulic unit pressure of 1500 psi (10.34 MPa). The first composite sample to be tested for expansion with 8% expansion ratio cone was with 16.4 lb/gal (1.96 g/cm<sup>3</sup>) cement slurry. Unsuccessful expansion revealed that the hydraulic unit, together with the hydraulic cylinder did not have enough power to expand the samples with 16.4 lb/gal (1.96 g/cm<sup>3</sup>) cement slurry. In all subsequent experiments, only composite samples with 13.1 lb/gal (1.57 g/cm<sup>3</sup>) cement slurry were used.

The next composite sample with 13.1 lb/gal (1.57 g/cm<sup>3</sup>) cement slurry was successfully expanded with 8% expansion ratio cone in the length of 16 in (40.64 cm). The expansion fixture was operated without problems; the integrated load cell, however,

recorded a suspiciously high value of 50,000 lbf (222.4 kN), which is the rating of the load cell. The expansion mandrel was rated for 30,000 lbf (133.5 kN), therefore it was concluded that the load cell needed calibration with a deformation under known force.

The load cell was designed to only measure axial forces in tension, and the calibration was done by a hydraulic press in tension mode with custom-made couplings for the load cell. These couplings allowed the load cell to be fixed to the top and bottom side of the press. Output conversion from mV to lbf had to be set up by linear correlation in LabVIEW software. This correlation was set with the readings from the hydraulic press and the load cell was calibrated and re-integrated in the expansion fixture. During the next expansion experiment with the cone of 8% expansion ratio, the load cell recorded the axial force of 12,596 lbf (56 kN), which confirmed successful calibration of the load cell.

### **3.5.2 Expansion Experiments**

The experiment begins by unscrewing the retaining mandrel from the expansion mandrel, which is then fully retained from the lower housing by the hydraulic cylinder. After the inner wall of the inner pipe has been fully coated with lubricant, the composite sample (with hydrated cement) is placed in the lower sample housing of the fixture through the opening at the top. The expansion mandrel is then fully elongated through the sample after which the expansion cone (coated with a thin layer of motor oil) with desired expansion ratio is placed on the top. Lastly, the retaining mandrel is screwed onto expansion mandrel, and the lower connector is screwed onto the lower end of the lower housing. The sample is then ready for expansion. This procedure can be seen in Figures 3.6 and 3.7.

The hydraulic unit is powered to an optimum pressure of 1,500 psi, and the axial force recording is activated. By activating the control switch, expansion mandrel is being retracted, and the expansion cone is pulled through the inner pipe of the sample, thus expanding the inner pipe and compressing the cement sheath (Figure 3.5). Samples were expanded over length of 16 in. (40.64 cm), the expansion mandrel was then elongated into original position and recording of axial forces was stopped. The expansion over 16 in. (40.64 cm) is completed in 4 seconds, which is 4 in./s (10.16 cm/s) comparing to the expansion speed of 6 in/s in the field operations.

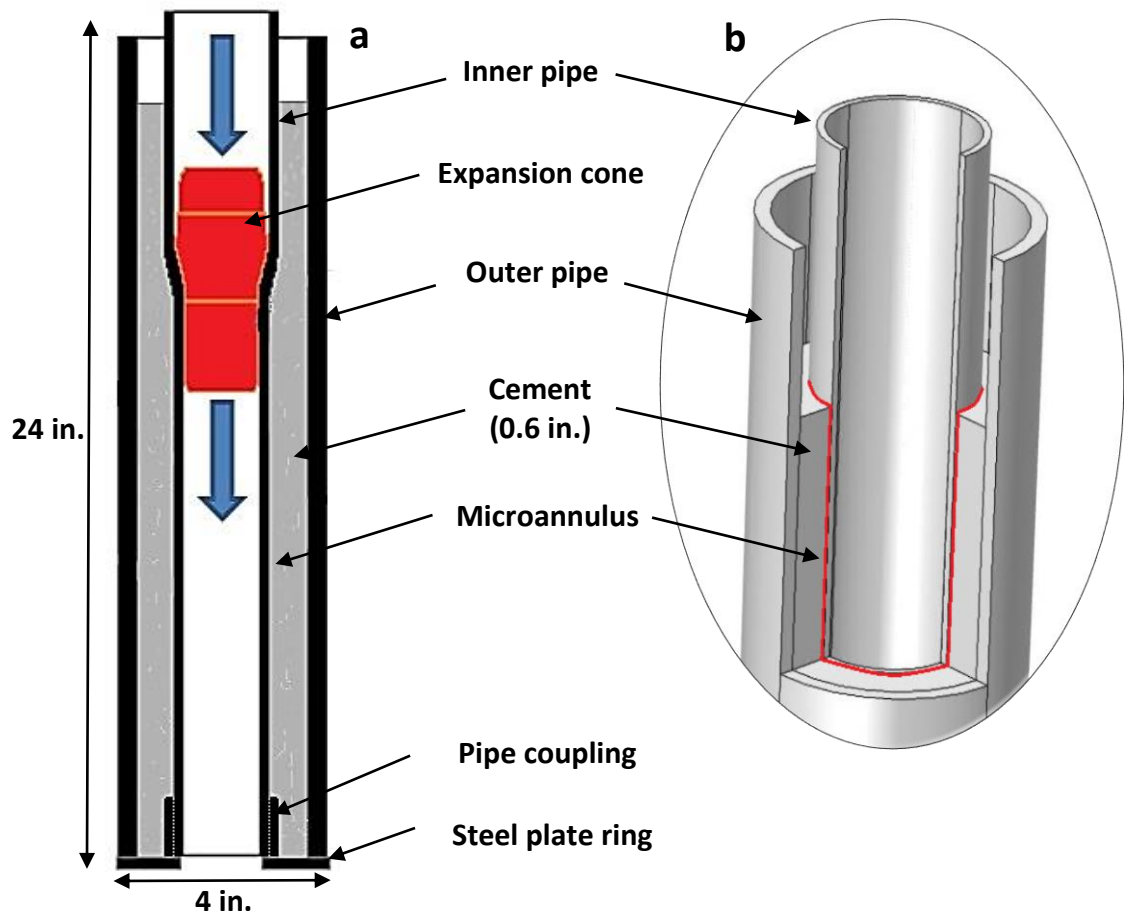


Figure 3.5: a. 2D composite sample schematic. Expansion cone (shown in red) is pulled through the inner pipe, expanding its diameter and compressing the cement sheath (blue arrows point expansion direction). Pipe coupling, which was welded for the steel plate ring at the bottom of the composite sample, allowed screwing of the inner pipe into place. This pipe rotation enabled the inner pipe to be turned during first 24 hours of cement hydration in order to create the microannulus; b. 3D composite sample schematic showing the microannulus (red color, not to scale).

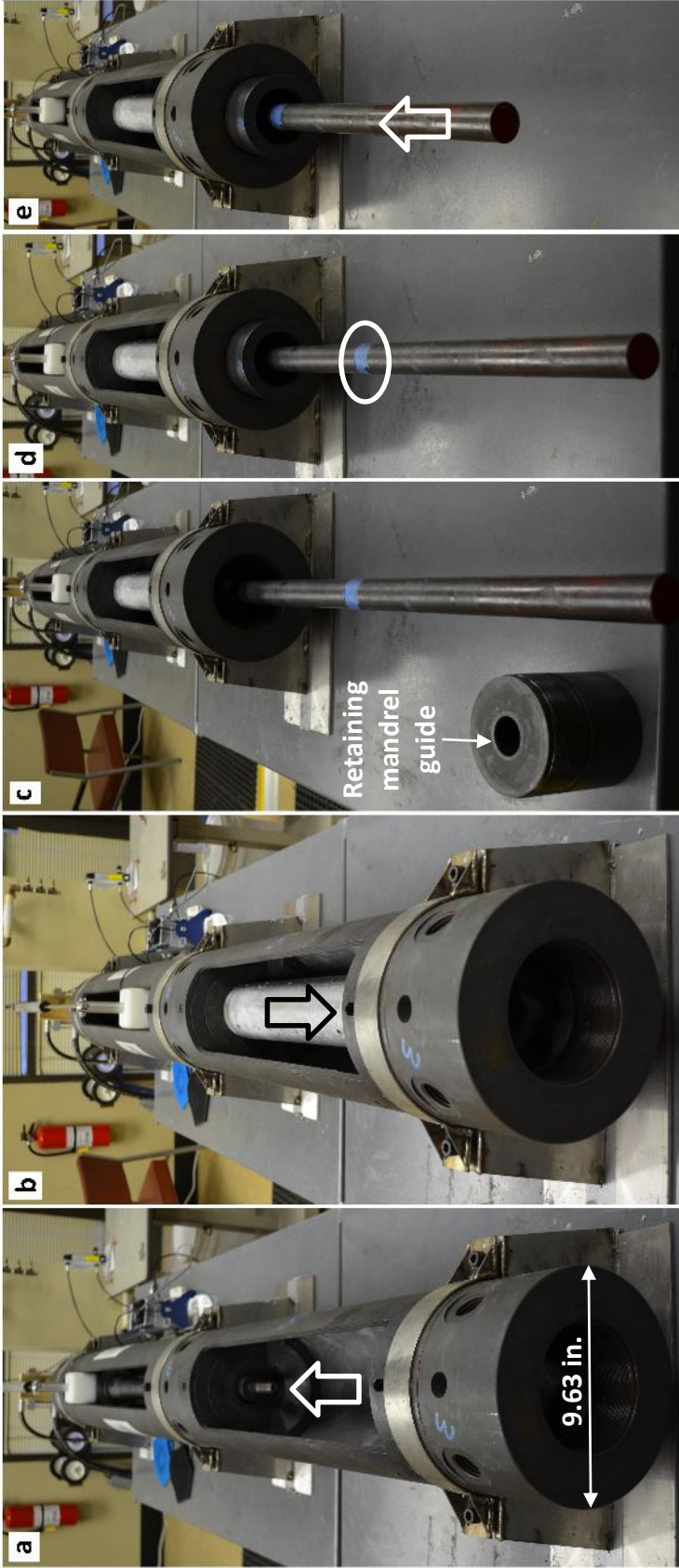


Figure 3.6: Setup and expansion process (front view). a. the expansion mandrel is retained (white arrow showing direction) in order to clear the lower housing for placement of the composite sample; b. the composite sample is placed in the lower housing and the expansion mandrel is fully elongated (black arrow showing direction) through the inner pipe; c. the expansion cone is slipped onto the expansion mandrel and it is held in place with the retaining mandrel which is screwed onto the end of the expansion mandrel; d. the retaining mandrel guide is screwed into the lower connector to complete the assembly and the rig is ready for expansion (blue tape showing the expansion limit); e. the expansion mandrel is retained (white arrow showing direction) and the expansion cone is pulled through the inner pipe (end of expansion stroke).



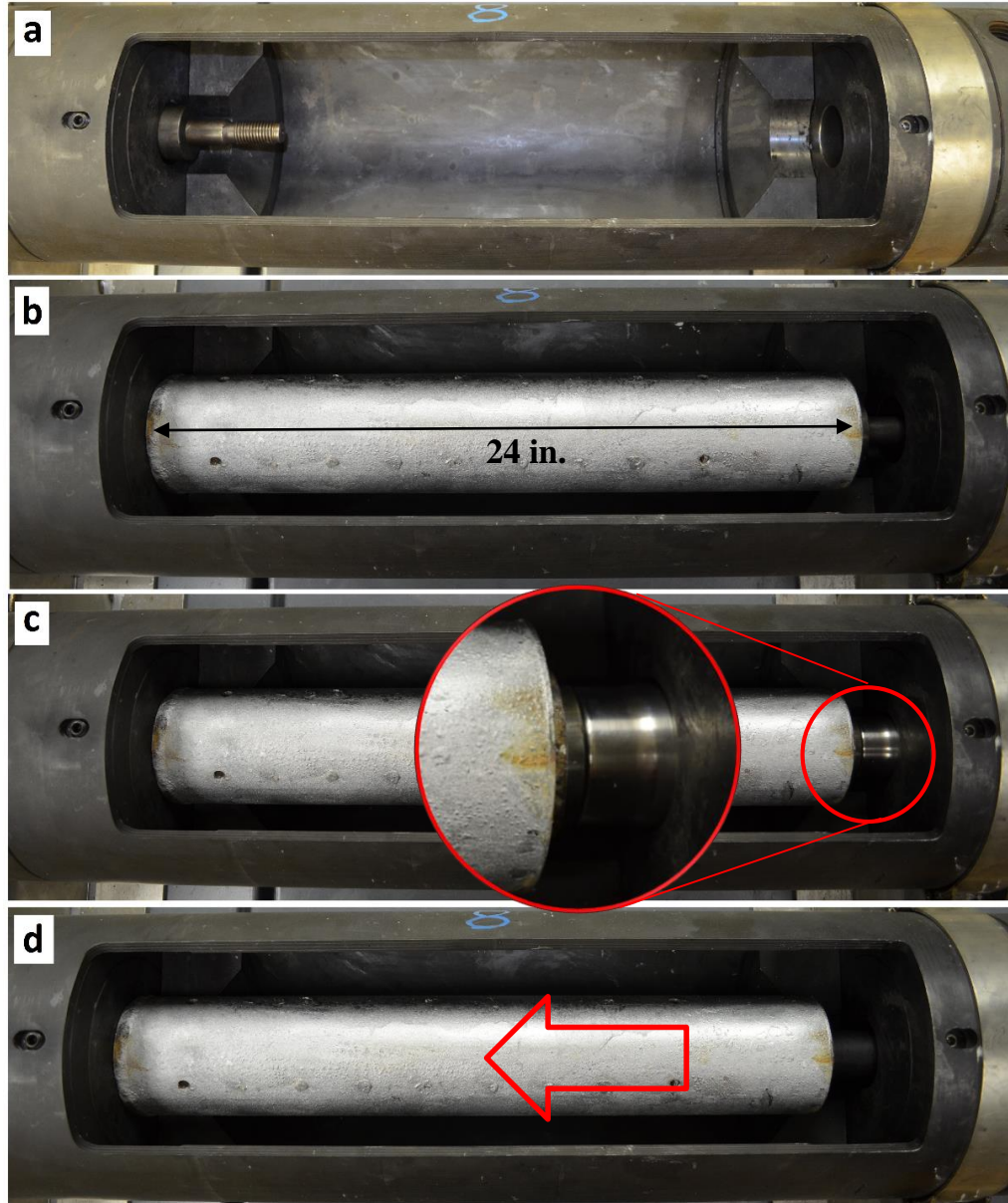


Figure 3.7: Setup and expansion process (top view): a. the expansion mandrel is retained (red arrow shows the direction) in order to clear the lower housing for placement of the composite sample; b. the composite sample is placed in the lower housing and the expansion mandrel is fully elongated through the inner pipe; c. the expansion cone is slipped onto the expansion mandrel. Magnified view shows the expansion cone being held in place with the retaining mandrel; d. the expansion mandrel is retained and the expansion cone is pulled through the inner pipe (red arrow shows the direction of expansion).



### 3.5.3 Force Measurements, Stress and Pressure Calculations

Axial forces recorded by integrated load cell during expansion were used for axial stress, collapse and burst pressure calculations. These forces were measured during expansion of a sample with steel pipe without cement and with regular composite cement sample, in order to compare the difference in forces and stresses in the pipe, with and without cement. Equation (3.1) was used to calculate the axial stress in the pipe during the expansion process:

$$\sigma_z = \frac{F_a}{\frac{\pi}{4}(D^2 - d^2)} \quad (3.1)$$

$\sigma_z$  – axial stress [psi]

$F_a$  – axial force [lbf]

$D$  – pipe OD [in]

$d$  – pipe ID [in]

Collapse pressure rating was calculated using the equation from Bourgoyne et al. (1986) [66]:

$$P_c = Y_p \left( \frac{A}{\frac{D}{t} - B} \right) - C \quad (3.2)$$

$P_c$  – collapse pressure [psi]

$Y_p$  – yield strength [psi]

$D$  – pipe OD [in]

$t$  – pipe wall thickness [in]

$A, B, C$  – empirical coefficients

Empirical coefficients (A, B, C) were taken from Bourgoyne et al. (1986) and the numbers used were for H-40 casing which yield strength (40,000 psi) is close to the yield strength of the inner pipe used (35,000 psi) [66]. The A, B, C coefficients used were 2.95, 0.0465 and 754 respectively. Increase in D/t ratio is the main factor for collapse rating

decrease. Wall thickness of the expanded pipe was assumed to decrease by 0.6 times each of the expansion ratio percentage [54].

Burst pressure rating was calculated using the following equation [66]:

$$P_{br} = 0.875 \left( \frac{2Y_p t}{D} \right) \quad (3.3)$$

$P_{br}$  – burst pressure [psi]

$Y_p$  – yield strength [psi]

$D$  – pipe OD [in]

$t$  – pipe wall thickness [in]

New outer diameter of the pipe was obtained with the same assumption that the wall thickness of the expanded pipe decreased by 0.6 times each of the expansion ratio percentage [54].

### 3.5.4 Post-expansion Investigation

The fluid samples collected through the holes on the outer pipe during expansion were analyzed using inductively coupled plasma (ICP) mass spectrometry. This is an analytical technique for measuring concentration of elements. Shortly after expansion, samples were taken out of the fixture and wrapped in plastic wrap to prevent carbonation. Samples were then taken for cross-section cutting of expanded region in order to expose manipulated cement sheath. Segmented diamond steel blade was used to cut through both steel pipes and cement, providing cross-sectional disc samples. Visual examination of the cement sheath was conducted in order to check for changes in cement, and samples of cement sheath were taken for tests of mechanical properties and material characterization (which will be reported in a future publication).

### **3.5.5 Optical Microscopy**

Leica<sup>®</sup> DM2500-P modular polarization optical microscope, with multiple levels of magnification provided by ocular lenses, was used for investigation of cement sheath thin sections. The samples used for this visual investigation technique were prepared at the Weatherford Lab in Houston. The cement sheath cuts were taken out from the composite sample (Appendix E) and impregnated with resin, after which vertical and horizontal thin cement sections were made. The purpose of this analysis under medium magnification (x50,000) was to observe the changes in the cement structure caused by pipe expansion.

### **3.5.6 Thermogravimetric Analysis**

Thermogravimetric Analysis (TGA) was selected as a cement thermal analysis technique. It determines the weight changes of different minerals within the sample as it is gradually heated at a uniform rate. Crystalline changes cannot be detected, however, since they do not involve weight changes. TGA for this experiment was conducted at LSU's Center for Advanced Microstructures and Devices (CAMD).

The machine used was TA Instruments SDT Q600 Simultaneous DSC/TGA with available temperature range from ambient to 2732°F (1500°C). Low temperature endothermal transition on the heat flow curve is associated with the weight loss of a certain phase. The following parameters were used for the tests: purge gas of nitrogen with a flow rate of 0.0035 ft<sup>3</sup>/min (100 ml/min); alumina pans; equilibration at 104°F (40°C) for 10 minutes; heating rate of 41°F/min (5°C/min) from 104°F (40°C) to 392°F (200°C), followed by a heating rate of 50°F/min (10°C/min) up to 1832°F (1000°C). Sample preparation entailed crushing the cement sample into powder and placing 0.35-0.53 oz. (10-15 mg) in the machine.

### 3.5.7 Microhardness Test

The microhardness test uses an established method where a diamond indenter tip with a known geometry is driven into a specific site of the sample by applying an increasing normal load. When reaching a pre-set maximum value, the normal load is reduced until partial or complete unloading of the sample occurs. For each loading/unloading cycle, the applied load value is plotted with respect to the corresponding position of the indenter. Five-spot indentation was done in a form of a line profile, on every sample ranging from inner pipe position to the outer region of the cement sheath, covering its entire cross-section (Figure 4.7). The resulting load/displacement curves provide data specific to the mechanical nature of the sample tested (primarily hardness and Young's modulus). Established models are used to calculate quantitative hardness and modulus values for such data.

The following set of conditions was used in all the indentation experiments: the maximum force used was 4.5 lbf (20 N); the loading and unloading rates were kept the same at 4.5 lbf/min (20 N/min); the pause at maximum load was 30 seconds; the contact load was  $6.7 \cdot 10^{-3}$  lbf (30 mN); the computation method used was from Oliver & Pharr [67]; the indenter type was Vickers diamond with the Poisson coefficient of 0.30. There are three important parameters that must be measured from the load/displacement curves: the maximum load ( $P_{\max}$ ), the maximum displacement ( $h_m$ ), and the elastic unloading stiffness ( $S$ ) defined as the slope of the upper portion of the unloading curve during the initial stages of unloading (also called the contact stiffness) [67]. A power-law fit through the upper third to half of the unloading data, shown in Figure 3.8, intersects the depth axis at  $h_t$ .

Hardness and elastic modulus are determined through load/displacement curve as for the example below [68].

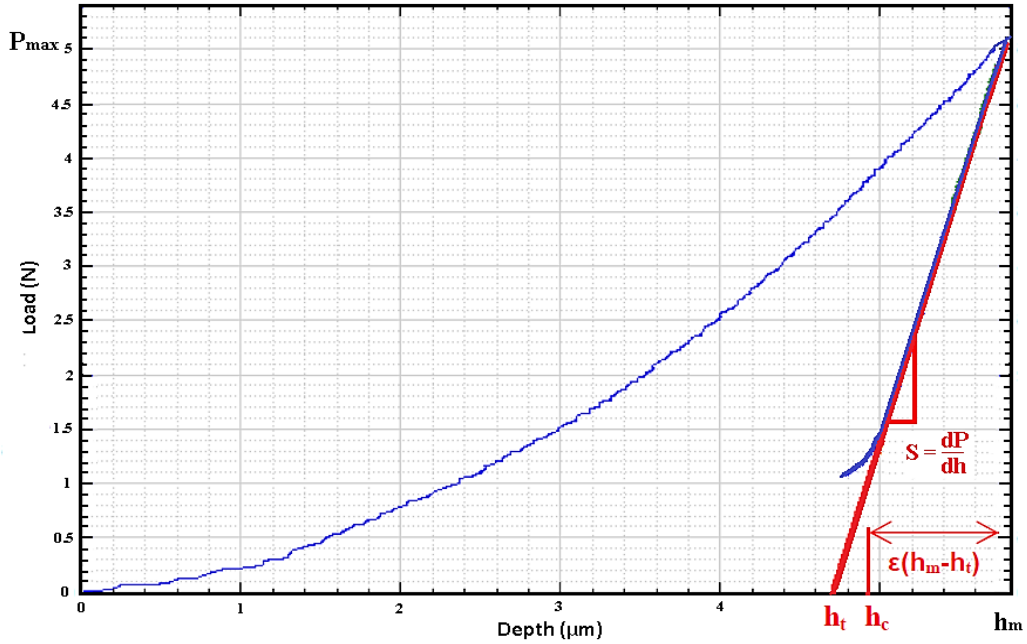


Figure 3.8: Hardness (H) and elastic modulus (E) are determined through load/displacement curve. A power-law fit through the upper third to half of the unloading data line intersects the depth axis at  $h_t$ . The stiffness  $S$ , is given by the slope of this line (adapted from Alexis Celestin).

The hardness (H) is determined from the maximum load ( $P_{max}$ ) divided by the projected contact area ( $A_C$ ):

$$H = \frac{P_{max}}{A_C} \quad (3.4)$$

The contact area ( $A_C$ ) is calculated by evaluating the indenter area function, which will depend on the diamond geometry of the indenter and at low loads by an area correction. For perfect Berkovich and Vickers indenters (as in this case), the area function is  $A_C=24.5h_c^2$ . The contact depth,  $h_c$ , is calculated as:

$$h_c = h_{max} - \epsilon \frac{P_{max}}{S} \quad (3.5)$$

where  $\epsilon$  is a constant that depends on the geometry of the indenter, and  $h_{\max}$  is the maximum displacement. The stiffness (S) is given by the slope of the straight part of the unloading curve. The  $\epsilon$  value of 0.75 was recommended based on empirical observations and has become the standard value used for analysis [67].

The Young's modulus (E) of the tested material can be obtained from:

$$E = \frac{1}{(1 - \nu^2) \left( \frac{1}{E_r} + \frac{1 - \nu_i^2}{E_i} \right)} \quad (3.6)$$

where  $E_i$  and  $\nu_i$  are the Young's modulus and Poisson coefficient of the indenter, respectively, and  $\nu$  is the Poisson coefficient of the tested sample. The reduced modulus ( $E_r$ ) is given by:

$$E_r = \frac{\sqrt{\pi}}{2} \frac{S}{\sqrt{A_c}} \quad (3.7)$$

Surface hardness obtained with indentation can be correlated with unconfined compressive strength (UCS) of the material [69]. The correlations have been used extensively in the field of rock mechanics. Based on the results from indentation tests conducted on shale samples, indentation parameters also show interdependence, that is, as one value increases, the other increases too [70]. A standard indentation test was recommended by ISRM and Equation 3.8 was suggested for the prediction of UCS from indentation hardness index (IHI) [71]:

$$UCS = 3.1 \cdot IHI^{1.09} \quad (3.8)$$

where UCS is in MPa and IHI in kN/mm.

### 3.5.8 Flow-through Experiments

In order to test the pipe expansion's capability to seal the microannular gas flow, Pre- and post-expansion multi-rate gas flow-through testing was conducted on composite samples with the pre-manufactured microannulus and without it (control). The microannulus was created by turning the inner pipe continuously within the first 26 hours of cement hydration leading to debonding of the cement/inner pipe interface. After this period samples were cured in the water bath for minimum hydration period of 28 days. Nitrogen gas was selected as the working fluid to simulate gas migration through the microannulus, as it is non-reactive with the cement paste and often used in foamed cements. Testing pre-expansion was done to check the existence of the microannular gas flow and estimate the size of the sample's microannulus by using the linear Darcy flow equation for gas. All experiments were done in the lab at ambient conditions.

The experiment starts by screwing the tubing fittings into the threaded holes on the outlet (bottom) and inlet (top) side of the outer pipe and connecting them with the compression fittings of the Teflon tubing manifold. This allowed nitrogen gas to be injected into the sample from four different sides of the sample, 90° apart, as shown on Figures 3.9. and 3.10. A cylinder with nitrogen gas was pressurized at desired starting inlet pressure of 15 psi (103 kPa), and upon stabilization of pressures the flow rate was kept constant at 0.003 ft<sup>3</sup>/min (85 ml/min) with the gas flow meter valve. The flow through the sample would indicate the existence of microannular gas flow pre-expansion. Pressure differential ( $P_{\text{inlet}} - P_{\text{outlet}}$ ), recorded by inlet and outlet pressure transducers, is the only variable which was used in calculations of effective permeability of the pre-manufactured microannulus,  $K_{\text{ef}}$  (modified Eq. 2.1) [33]:

$$K_{ef} = \frac{1424q\mu ZT\Delta L}{\pi(r_{Oinn}^2 - r_{Iout}^2)} \cdot \frac{1}{(P_{inlet}^2 - P_{outlet}^2)} \quad (3.8)$$

$q$  – nitrogen flow rate [Mcf/day]       $K_{ef}$  – effective perm. of microannulus [mD]  
 $r_{Iout}$  – ID of outer pipe [ft]       $r_{Oinn}$  – OD of inner pipe [ft]  
 $\mu$  – gas viscosity [cP]       $Z$  – gas deviation factor  
 $T$  – temperature [°R]       $\Delta L$  – distance between P transducers [ft]  
 $P_{inlet}$  – inlet pressure [psi]       $P_{outlet}$  – outlet pressure [psi]

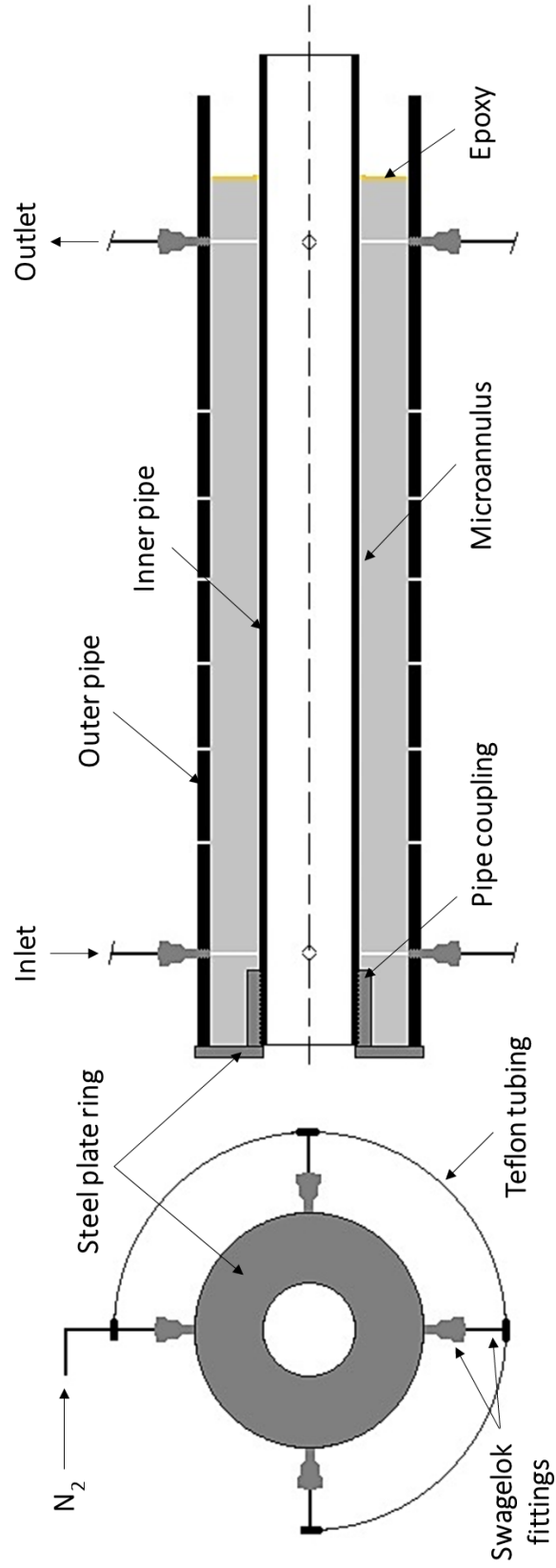
Upon pressure stabilization nitrogen flow rate was kept constant at approximately  $q=0.003 \text{ ft}^3/\text{min}$  (85 ml/min) which converted to field units makes 0.0042 Mcf/day. The gas deviation factor for nitrogen at ambient conditions was taken to be  $Z=1$  and viscosity  $\mu=0.018 \text{ cP}$ . All the flow-through tests were conducted at ambient conditions of  $T=534.7^\circ\text{R}$  (75°F, 24°C). The distance between inlet and outlet ports ( $\Delta L$ ) was 1.33 ft (40.64 cm) and the area of the cemented annular space was calculated taking inner radius of the outer pipe,  $r_{Oinn}=0.15 \text{ ft}$  (4.6 cm), and outer radius of the inner pipe,  $r_{Iout}=0.10 \text{ ft}$  (3.05 cm).

From the Equation 3.8, the effective permeability is inversely proportional to the pressure differential, meaning that smaller  $\Delta P$  would indicate a larger microannulus. Due to preferential pathway of nitrogen gas, effective permeability obtained can be accounted for in its entirety by the flow through the microannulus ( $K_{ef}$ ), as both casing and cement have low permeability and therefore are not providing substantial migration pathways. The size of that microannulus can be estimated with the Equation 3.9 (modified Eq. 2.2) [33]:

$$w = \sqrt{\frac{K_{ef}}{8.4 \cdot 10^{13}}} \quad (3.9)$$

$w$  – size of the microannulus (m)       $K_{ef}$  – effective permeability [mD]





**Bottom view**

**Cross-sectional view**

Figure 3.9: Composite sample flow-through schematic. Bottom view shows manifold with Swagelok fittings and Teflon tubing. Cross-sectional view shows location of the inlet and outlet ports with respect to the pre-manufactured microannulus between the inner pipe and cement sheath. Epoxy was added to prevent nitrogen flow from venting to atmosphere.

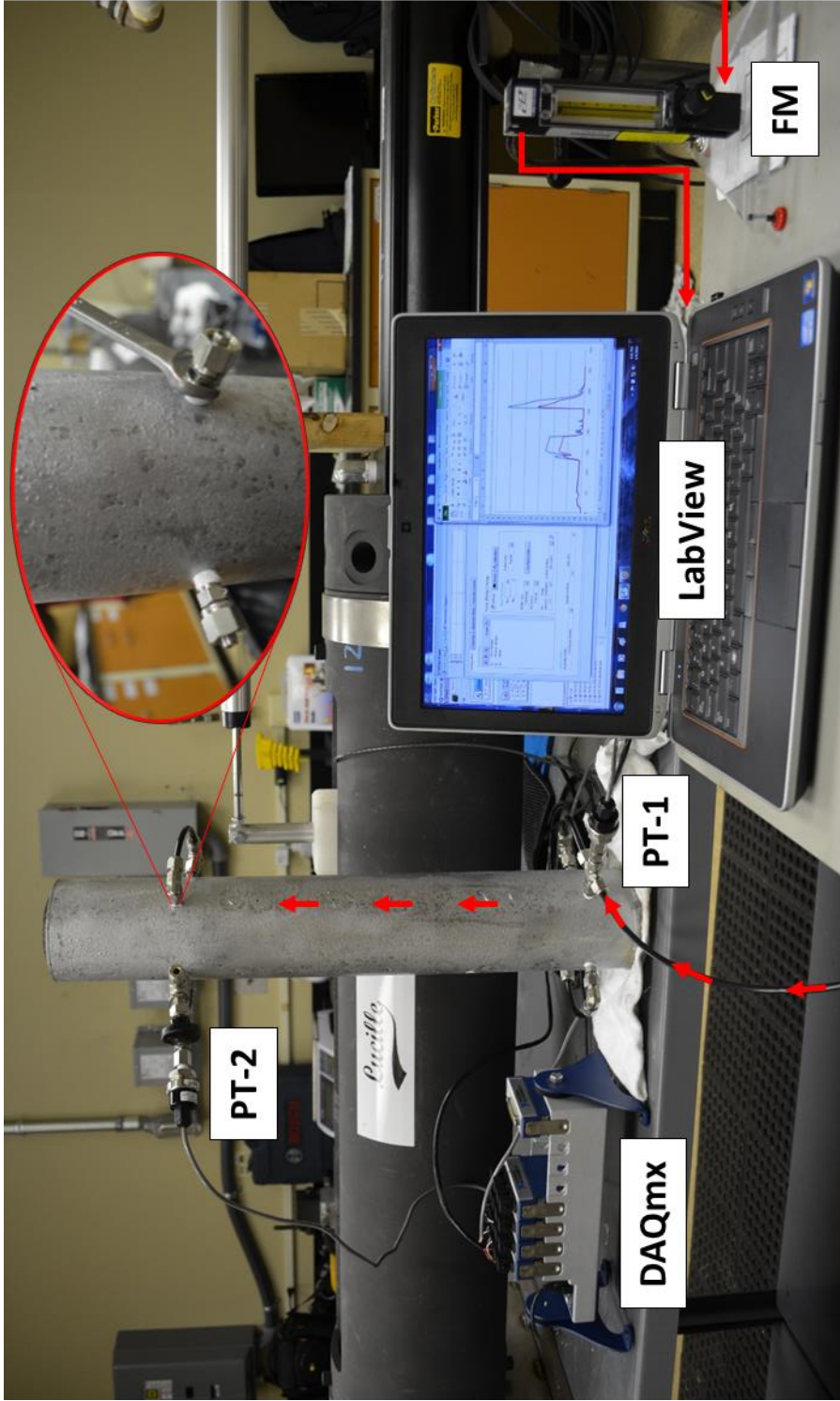


Figure 3.10: Flow-through experimental setup. The flow meter (FM) controls nitrogen gas flow (red arrows) throughout the experiment. Gas flows and enters the composite sample on the inlet manifold where the inlet pressure transducer (PT-1) records the inlet pressure. Gas flows through the sample's pre-manufactured microannulus and the pressure recording on the outlet manifold's pressure transducer (PT-2) provides the information of whether there is a connectivity and microannular gas migration through the composite sample. Pressure transducers are connected to the data acquisition system (DAQmx) and pressures are monitored and recorded in real time on the computer screen (LabView software). Magnified view shows installation of the Swagelok fittings which were sealed by Teflon tape to prevent any nitrogen leakage (gas flow-through composite sample schematic previously shown on Figure 3.5).

After conclusion of the flow-through tests, the gas cylinder was closed and the gas manifold disassembled. The small holes on the outer pipe were unplugged and the sample was then prepared for expansion. Flow-through testing post-expansion was conducted within 1 hour, 24 hours, and 60 days after expansion to examine if the expansion was successful in sealing the microannulus and test the seal integrity. The holes were sealed with epoxy immediately after expansion. After re-connecting the gas manifold, multi-rate nitrogen gas flow-through experiments were conducted. Initial inlet pressure was kept at 25 psi (172 kPa) and it was increased by 25 psi (172 kPa) every five minutes until the final inlet pressure of 100 psi was reached. No pressure recording on the outlet pressure transducer would indicate sealing of the microannular gas flow.

## CHAPTER 4: RESULTS

### 4.1 Visual Observations During and Post-expansion

Tubular expansion resulted in increase of pipe diameter at the expense of volume occupied by the cement sheath. The result is a compression of cement matrix and release of free pore water through “porosity” holes of the outer pipe, followed by protrusion of the paste-like material, as seen in Figure 4.1. In all further discussion, the term “compressed” will be used for the cement sheath and the term “expanded” will be used for the pipe.

Alkalinity measurements of the collected fluid samples with the pH paper showed a pH of between 13 and 14 indicating that the fluid sample was most likely the cement free pore water. Inductively coupled plasma (ICP) mass spectrometry of fluid samples detected mainly  $\text{Na}^+$  and  $\text{K}^+$ , with significant increase in concentrations of  $\text{Ca}^{2+}$ ,  $\text{Fe}^{3+}$ ,  $\text{Mg}^{2+}$  and  $\text{S}^{6+}$  with expansion ratio. The concentration of these ions in the effluent sample increased more than three times in the sample expanded 8% compared to one expanded at 4% expansion ratio. The results shown in Table 4.1 suggest that primarily pore water is squeezed out of the cement sheath.

Table 4.1: Results of the ICP mass spectroscopy conducted on fluid samples collected during expansion at 4% and 8% expansion ratios. High concentrations of  $\text{K}^+$  and  $\text{Na}^+$  suggest that free cement pore water is being squeezed out of the sample. Large increase in concentration of  $\text{Ca}^{2+}$ ,  $\text{Fe}^{3+}$ ,  $\text{Mg}^{2+}$  and  $\text{S}^{6+}$  with expansion ratio indicates dissolution of certain minerals within the cement.

<b>Ion concentration [ppm]</b>	<b><math>\text{Al}^{3+}</math></b>	<b><math>\text{Ca}^{2+}</math></b>	<b><math>\text{Fe}^{3+}</math></b>	<b><math>\text{S}^{6+}</math></b>	<b><math>\text{Mg}^{2+}</math></b>	<b><math>\text{K}^+</math></b>	<b><math>\text{Na}^+</math></b>
<b>4% sample</b>	4.50	8.04	1.45	10.60	14.48	1,760.16	1,282.48
<b>8% sample</b>	5.80	27.70	4.68	33.40	41.13	2,085.65	1,442.54



Figure 4.1: Photo of a composite sample after expansion with the 8% expansion ratio cone. Fully hydrated cement, with a paste-like consistency, has been squeezed out from the holes on the outer pipe together with free cement pore water. The magnified view showing cement paste squeezed out from larger holes.

A cross section of the cement/casing sample was obtained by cutting the specimen to investigate the integrity of the cement sheath (Figure 4.2). Mini-cores which were drilled from the matrix were easily crushed with fingertips indicating a change in consistency and loss of integrity. The post-expanded cement sheath was soft enough to be scraped with a small spatula. The cut samples were then wrapped in a plastic wrap and returned to the water bath for further hydration. After a period of five days, the cross-sectioned disks were visually observed and subjected to a qualitative hardness test. Five days post-expansion resulted in a different behavior primarily indicating that cement regained most of its consistency.

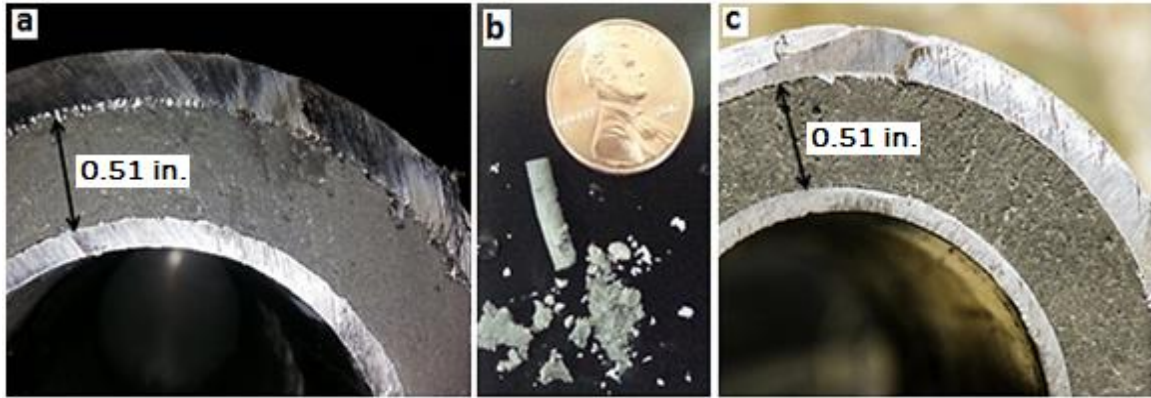


Figure 4.2: a. a cross-section of the composite sample immediately after 8% expansion exhibiting the cement sheath with softer consistency; b. drilled cement mini-cores from the composite sample were easily crushed under very small forces (between fingertips); c. a cross-section of the same composite sample five days after expansion. The cement regained its strength and there was no fracturing and deformation upon visual inspection. The width of the cement sheath was 0.51 in. (1.3 cm).

#### 4.2 Optical Microscopy

Images of the control samples showed presence of air voids (bubbles) on both vertical and horizontal thin sections. Some of the air bubbles had a diameter of over  $3.94 \cdot 10^{-3}$  in. (100  $\mu\text{m}$ ). Cement matrix appeared to have had more pores than the expanded samples, with larger presence of scattered portlandite crystals, but not on the walls of air voids and larger pores (shown in Tables 4.2 and 4.3).

On both regular and polarized images of expanded samples with 4% and 8% expansion ratio, collapse of air bubbles under expansion force was observed. Polarized images showed presence of bright colorful shapes which represent the mineral portlandite precipitating on the pore walls as a product of rehydration. Portlandite crystals tend to grow in spaces initially occupied by water [6]. Cement free pore water propagation due to pipe expansion most likely triggered this precipitation of new minerals within the collapsed bubbles and smaller pores. Fractures which seem to have spread from the collapsed pores could have been made either during sample cutting or due to stress during expansion.



Table 4.2: Microscopy images of cement sample's horizontal thin sections pre and post-expansion (4% and 8% expansion ratio). Images of expanded samples showing collapse of large air voids (AB) and precipitation of portlandite (P) within the pores. Fractures (F) were also observed within the matrix as a result of stresses during expansion.

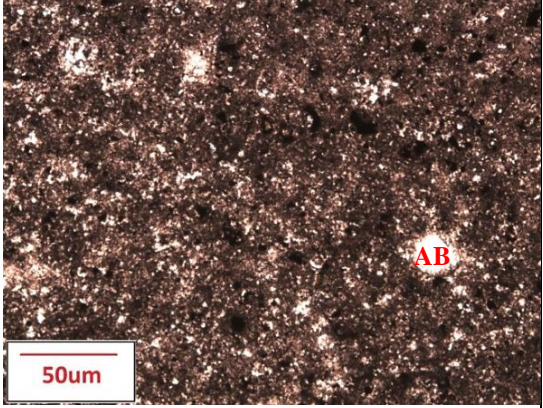
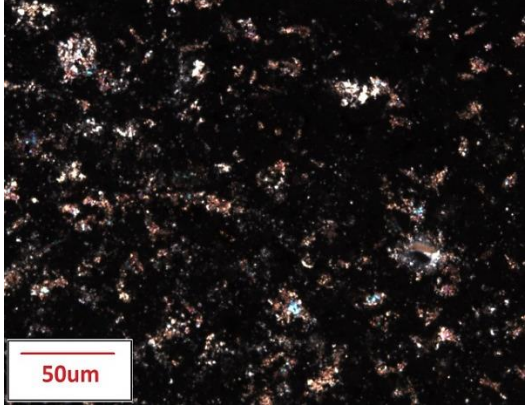
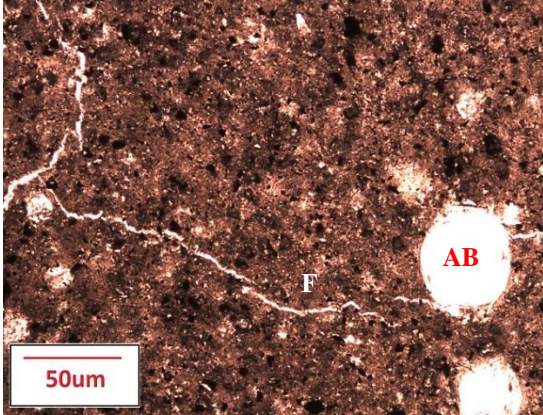
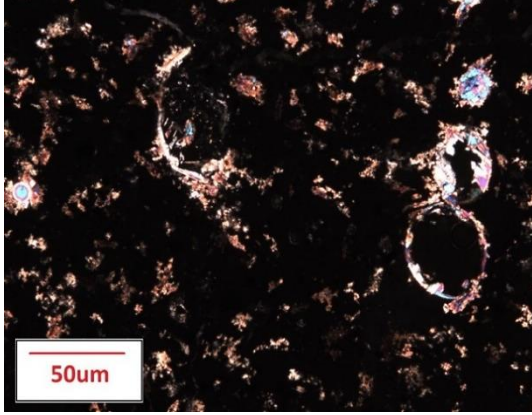
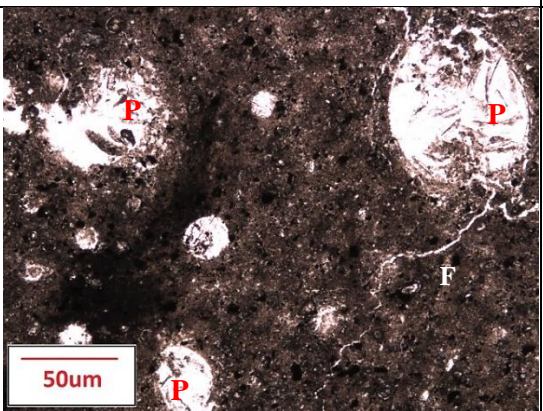
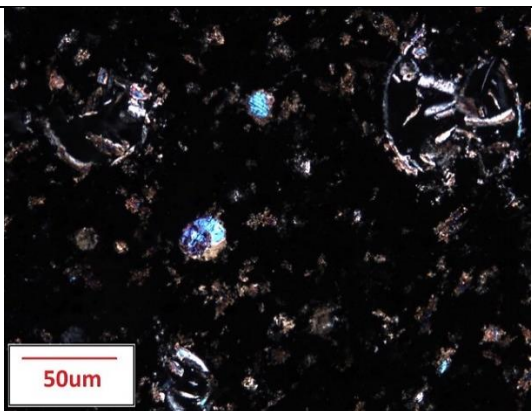
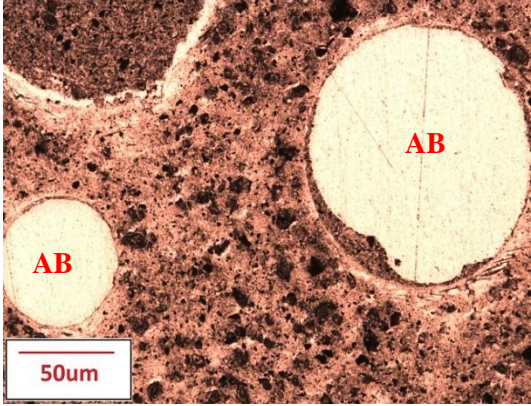
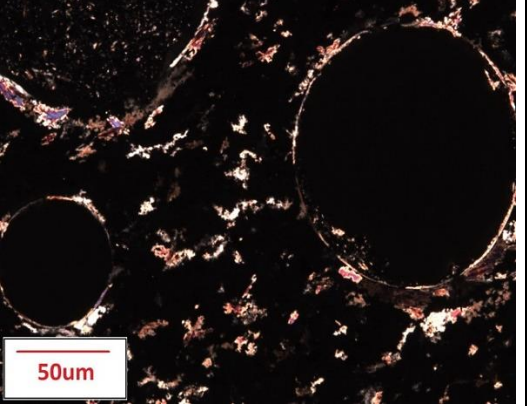
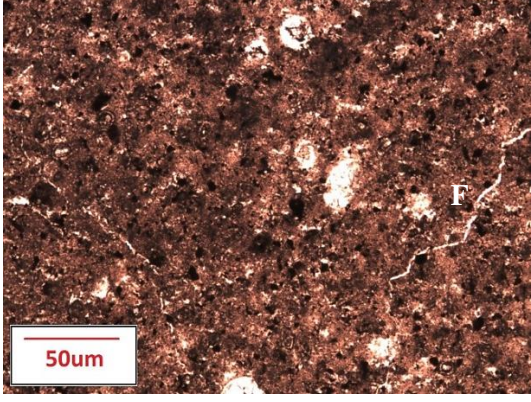
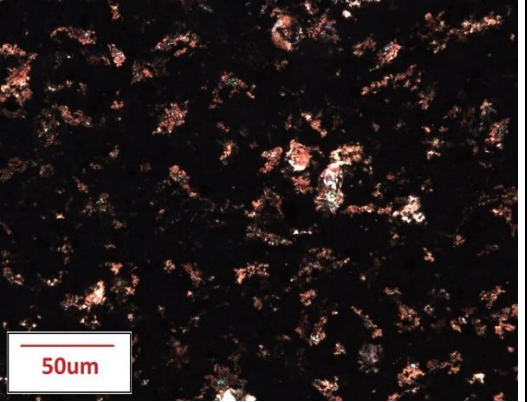
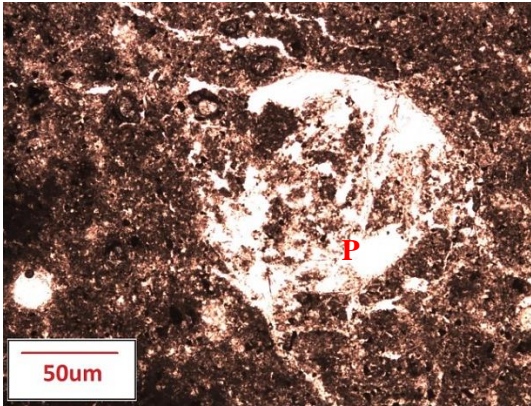
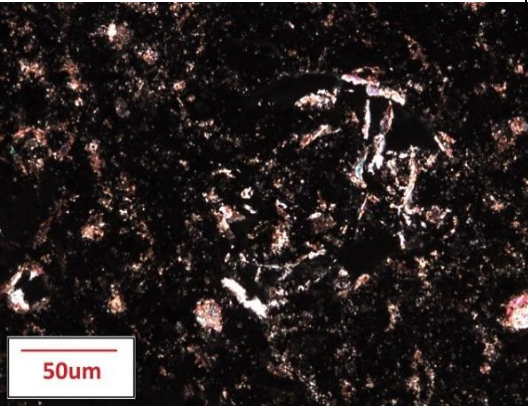
	Regular light	Polarized light
Control		
4% expansion		
8% expansion		



Table 4.3: Microscopy images of cement sample's vertical thin sections pre and post-expansion (4% and 8% expansion ratio). Images of expanded samples showing collapse of the air voids and precipitation of portlandite crystals on the walls and within collapsed pores, as well as fracturing (F) of cement matrix.

	Regular light	Polarized light
Control		
4% expansion		
8% expansion		



### 4.3 Thermogravimetric Analysis (TGA) of Cement

TGA was run on the control sample, cement samples five days post-expansion (Appendix D), and on cement samples six months post-expansion. To determine and quantify mineralogical composition of the cement before and after expansion test, a temperature range correlating to the weight loss for each mineral's decomposition temperature peak is pre-determined. Located in the Table 4.4 below are all the temperature ranges in endothermic peaks of most abundant hydrated cement minerals. It has to be recognized that there are interference effects at low temperatures, depending on the drying procedures and the state of the material [5].

Table 4.4: Temperature ranges with endothermic peaks of different minerals which can be found in cement [5].

<b>Hydrated cement mineral [chemical formula]</b>	<b>Temperature range of mineral decomposition, °F [°C]</b>
Ettringite [ $\text{Ca}_6\text{Al}_2(\text{SO}_4)_3(\text{OH})_{12}\cdot 26\text{H}_2\text{O}$ ]	248-266 [120-130]
C-S-H [ $3\text{CaO}\cdot 2\text{SiO}_2\cdot 3\text{H}_2\text{O}$ ]	Below 302 [150]
Gypsum [ $\text{CaSO}_4\cdot 2\text{H}_2\text{O}$ ]	284-338 [140-170]
Portlandite [ $\text{Ca}(\text{OH})_2$ ]	842-1022 [450-550]
Calcite [ $\text{CaCO}_3$ ]	1382-1562 [750-850]

Based on published data on TGA measurements of ordinary Portland cement, the derivation was made for estimating initial quantity of portlandite in the cement paste. In determined endothermic range of 842-1022°F (450-550°C), approximately 25% of the total mineral's weight is being lost [72]. This correlation was used to determine the initial quantity of portlandite in the cement samples.

Results of the control sample showed weight loss in portlandite mineral of 5.7%, shown in Figure 4.3. Knowing that approximately 25% of total portlandite weight is being lost in that endothermal region, this means that there was approximately 23.4% of portlandite in the control cement sample. The weight loss between 167-302°F (75-150°C) was 6.5%, which contained endothermal peaks of water, ettringite, gypsum and C-S-H. The last endothermal peak corresponds to weight percentage of calcite (0.64% weight loss). The presence of calcite can be predominantly ascribed to carbonation of the sample.

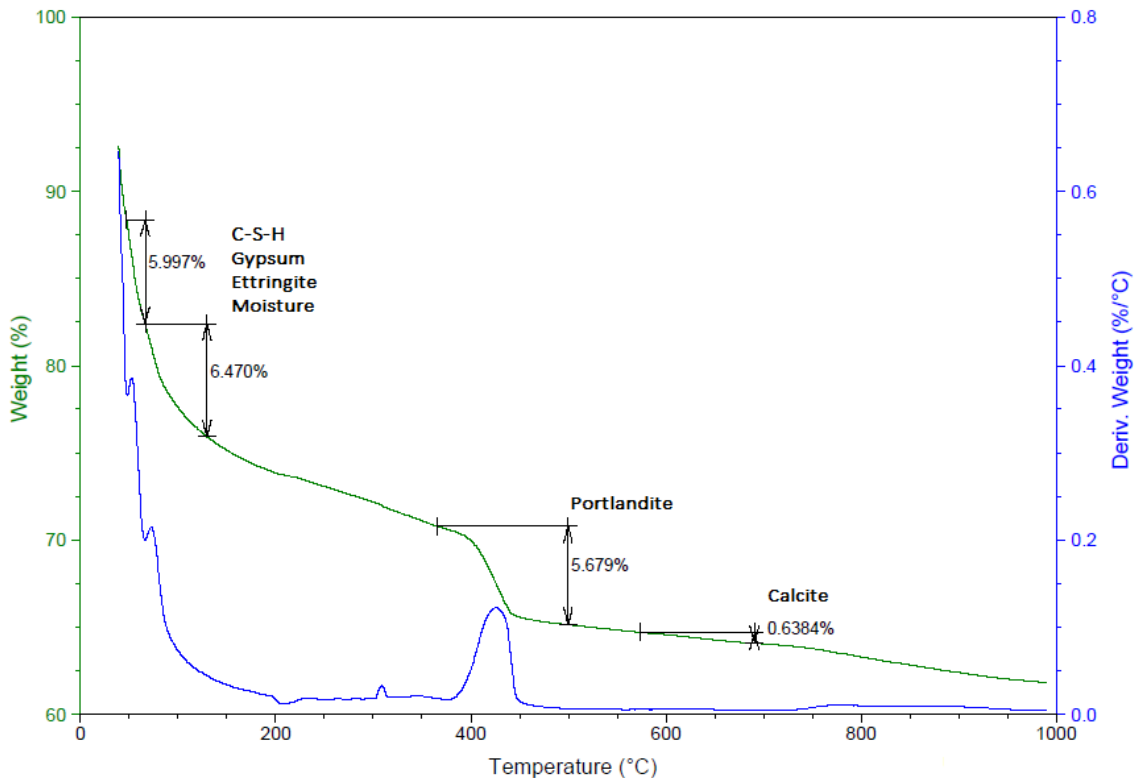


Figure 4.3: Plot of TGA for 7-month old control sample. The green (upper) line is showing weight percentage lost, while the blue line shows endothermal peaks (°C) of the weight percentage lost per unit of heat. In the range of 167-302°F (75-150°C), the total weight loss was 6.5%. This loss corresponds to the amount of moisture, and mineral phases of gypsum, ettringite and C-S-H in the sample. The next endothermal peak at 797°F (425°C) is portlandite peak. The weight loss of 5.7% indicates that there was initially approximately 23% portlandite in the control sample. Last endothermal peak at 1202°F (650°C) is calcite peak and small weight loss of 0.64% indicates minor presence of calcite.

Sample expanded with 2% expansion ratio cone showed slightly different results than the control sample, as shown in Figure 4.4. Weight loss of 9% in minerals with endothermal peaks below 302°F (150°C) was observed, which corresponds to increased presence of moisture, gypsum, ettringite and/or C-S-H minerals. Weight loss of portlandite was registered to be 5.77%, indicating that after 2% expansion the concentration of this mineral (23.6%) did not differ from control sample after six months of rehydration. Increased presence of calcite (2.9% weight loss) was observed after this expansion.

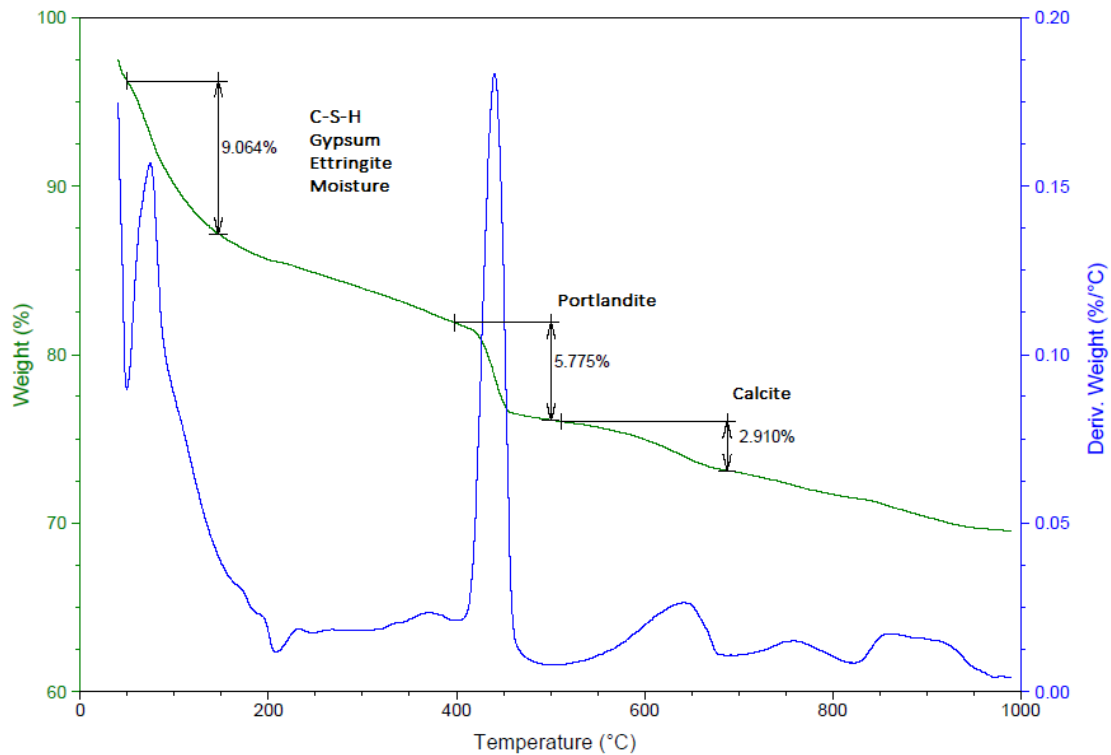


Figure 4.4: TGA plot of cement sample after 2% expansion and six months of rehydration. The green (upper) line is showing weight percentage lost, while the blue line shows endothermal peaks (°C) of the weight percentage lost per unit of heat. The peak observed in the range of 167-302°F (75-150°C), correspond to the weight loss of moisture and mineral phases of gypsum, ettringite and C-S-H (9%). The portlandite peak at 788°F (420°C) showed weight loss of 5.77% indicating that there was approximately 23.6% portlandite in the sample expanded with 4% expansion ratio cone. Last endothermal peak at 1202°F (650°C), corresponding to the calcite peak, showed weight loss of 2.9%, indicating increased presence of calcite six months after expansion, compared to the control sample.

Thermal analysis of the sample which was expanded at 4% expansion ratio, shown in Figure 4.5, showed weight losses of 9% at endothermal peaks under 302°F (150°C). This means that both concentration of moisture and mineral group of ettringite, gypsum and C-S-H did not change significantly compared to the 2% expanded sample. The observed weight loss in portlandite mineral of 5.6% indicated that the portlandite concentration remained at approximately 23% six months post-expansion with 4% expansion ratio cone. Presence of calcite increased, (2.1% weight loss) compared to the control sample, and was similar to the one in the sample expanded with 2% expansion cone.

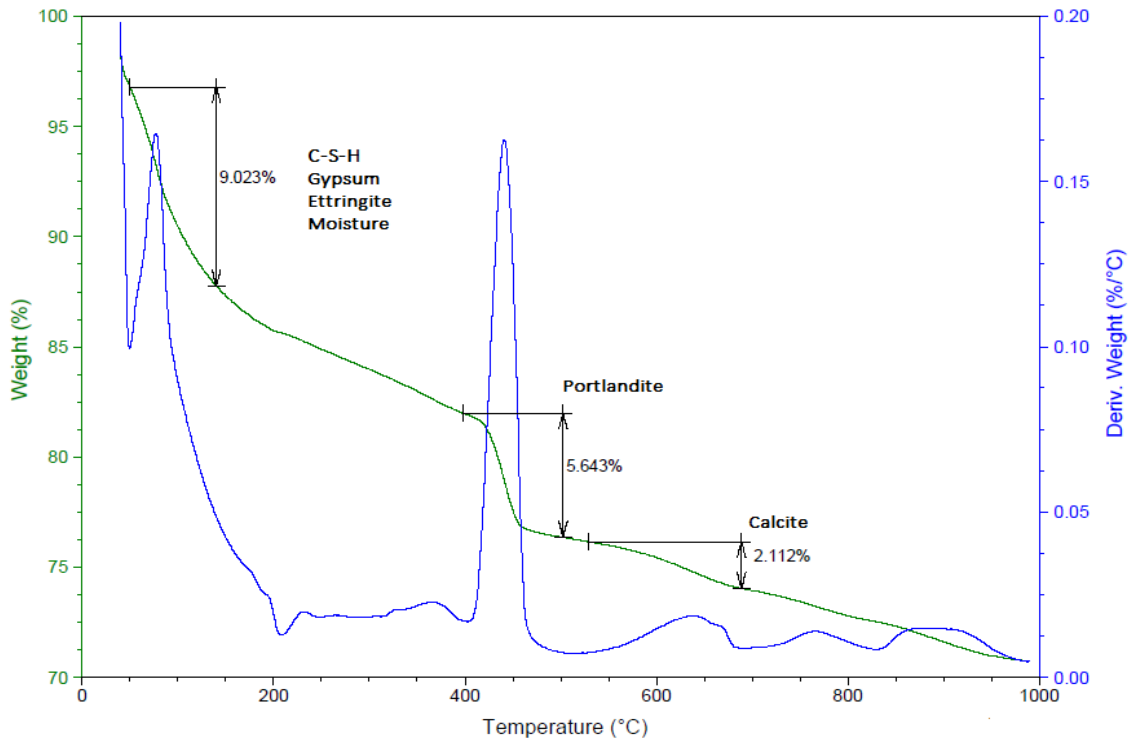


Figure 4.5: TGA plot of cement sample six months after 4% expansion. The green (upper) line is showing weight percentage lost, while the blue line shows endothermal peaks (°C) of the weight percentage lost per unit of heat. The distinctive peak observed in below 302°F (150°C), correspond to the weight losses of moisture (8%) and mineral phases of gypsum, ettringite and C-S-H (5%). The portlandite peak at 788°F (420°C) showed weight loss of 4% indicating that there was 17% portlandite in the sample expanded with 4% expansion ratio cone. Last endothermal peak at 1202°F (650°C), corresponding to the calcite peak, showed weight loss of 0.77%, indicating minor presence of calcite due to carbonation of the cement sample during preparation.

Sample expanded with 8% expansion ratio cone had similar results to two previous expanded samples six months post-expansion (Figure 4.6). Weight loss of 9.55% in minerals with endothermal peaks below 302°F (150°C) was observed, which corresponds to increased presence of moisture, gypsum, ettringite and/or C-S-H minerals, compared to the control sample. Weight loss of portlandite was registered to be 6%, indicating that after 8% expansion and six months of rehydration, the concentration of this mineral returned to 24% which is in the range of hydrated Portland cements. Weight loss of calcite (1.31%) indicated smaller concentration of that mineral than in cases after 2% and 4% expansion.

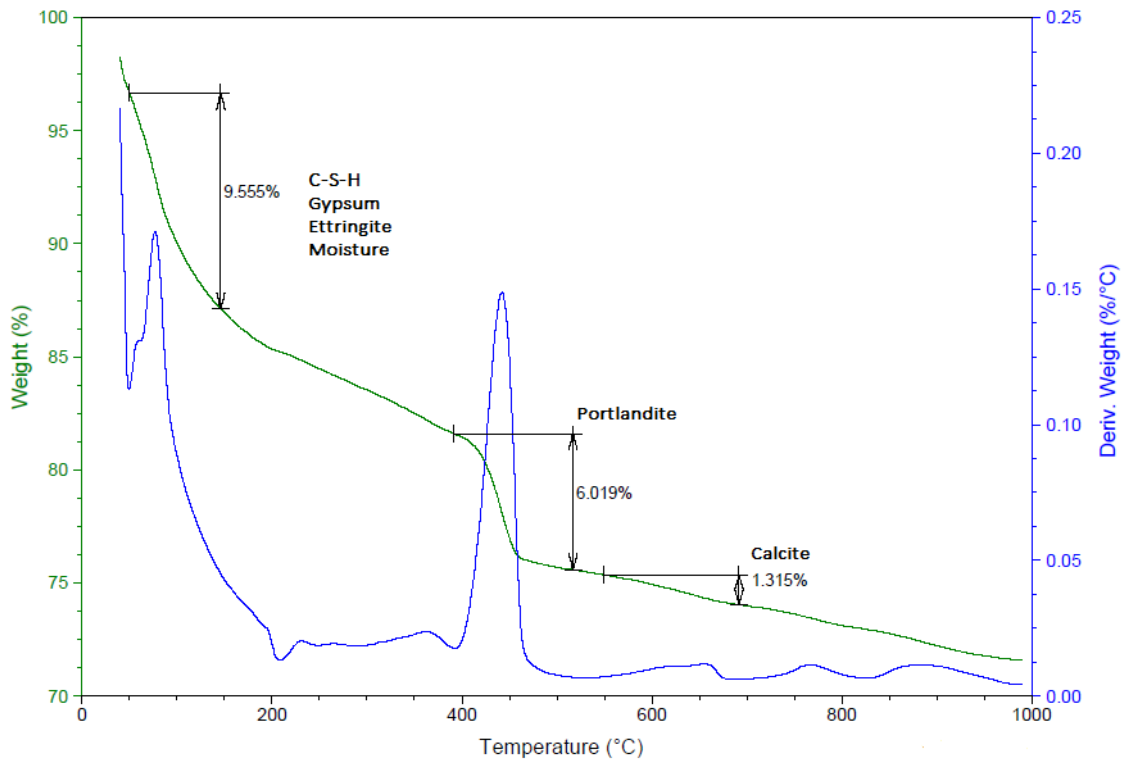


Figure 4.6: TGA plot for cement sample six months post-expansion at 8% expansion ratio. The green (upper) line is showing weight percentage lost, while the blue line shows endothermal peaks (°C) of the weight percentage lost per unit of heat. In the range of 167-302°F (75-150°C), weight loss of 9.55% corresponds to the larger amount of moisture within the sample, and also mineral phases of gypsum, ettringite and C-S-H. The next endothermal peak at 788°F (420°C) showed portlandite weight loss of 6% indicating initial concentration of 24%. Last endothermal peak at 1202°F (650°C) showed 1.31% weight loss of calcite.

#### 4.4 Microhardness Test

In order to investigate the effect of expansion on the mechanical properties of the cement matrix, microhardness tests were performed on the control and compressed cement samples. Every sample was tested for hardness with indentation on five points, starting from the side of the inner pipe to the outer pipe side of the sample, as shown in Figure 4.7. Tables 4.5 and 4.6 summarize the main numerical results for control sample, and cement samples six days and six months post-expansion with 2%, 4% and 8% expansion ratio cones.

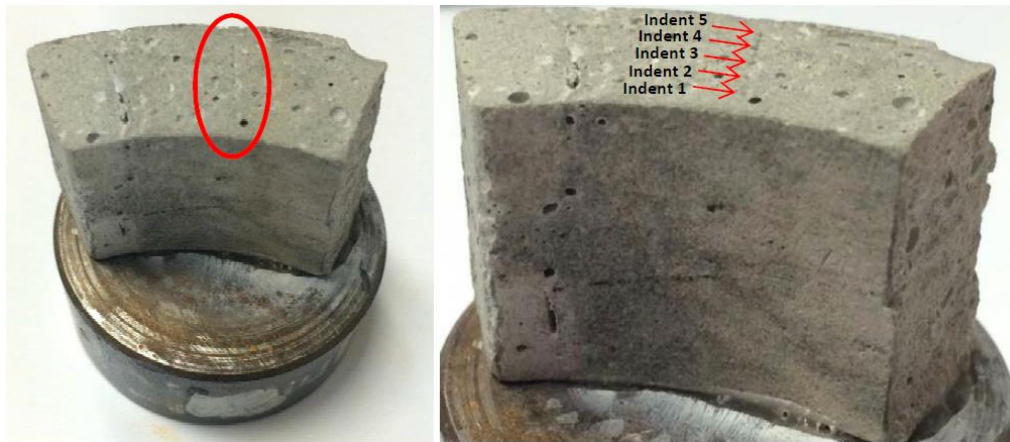


Figure 4.7: Indentation points of the cement sample. Indents range from the inner pipe side of the sample (Indent 1) to the outer pipe side of the sample (Indent 5).

The results are expressed as calculated values of cement hardness and Young's Modulus based on penetration depth of the indenter probe, showing average values and standard deviations. It should be considered that the large variations in results can occur when the surface roughness is in the same size range as the indentation. Features such as air bubbles can interfere, although these effects are present on all sample surfaces and are minimized by using microscope-guided positioning of the indents.

The indentation results of the samples six days post-expansion show decrease in hardness for all samples, where highest decrease of 30% was recorded in the samples which underwent 4% and 8% expansion.

Table 4.5: Summary table (average) of the main numerical results for cement samples six days post-expansion. Hardness and Young's modulus show decrease for all expansion ratios with 30% decrease being the highest for 4% and 8% expansion.

<b>Sample</b>	<b>Hardness [Vickers]</b>	<b>Hardness [MPa]</b>	<b>Young's Modulus [MPa]</b>	<b>Max Depth [μm]</b>
Control	3.04±0.94	32.2±9.90	3973±587	167.4±4.5
2% expansion	2.70±0.37	28.5±3.9	3036±1700	176±11
4% expansion	1.96±0.32	20.7±3.4	1961±539	207±16
8% expansion	1.92±0.77	20.3±8.1	1196±298	172±60

The indentation results of the samples six months post-expansion showed average increase in cement's hardness after pipe expansion. The hardness increased the most in the sample 8% post-expansion (20% increase), as tabulated in Table 4.6.

Table 4.6: Summary table (average) of the main numerical results for cement samples six months post-expansion. Hardness and Young's modulus show increase in hardness in all samples post-expansion.

<b>Sample</b>	<b>Hardness [Vickers]</b>	<b>Hardness [MPa]</b>	<b>Young's Modulus [MPa]</b>	<b>Max Depth [μm]</b>
Control	2.89±0.20	30.6±2.2	3135±	170±4
2% expansion	3.22±0.19	34.1±2.0	5034±956	158±5
4% expansion	3.16±0.29	33.5±3.1	2823±1003	163±7
8% expansion	3.51±0.26	37.2±2.7	4656±1606	152±6

#### 4.5 Mechanical Effects of Expansion on Pipe (Casing)

By using known correlations adapted from previous research [54], [53], different pipe parameters and pressure ratings were calculated to determine the detrimental effects expansion had on the pipe. The main parameters associated with detrimental effects of expansion were focused include: pipe shortening, reduction of wall thickness, OD/t increase, collapse ( $P_c$ ) and burst ( $P_{br}$ ) pressure ratings (Equations 3.2 and 3.3, respectively).

The calculated values are shown in Table 4.7. and they assume the loss in pipe wall thickness of 0.6 of the percentage of expansion ratio [53] and pipe length shortening of 0.2 of the percentage of expansion ratio [54], e.g., an expansion of 8% would cause a decrease in wall thickness of 4.8% and length shortening of 1.6%.

Table 4.7: Expansion and pipe parameters. Decrease in the wall thickness and increase in OD/t affected the collapse rating, decreasing it up to 20% for the 8% expansion ratio.

<b>Actual Expansion Ratio [%]</b>	<b>Pipe OD [in.]</b>	<b>Wall Thickness, t [in.]</b>	<b>OD/t</b>	<b>Length [in.]</b>	<b><math>P_{br}</math> [psi]</b>	<b><math>P_c</math> [psi]</b>
0	2.375	0.109	21.79	24.0	2811.1	2357.1
1.46	2.405	0.108	22.26	23.9	2751.9	2257.5
3.45	2.445	0.107	22.91	23.8	2674.0	2126.1
7.43	2.526	0.104	24.25	23.6	2525.6	1875.9

The calculated collapse pressure rating for the pipe expanded with the 8% expansion ratio cone decreased by 20% compared to initial pipe rating (Figure 4.8). The calculated burst pressure rating, however, does not take into account the isotropic strain hardening which adds to the material's burst capabilities and making it more resistant [52].



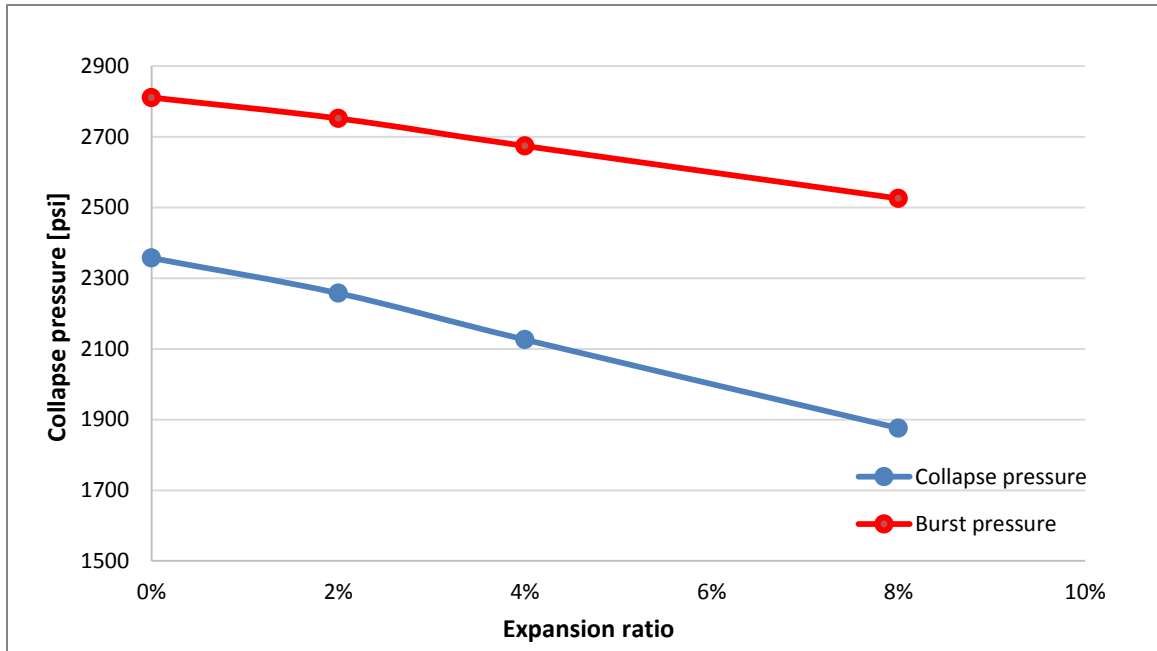


Figure 4.8: Plot showing decrease in collapse and burst pressure ratings after expansion with 2%, 4% and 8% expansion ratio cones. Calculations of burst rating showed a decrease of 10% for the 8% expansion ratio, while the collapse rating decreased over 20% for the same expansion ratio.

Axial forces ( $F_e$ ) were recorded during expansion with an integrated load cell. The expansion was first done on welded pipe samples which were not cemented (free annular space). This was done to compare the values of those obtained during expansion of the composite cement samples. These recordings and the results of axial stress ( $\sigma_z$ ) calculations are shown in Table 4.8 and Figure 4.9.

Table 4.8: Force measurements obtained during pipe expansion and calculated axial stresses. Values are for expansions with pipe only ( $F_e$ ,  $\sigma_z$  – pipe) and for composite cement sample ( $F_e$ ,  $\sigma_z$  – sample).

Actual Expansion Ratio [%]	Cone OD [in.]	$F_e$ - pipe [lbf]	$\sigma_z$ - pipe [psi]	$F_e$ - sample [lbf]	$\sigma_z$ - sample [psi]
1.46	2.189	1943	2504.3	2815	3627.8
3.45	2.232	3513	4527.3	4295	5535.1
7.43	2.317	8267	10653.8	12596	16232.9

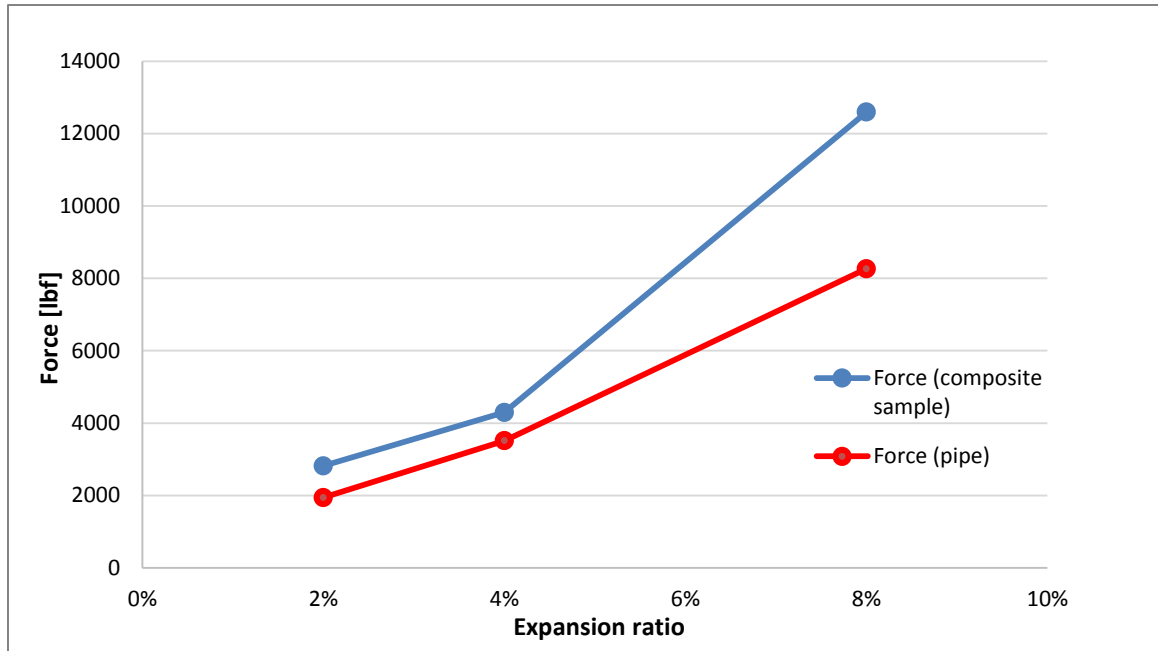


Figure 4.9: Plot of axial forces recorded during expansion with 2%, 4% and 8% expansion ratio cones. The increase in forces during expansion of composite samples accounts for the presence of the cement sheath behind the pipe and transfer of stress into cement.

#### 4.6 Gas Flow-through Experiments

The total of 15 samples with a pre-manufactured microannulus were made, out of which only 7 showed flow during multi-rate gas flow-through experiments. These samples were used for preliminary and concluding data, out of which five were tested for gas flow after pipe expansion at 2%, 4% and 8% expansion ratios.

Multi-rate gas flow-through experiments were run on each specimen pre-expansion, immediately after expansion (0 hours), 24 hours after expansion and 60 days after expansion. One of the composite samples (control sample) did not have the pre-manufactured microannulus and it did not undergo expansion. The control sample was tested for gas flow to establish whether gas flow through the cement sheath of the composite sample would be recorded.

The effectiveness of tubular expansion in sealing the annulus was monitored using the readings from the outlet pressure transducer. When the pressure transducer on the outlet side of the sample showed no recorded pressure post-expansion during gas flow-through experiments, it implied that the microannular flow was successfully remediated. The effective permeability of the microannulus is quantified using Darcy’s linear gas flow calculations. This value was used to estimate the size of the microannulus using known correlations.

#### 4.6.1 Gas Flow-through Test I – Control Sample

A multi-rate gas flow-through experiment was first performed on the sample without the pre-manufactured microannulus (results shown in Figure 4.10). This was done in order to establish that the design and accuracy of the pressure transducers as well as to check if there was a good bond at cement/pipe interface.

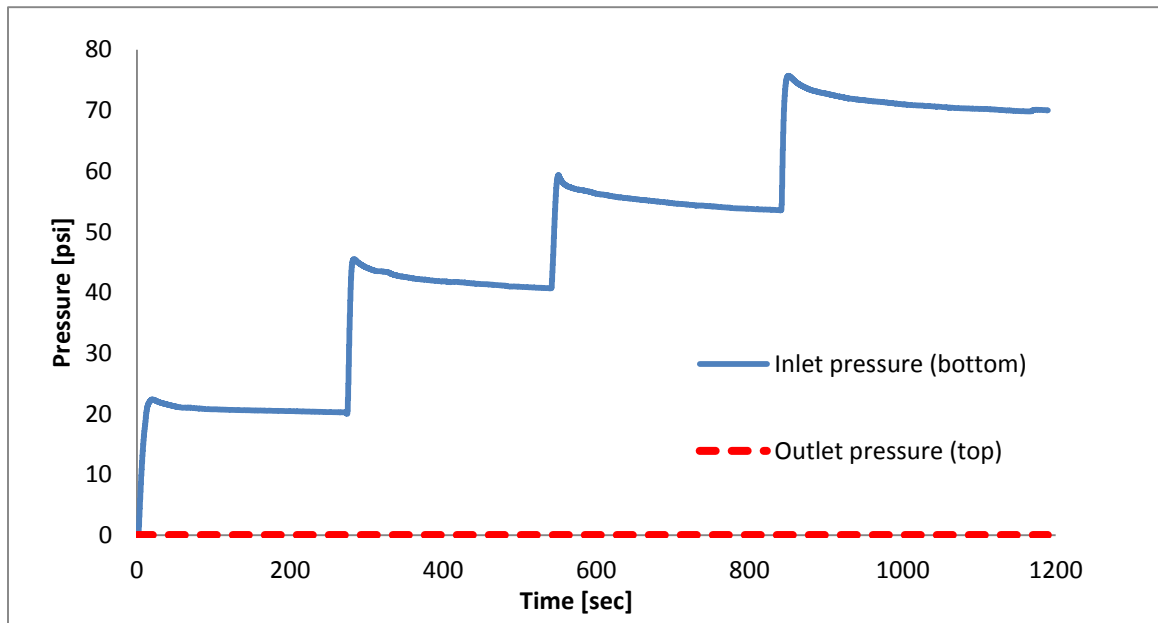


Figure 4.10: Multi-rate gas flow-through test data plot recorded on control sample without pre-manufactured microannulus. After a gradual increase of 25 psi (172 kPa) in inlet pressure on the gas cylinder every five minutes from 25 psi (172 kPa) to 100 psi (690 kPa), there was no recorded pressure on the outlet pressure transducer, confirming that there was no microannular gas flow.

The multi-rate gas flow-through procedure involved a gradual increase in inlet pressure by 25 psi (172 kPa) every five minutes from 25 psi (172 kPa) to 100 psi (690 kPa). There was no pressure recording on the outlet pressure transducer during this experiment, which confirmed that there was no flow through the entire composite specimen or at both cement/pipe interfaces.

#### **4.6.2 Gas Flow-through Test II – 2% Expansion**

The pre-expanded gas flow-through experiment on the first sample showed flow through the composite sample's microannulus and recorded pressure on outlet's pressure transducer, thus confirming the presence of a microannulus. Initial inlet pressure on the gas cylinder was 15 psi (103 kPa), and the gas flow was kept constant at 0.003 ft<sup>3</sup>/min (85 ml/min) upon pressure stabilization. The recorded time lag between inlet and outlet pressure transducer was five seconds, and after increasing the inlet pressure to 50 psi (345 kPa) the pressures recorded on the transducers increased to 32 psi (220 kPa) (inlet) and 9 psi (62 kPa) (outlet), causing the largest recorded pressure differential ( $\Delta P$ ) of 23 psi (158.6 kPa). The stabilized pressures used in the calculations of  $K_{ef}$  were  $P_{inlet}=0.97$  psi (6.7 kPa) and  $P_{outlet}=0.13$  psi (0.9 kPa). Using the Equation 3.8, the microannulus effective permeability of the first sample was found to be  $K_{ef1}=2.11$  D. The size of the microannulus was found to be  $w_1=1.96 \cdot 10^{-4}$  in. (5  $\mu$ m).

A second gas flow-through test was run immediately after pipe expansion at 2% expansion ratio. The multi-rate gas flow-through procedure post-expansion entailed a gradual increase in inlet pressure by 25 psi (172 kPa) every five minutes from 25 psi (172 kPa) to 100 psi (690 kPa). The outlet pressure transducer during this experiment did not show any detectable levels of pressure, suggesting that the 2% expansion ratio cone was

successful in sealing the microannular gas migration. The next gas flow-through test was run again 24 hours later following the same procedure of gradual pressure increase. There was no pressure recorded on the outlet port, confirming that the seal was still in place. The last gas flow-through test on the first sample was run 60 days after expansion with the same procedure and there was no pressure recorded on the outlet transducer. The flow-through test on the first sample, shown in Table 4.9, showed that the expansion cone with 2% expansion ratio was successful in permanently closing the microannular gas flow above the expanded region.

Table 4.9: Gas flow-through experiments data. The time lag represents the time elapsed between recordings of the two transducers. Stabilized inlet ( $P_{in}$ ) and outlet ( $P_{out}$ ) pressures used in the calculation of effective permeability of the microannulus ( $K_{ef}$ ). After expansion with the 2% expansion ratio cone, the microannular flow of 2.11 D permeability was successfully remediated. The size of the microannulus ( $w$ ) was found to have been 5 microns.

	$P_{in}$ [psi]	$P_{out}$ [psi]	Time lag [s]	$K_{ef}$ [D]	$w$ [ $\mu m$ ]
<b>Pre-expansion</b>	0.97	0.13	5	2.11	5
<b>0 hrs Post-expansion (2%)</b>	81	0	-	0	0
<b>24 hrs Post-expansion (2%)</b>	75.5	0	-	0	0
<b>60 days Post-expansion (2%)</b>	83	0	-	0	0

### 4.6.3 Gas Flow-through Test III – 2% Expansion

Multi-rate flow-through experiments conducted on the third sample showed microannular gas flow pre-expansion and pressures recorded on both pressure transducers. An identical inlet pressure of 15 psi (103 kPa) was selected, while the gas flow rate was kept at a constant value of 0.003 ft<sup>3</sup>/min (85 ml/min) upon pressure stabilization.

The recorded time lag between inlet and pressure transducer was over six seconds. After increasing the inlet pressure to 50 psi (345 kPa), the pressures recorded on the transducers increased to 45 psi (310 kPa) (inlet) and 17 psi (117 kPa) (outlet), giving a pressure differential ( $\Delta P$ ) of 28 psi (193 kPa). The stabilized pressures used in the calculations of microannulus effective permeability were  $P_{\text{inlet}}=0.92$  psi (6.3 kPa) and  $P_{\text{outlet}}=0.04$  psi (0.27 kPa). This sample was calculated to have the effective permeability of the microannulus of  $K_{\text{ef}2}=2.31$  D and the size of  $w_2=2.05 \cdot 10^{-4}$  in. (5.2  $\mu\text{m}$ ).

A second multi-rate gas flow-through test was run immediately after expansion with a gradual increase in inlet pressure by 25 psi (172 kPa) every five minutes from 25 psi (172 kPa) to 100 psi (690 kPa). There was no recording on the outlet pressure transducer during this experiment, which confirmed remediation of the microannular gas flow. Flow through experiments were also conducted 24 hours and 60 days after the expansion and both had zero readings at the outlet transducers. The 2% expansion proved to be successful in sealing the microannular gas migration. Detailed results are shown in Table 4.10.

Table 4.10: Gas flow-through experiments data. The time lag represents the time elapsed between recordings of the two transducers. Stabilized inlet ( $P_{in}$ ) and outlet ( $P_{out}$ ) pressures used in the calculation of effective permeability of the microannulus ( $K_{ef}$ ), the size ( $w$ ) of 5.2 microns. After expansion with the 2% expansion ratio cone, the microannular flow of 2.31 D permeability was successfully remediated.

	<b><math>P_{in}</math></b> <b>[psi]</b>	<b><math>P_{out}</math></b> <b>[psi]</b>	<b>Time lag</b> <b>[s]</b>	<b><math>K_{ef}</math></b> <b>[D]</b>	<b><math>w</math></b> <b>[<math>\mu m</math>]</b>
<b>Pre-expansion</b>	0.92	0.04	6	2.31	5.2
<b>0 hrs Post-expansion (2%)</b>	70	0	-	0	0
<b>24 hrs Post-expansion (2%)</b>	83	0	-	0	0
<b>60 days Post-expansion (2%)</b>	86	0	-	0	0

#### 4.6.4 Gas Flow-through Test IV – 4% Expansion

Flow-through experiments conducted on the fourth sample also showed microannular gas flow pre-expansion and pressures recorded on both pressure transducers. Inlet pressure was kept at 15 psi (103 kPa), and upon pressure stabilization the flow rate was kept at 0.003 ft<sup>3</sup>/min (85 ml/min). The time lag recorded between the two transducers was 13 seconds, indicating a lower permeability microannulus than in cases with the first two samples. Lower permeability was also indicated by a high  $\Delta P$  of 47 psi (324 kPa); the highest pressures recorded after increasing the inlet pressure to 50 psi (345 kPa) were 49 psi (338 kPa) (inlet) and 2 psi (14 kPa) (outlet). Calculations of the effective permeability of microannulus confirmed it had the lowest permeability of all the samples. The pressures used in the calculations were  $P_{inlet}=3.75$  psi (26 kPa) and  $P_{outlet}=0.36$  psi (2.5 kPa), and the effective permeability of microannulus was found to be  $K_{ef3}=0.14$  D. The size of the microannulus of this sample was calculated to be  $w_3=0.51 \cdot 10^{-4}$  in. (1.3  $\mu m$ ).

After pipe expansion with the cone of 4% expansion ratio, gas flow-through tests were run with the same procedure as for the previous samples, and no pressures were recorded on the outlet pressure transducer immediately after expansion, 24 hours later, and after 60 days. The only observed change was the maximum inlet pressure on the test run immediately after expansion, the test was run at 75 psi (517 kPa) due to leakage in the manifold tubing. An expansion ratio of 4% also proved to be successful in closing the microannular gas flow. Detailed results are shown in Table 4.11 below.

Table 4.11: Gas flow-through experiments data. The time lag represents the time elapsed between recordings of the two transducers. Stabilized inlet ( $P_{in}$ ) and outlet ( $P_{out}$ ) pressures used in the calculation of effective permeability of the microannulus ( $K_{ef}$ ). After expansion with the 4% expansion ratio cone, the microannular flow of 0.14 D permeability was successfully remediated. The size of the microannulus ( $w$ ) was found to have been 1.2 microns.

	$P_{in}$ [psi]	$P_{out}$ [psi]	Time lag [s]	$K_{ef}$ [D]	$w$ [ $\mu m$ ]
<b>Pre-expansion</b>	3.75	0.36	13	0.14	1.2
<b>0 hrs Post-expansion (4%)</b>	47	0	-	0	0
<b>24 hrs Post-expansion (4%)</b>	61	0	-	0	0
<b>60 days Post-expansion (4%)</b>	62	0	-	0	0

#### 4.6.5 Gas Flow-through Test V – 8% Expansion

The pre-expansion flow-through experiment on this sample also showed the existence of microannular gas flow with the pressure recorded on outlet pressure transducer. The same initial inlet pressure of 15 psi (103 kPa) was selected, and constant flow was kept at  $q = 0.003 \text{ ft}^3/\text{min}$  (85 ml/min) upon pressure stabilization. The recorded



time lag between inlet and outlet pressure transducers was just over one second indicating a microannulus with very high permeability. The inlet pressure was increased to 25 psi (172 kPa), and kept constant at that rate for four minutes and then increased to 50 psi (690 kPa). The highest recorded pressures on both transducers were approximately 26 psi (179 kPa) (inlet) and 16 psi (110 kPa) (outlet), resulting in the highest  $\Delta P$  of 10 psi (69 kPa).  $P_{\text{inlet}}=1.13$  psi (8 kPa) and  $P_{\text{outlet}}=1.00$  psi (7 kPa) were the stabilized pressures used in the calculations of  $K_{\text{eff}}$ . The microannulus effective permeability of the sample was found to be  $K_{\text{ef4}}=7.04$  D, while the size of the microannulus was  $w_4= 3.6 \cdot 10^{-4}$  in. (9.1  $\mu\text{m}$ ).

The highest expansion ratio of 8% was selected as the maximum expansion rate at our current load capacity. The second gas flow-through test was run immediately after expansion following the same procedure as the first sample: gradually increasing inlet pressure by 25 psi (172 kPa) every five minutes from an initial pressure of 25 psi (172 kPa) to a final pressure of 100 psi (690 kPa). After the test, the highest pressure value recorded on the outlet transducer was 0.214 psi (1.5 kPa) while inlet pressure was 68 psi (469 kPa) at that time. This pressure differential corresponded to the effective permeability of 300 nD. However, subsequent gas flow-through tests conducted 24 hours and 60 days post-expansion showed no pressure recordings on the outlet transducer. This test showed that an 8% expansion ratio was also successful in closing the microannular flow at tested pressure rates, as shown in Table 4.12.

Table 4.12: Gas flow-through experiments data. The time lag represents the time elapsed between recordings of the two transducers. Stabilized inlet ( $P_{in}$ ) and outlet ( $P_{out}$ ) pressures used in the calculation of effective permeability of the microannulus ( $K_{ef}$ ), with the size ( $w$ ) of 9.1 microns. After expansion with the 8% expansion ratio cone, the microannular flow of 7.04 D was decreased to 300 nD immediately after expansion. Gas flow-through tests 24 hours and 60 days after expansion showed complete seal of the microannular flow.

	$P_{in}$ [psi]	$P_{out}$ [psi]	Time lag [s]	$K_{ef}$ [D]	$w$ [ $\mu m$ ]
<b>Pre-expansion</b>	1.13	1.00	1	7.04	9.1
<b>0 hrs Post-expansion (8%)</b>	68	0.214	-	$3 \cdot 10^{-7}$	0.05
<b>24 hrs Post-expansion (8%)</b>	59	0	-	0	0
<b>60 days Post-expansion (8%)</b>	86	0	-	0	0

#### 4.6.6 Gas Flow-through Test VI – 8% Expansion

Pre-expansion gas flow-through tests on the sixth and final composite sample showed pressure recording on the outlet pressure transducer, confirming gas flow through the pre-manufactured microannulus. Initial conditions were kept the same as with previous samples, where initial inlet pressure was 15 psi (103 kPa) and the gas flow rate was kept at 0.003 ft<sup>3</sup>/min (85 ml/min) upon pressure stabilization. The time lag in pressure recording between the inlet and outlet pressure transducers was 7.5 seconds, while the highest pressures recorded after increasing the inlet pressure to 25 psi (172 kPa) were 17 psi (117 kPa) (inlet) and 3 psi (20.7 kPa) (outlet). Stabilized pressures used in  $K_{ef}$  calculations were  $P_{inlet}=1.72$  psi (12 kPa) and  $P_{outlet}=0.06$  psi (0.4 kPa), giving a microannulus effective permeability of  $K_{ef5}=0.66$  D. The size of the microannulus was found to have been  $w_5=1.1 \cdot 10^{-4}$  in. (2.8  $\mu m$ ).

The second gas flow-through test was run immediately after expansion at 8% expansion ratio, with the same procedure as the first five samples a gradual increase in inlet pressure by 25 psi (172 kPa) every five minutes from an initial pressure of 25 psi (172 kPa) to a final pressure of 100 psi (690 kPa), and it showed no pressure recording on the outlet pressure transducer.

The same procedure was repeated after 24 hours and then after 60 days. Both tests showed no pressure readings on the outlet pressure transducer, which confirmed that the 8% expansion ratio cone was successful in closing the microannular gas flow in the fifth composite sample. Detailed results are shown in Table 4.13 below.

Table 4.13: Gas flow-through experiments data. The time lag represents the time elapsed between recordings of the two transducers. Stabilized inlet ( $P_{in}$ ) and outlet ( $P_{out}$ ) pressures used in the calculation of effective permeability of the microannulus ( $K_{ef}$ ), which had the size ( $w$ ) of 2.8 microns. After expansion with the 8% expansion ratio cone, the microannular flow of 0.66 D permeability was successfully remediated.

	<b><math>P_{in}</math></b> <b>[psi]</b>	<b><math>P_{out}</math></b> <b>[psi]</b>	<b>Time lag</b> <b>[s]</b>	<b><math>K_{ef}</math></b> <b>[D]</b>	<b><math>w</math></b> <b>[<math>\mu</math>m]</b>
<b>Pre-expansion</b>	1.72	0.06	7.5	0.66	2.8
<b>0 hrs Post-expansion (8%)</b>	85.6	0	-	0	0
<b>24 hrs Post-expansion (8%)</b>	78	0	-	0	0
<b>60 days Post-expansion (8%)</b>	85	0	-	0	0

## CHAPTER 5: DISCUSSION

The main part of the experimental setup, the custom-made expansion system, was assembled, calibrated, and successfully applied in the operations of the inner pipe expansion. During the expansion of the inner pipe, the annular cement sheath was compressed and a change from a solid, hydrated structure into a material of softer consistency was observed. These structural changes resulted from the impact of the forces and pressures created by the movement of the expansion cone. The pipe expansion, which led to collapse of macro-pores within the cement matrix, most likely resulted in movement of free pore water ahead of the expansion cone during the expansion process. The results from experiments conducted with pigmented cement, shown in Figure 5.1, were used to test and confirm this hypothesis. The top quarter of the composite sample was cemented with red pigmented cement and the remainder of the sample consisted of unpigmented slurry with the same density of 13.1 lb/gal (1.57 g/cm<sup>3</sup>).

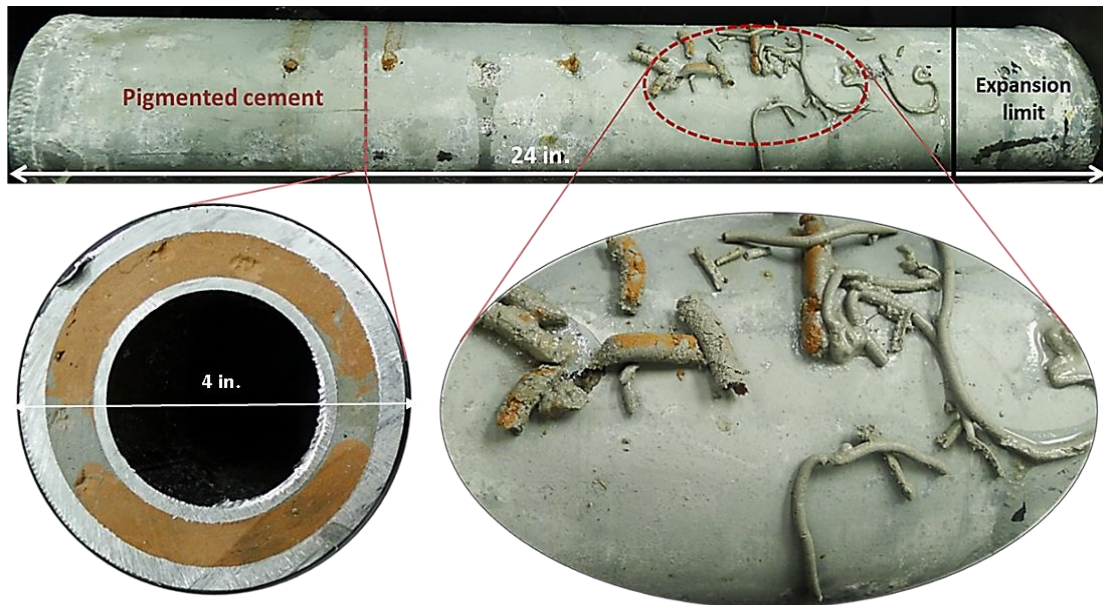


Figure 5.1: Expansion experiment with pigmented cement. The left image is a magnified view of the cross-section at the interface between pigmented and regular cement. The red cement pore water propagated through the sample ahead of the cone and was observed in the paste squeezed out through the holes on the outer pipe (right magnified view).

After expansion utilizing the 8% expansion ratio cone, cross-sections on multiple lengths throughout the sample revealed the propagation of the pore water. To further investigate the hypothesis of free pore water propagation and its role in successful expansion, a test was conducted on a composite sample which was dried in the oven. The sample was stored in the oven at 420°F (215°C) for 35 days after which an expansion was tried at a 4% expansion ratio. In this case, the cone stuck once it reached the cemented part of the pipe and was not able to perform expansion. This result further validated the hypothesis that free cement pore water propagation is the most likely driving force for successful expansion and mineralogical/microstructural changes in cement.

Water-extended cement slurry with a high w/c ratio of over 0.8 can have a total porosity of over 40% [6]. Most of the pores are within the range of 10-100 nm diameter; larger pores of up to 1  $\mu\text{m}$ , however, can be present in 10% of the total porosity in cement slurries with w/c ratios close to 0.9 [8].

The hypothesis that the first stage of cement compaction was primarily the collapsing of smaller pores and larger air bubbles was confirmed using optical microscopy on thin cement sections. The next stage of cement compaction was most likely the movement of pore water from the smallest pores (over 50 nm), compression and dissolution of unhydrated cement grains, and change in C-S-H structure and other mineral products of hydration. This mechanism is shown in Figure 5.2, where CT images of the cement from pre- and post-expansion samples are processed to fit the illustration. The brightest area of the image is the material with the highest density; in this case unhydrated cement grains of  $\text{C}_3\text{S}$ ,  $\text{C}_2\text{S}$  and  $\text{C}_4\text{AF}$ , whose large structures are observable in the control sample.

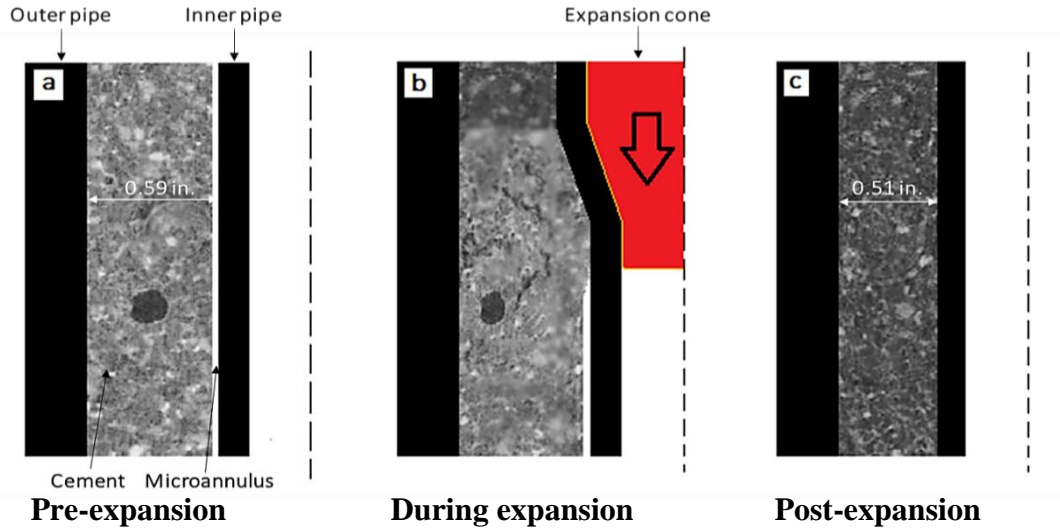


Figure 5.2: An illustration of the expansion process (not to scale). The cement sheath images were obtained with X-ray computer tomography (CT) and processed to fit the schematic. a. the pre-expansion illustration shows microannulus between the inner pipe and the cement sheath; b. during expansion the cone is being pulled (arrow showing direction) and the cement sheath is being compressed behind the pipe, altering its structure; c. after expansion at 8% expansion ratio, the compressed cement sheath is shown without the microannulus.

The darkest spots represent the pores, dispersed throughout the cement matrix in the control sample image, while slightly brighter areas indicate presence of portlandite crystals. The darker shaded image of the compressed cement sample indicated structural changes and increased concentration of hydrated material, such as C-S-H. Unhydrated clinker phases are much more dispersed and smaller in the cement matrix of this sample. The post-expansion image proved the assumption that dissolution of Ca-rich unhydrated clinker phases is occurring during expansion.

The volume of displaced cement was calculated with the assumption that every sample was expanded 11 in. (28 cm) into the cement sheath. The largest displaced volume (V) was obtained with the 8% expansion cone resulting in a 10%, or 6.37 in<sup>3</sup> (104.47 cm<sup>3</sup>), reduction in volume of the initial cement sheath (Table 5.1). Taking into consideration the porosity percentages discussed, it is assumed that the remaining volume of displaced

cement consisted of unhydrated cement grains and hydrated cement minerals which underwent compaction and restructuralization.

Table 5.1: A summary of the volume calculations of compressed cement. The cement sheath was expanded to a length of 11 in. (28 cm) and the largest volume of cement displaced by the pipe (V) occurred during the 8% expansion (10% of the initial volume of the cement).

<b>Expansion ratio [%]</b>	<b>V [in<sup>3</sup>], (cm<sup>3</sup>)</b>	<b>V [%]</b>
Volume of cement sheath to be expanded – control sample	60.15 (985.62)	100
Volume of displaced cement after expansion at 2% expansion ratio	1.23 (20.09)	-2.04
Volume of displaced cement after expansion at 4% expansion ratio	2.91 (47.75)	-4.85
Volume of displaced cement after expansion at 8% expansion ratio	6.37 (104.47)	-10.60

Effluent samples were collected through the holes on the pipe for ICP mass spectrometry and the results showed high concentrations of Na<sup>+</sup> and K<sup>+</sup>. Aktas et al. (1999) also observed that the concentration of Na<sup>+</sup> and K<sup>+</sup> ions was the highest in the squeezed pore solution, which agrees with the atomic absorption results of the effluent samples collected after compression of the hydrated cement paste [73]. There are two possible explanations for the concentration of Ca<sup>2+</sup>, Fe<sup>3+</sup>, Mg<sup>2+</sup> and S<sup>6+</sup> increasing by more than three times in the effluent sample expanded 8%, compared to the one expanded at a 4% expansion ratio. These ions can be assigned to the dissolution of unhydrated cement grains such as alite, ferrite, and SO<sub>3</sub> and MgO phases present in the clinker. Another hypothesis is that the ions are coming from dissolving hydrated minerals of portlandite, ettringite, magnesium hydroxide and hydrated calcium aluminate phases. Dissolution of ettringite

and hydrated aluminates, however, would have also shown a larger increase in  $\text{Al}^{3+}$  concentration than the measured 20% (compared between the 8% expansion and the 4% expansion ratios) indicating greater probability of the first hypothesis.

Another important observation was made five days post-expansion. The cement sheath regained its solid structure and strength after a period of rehydration in the water bath. A similar process was observed by Ramachandran and Beaudoin (2001). The pipe expansion seemed to have triggered re-compaction of hydrated set cement, a process similar to that during the normal hydration process [5].

The mechanical properties of the post-expanded cement sheath were examined by microindentation on samples six days and six months post-expansion. The indentation of samples six days after expansion confirmed what was observed visually after expansion; namely that the integrity and strength of the cement ongoing through rehydration was weaker than the control sample. Indentation experiments six months post-expansion showed an overall increase in hardness and Young's Modulus of cement. This can be correlated with an increase in strength of the rehydrated cement [74], which is important information for field application and long-term wellbore integrity. Cement regained its mechanical properties and became stronger than the control sample after six month of rehydration.

The effect of the expansion process on the mechanical properties of the pipes was also quantified. Due to the internal loading from the expansion force, there is only a slight reduction in the pipe's burst pressure rating; less than 10% for the highest expansion ratio of 8%. The burst capabilities of the casing, however, will not be as detrimental as calculated due to isotropic strain hardening in the direction of the load. The collapse pressure rating



decreased significantly because of expansion's effect on loading in the opposite direction, in this case collapse (outer) pressure. Calculations for the highest expansion ratio of 8% showed a decrease in collapse rating of over 20%. This detrimental effect has to be taken into account when running expansion of casing in the wellbore for remediation purposes. These calculations do not consider the effect of the pressure build-up in the cement sheath ahead of the cone, which will have an additional impact on casing collapse and presents a great risk. The casing ratings should be known and strong enough to withstand the decrease of the collapse pressure rating post-expansion.

The main goal of this thesis research was to test the capabilities of pipe expansion in sealing the microannular gas flow. A wide range of permeabilities (0.14 D to 7.04 D) and microannuli sizes (from 1.2 to 9.1  $\mu\text{m}$ ) were calculated pre-expansion. The multi-rate gas flow-through tests showed that all expansion ratios of 2%, 4% and 8% were effective in closing the microannular gas flow through samples with a pre-manufactured microannulus. The tests confirmed that the seal was durable and still in place even after two months.

Small holes on the outer pipe provided pressure/fluid release from the cement sheath during expansion. This would simulate a casing expansion in the openhole section of the wellbore. The holes simulate either the porosity, in the case of sandstone, or the volumetric expansion of the formation, in the case of shale.

All of the findings presented here provide insight into the theory behind the mechanisms occurring within cement and the cement/pipe interface during pipe expansion. The restructuralization and rehydration of the cement matrix, triggered by the compression of the cement sheath, did not hinder cement integrity at the higher expansion ratio of 8%.

This is an important conclusion for field application where this technology would be applied to seal microannular gas flow behind the casing.

The channels and fractures in the cement matrix and microannuli at the interfaces can be located using proven conventional logging techniques, such as spinners, temperature logs, and downhole cameras, which are widely used in the detection of leaks in offshore wells [67]. If the leak is small, these devices are limited in their effectiveness, but ultrasonic logging tools have been successfully utilized for leak detection. After locating the problematic zone, a low expansion ratio collapsible (retrievable) cone should be run downhole to expand the casing between the couplings by a certain percentage and compress the cement sheath. The expanded region should provide a durable seal without compromising the wellbore cement integrity at higher expansion ratio of over 8%, while the humidity, high pressures, and temperatures at subsurface conditions would quicken the rehydration period.

## CHAPTER 6: CONCLUSIONS AND RECOMMENDATIONS

### 6.1 Conclusions

The potential of expandable casing technology was investigated as a remediation tool for microannular gas flow between the casing and cement in the open hole section of the wellbore. The first objective was to develop a bench-scale physical model for the simulation of expandable tubulars. The main objective was to successfully apply this model to test the potential of expandable casing technology for remediation of microannular gas migration.

During expansion experiments conducted in this investigation multiple observations and measurements were made. These have been documented in Chapters 4 and 5, and the Appendices. Multi-rate gas flow-through experiments were run post-expansion to test the seal of the microannular flow immediately, 24 hours, and 60 days after expansion. The following conclusions were made after this experimental investigation:

- Free cement pore water propagation is crucial for successful pipe expansion. The wellbore cement will always have sufficient humidity from the formation fluids. Furthermore, higher temperature and pressure conditions make the environment ideal for successful expansion experiments and faster rehydration.
- The integrity of the wellbore cement will not be hindered pipe expansion after certain rehydration period of the compressed cement matrix.
- The casing collapse rating must be known in order to determine whether it can withstand expansion with the cement sheath behind the pipe.

- Pipe expansion has been shown to have great potential in sealing microannular gas flow behind the casing. The seal was permanent even 60 days after expansion remediation.
- Implementation of this method in the field has the potential to mitigate leaky wells in CO<sub>2</sub> sequestration projects, wellbores completed for hydraulic-fracturing, and other conventional oil and gas wells.

## 6.2 Recommendations

Future work could entail a closer look into C-S-H structures on a nanoscale. Hydration of pure C<sub>3</sub>S in controlled environment and nanoindentation under confinement might explain even more the mechanisms behind microstructural changes due to pipe expansion. While this work focused on effects on a microscale, Transmission Electron Microscopy (TEM) could provide deeper view of such changes on a nanoscale.

Recommendations for future experiments would also include running expansion on cements with lower w/c ratios, as well as including various additives into the mixture to simulate the field application as closely as possible. Expansion on corroded and older cement samples could be run (over one year of hydration) to investigate the effect of older cements and low pH environment on applicability of casing expansion.

Multi-rate flow-through experiments are suggested with different gases (e.g. CH<sub>4</sub>), with higher inlet pressure cycles for longer periods of time, e.g. a 100 psi (689.5 kPa) increase every 10 minutes from 100 to 500 psi (0.69 to 3.45MPa). The poor bond on pipe/cement interface could be simulated by mud contamination and/or flowing gas during cement hydration to create gas channels.

## REFERENCES

1. Dusseault, M., M. Gray, and P. Nawrocki. *Why oilwells leak: cement behavior and long-term consequences*. in *International Oil and Gas Conference and Exhibition in China*. 2000.
2. Kaiser, M. and B. Kruse, *A Risk-Adjusted Method for Determining OCS Lease Abandonment Liability in the Gulf of Mexico for BOEMRE Supplemental Bonding*. SPE Economics & Management, 2011. **3**(1): p. 22-30.
3. Nelson, E.B. and D. Guillot, *Well Cementing Schlumberger*. Sugar Land, TX, USA, 2006.
4. C150, A. *Standard Specification for Portland Cement, Annual Book of ASTM Standards*. 2001. ASTM Philadelphia, PA.
5. Ramachandran, V.S. and J.J. Beaudoin, *Handbook of analytical techniques in concrete science and technology: principles, techniques and applications*. 2000: Access Online via Elsevier.
6. Taylor, H.F., *Cement chemistry*. 1997: Thomas Telford.
7. Velez, K., et al., *Determination by nanoindentation of elastic modulus and hardness of pure constituents of Portland cement clinker*. Cement and Concrete Research, 2001. **31**(4): p. 555-561.
8. Mehta, P.K. and P.J. Monteiro, *Concrete: microstructure, properties, and materials*. 2006.
9. Cook, R.A. and K.C. Hover, *Mercury porosimetry of hardened cement pastes*. Cement and Concrete Research, 1999. **29**(6): p. 933-943.
10. Tsvivilis, S., et al., *The permeability of Portland limestone cement concrete*. Cement and Concrete Research, 2003. **33**(9): p. 1465-1471.
11. Glinicki, M.A. and M. Zielinski, *Depth-sensing indentation method for evaluation of efficiency of secondary cementitious materials*. Cement and concrete research, 2004. **34**(4): p. 721-724.
12. Mahmoudkhani, A., L. Bava, and B. Wilson, *An Innovative Approach for Laboratory Evaluation of Defoamers for Oilfield Cementing Applications*. Brasil Offshore, 2011.
13. API, R., *10B: Recommended Practice for Testing Oilwell Cements and Cement Additives*. Appendix C (tentative), "Fluid Density Balance," American Petroleum Institute Publication 'a, 1971.
14. Benge, O. and W. Webster. *Evaluation of blast furnace slag slurries for oilfield application*. in *SPE/IADC Drilling Conference*. 1994.
15. Maier, L., et al., *Cementing Materials for Cold Environments*. Journal of Petroleum Technology, 1971. **23**(10): p. 1215-1220.

16. Frigione, G. and S. Marra, *Relationship between particle size distribution and compressive strength in Portland cement*. Cement and concrete research, 1976. **6**(1): p. 113-127.
17. Garnier, A., et al. *Characterization of cement systems to ensure cement sheath integrity*. in *Offshore Technology Conference*. 2007.
18. Jo, H. and K. Gray. *Mechanical Behavior of Concentric Casing, Cement, And Formation Using Analytical And Numerical Methods*. in *44th US Rock Mechanics Symposium and 5th US-Canada Rock Mechanics Symposium*. 2010.
19. Goodwin, K. and R. Crook, *Cement sheath stress failure*. SPE drilling engineering, 1992. **7**(4): p. 291-296.
20. Heathman, J. and F. Beck. *Finite Element Analysis Couples Casing and Cement Designs for HTHP Wells in East Texas*. in *IADC/SPE Drilling Conference*. 2006.
21. Celia, M.A., et al. *Quantitative estimation of CO<sub>2</sub> leakage from geological storage: Analytical models, numerical models and data needs*. in *Proceedings of 7th International Conference on Greenhouse Gas Control Technologies.(GHGT-7)*. 2004.
22. Boukhelifa, L., et al. *Evaluation of cement systems for oil and gas well zonal isolation in a full-scale annular geometry*. in *IADC/SPE Drilling Conference*. 2004.
23. Brandl, A., et al., *Cementing solutions for corrosive well environments*. SPE Drilling & Completion, 2011. **26**(2): p. 208-219.
24. Bachu, S. and D.B. Bennion, *Experimental assessment of brine and/or CO<sub>2</sub> leakage through well cements at reservoir conditions*. International Journal of Greenhouse Gas Control, 2009. **3**(4): p. 494-501.
25. Huerta, N., D. Checkai, and S. Bryant. *Utilizing sustained casing pressure analog to provide parameters to study CO<sub>2</sub> leakage rates along a wellbore*. in *SPE International Conference on CO<sub>2</sub> Capture, Storage, and Utilization*. 2009.
26. Howarth, R.W., R. Santoro, and A. Ingraffea, *Methane and the greenhouse-gas footprint of natural gas from shale formations*. Climatic Change, 2011. **106**(4): p. 679-690.
27. Calosa, W.J., B. Sadarta, and R. Ronaldi. *Well Integrity Issues in Malacca Strait Contract Area*. in *SPE Oil and Gas India Conference and Exhibition*. 2010.
28. King, G.E., King, D.E., *Environmental Risk Arising From Well Construction Failure: Difference between Barrier and Well Failure, and Estimates of Failure Frequency*, in *SPE Annual Technical Conference and Exhibition*. 2013: New Orleans, LA.
29. Nicot, J.-P., *A survey of oil and gas wells in the Texas Gulf Coast, USA, and implications for geological sequestration of CO<sub>2</sub>*. Environmental geology, 2009. **57**(7): p. 1625-1638.
30. Watson, T. and S. Bachu, *Evaluation of the potential for gas and CO<sub>2</sub> leakage along wellbores*. SPE Drilling & Completion, 2009. **24**(1): p. 115-126.

31. Nygaard, R. and R. Lavoie. *Well Integrity and Workover Candidates for Existing Wells in the Wabamun Area CO2 Sequestration Project (WASP)*. in *Canadian Unconventional Resources and International Petroleum Conference*. 2010.
32. Xu, R., *Analysis of Diagnostic Testing of Sustained Casing Pressure in Wells*, in *Petroleum Engineering*. 2002, Louisiana State University: Baton Rouge, Louisiana.
33. Nelson, E.B., *Well cementing*. 1990: Elsevier Science.
34. Report, J.I.P., *Best Practices for Prevention and Management of Sustained Casing Pressure*. 2001: 13800 Westfair East Drive, Houston, Texas 77041-1101.
35. Xu, R. and A. Wojtanowicz. *Diagnostic Testing of Wells With Sustained Casing Pressure-An Analytical Approach*. in *Canadian International Petroleum Conference*. 2003.
36. IEA GHG, B.a.P.U., *Summary Report of 2nd Wellbore Integrity Network Meeting*. 2006.
37. Duan, S. and A. Wojtanowicz. *A Method for Evaluation of Risk of Continuous Air Emissions From Sustained Casinghead Pressure*. in *SPE/EPA/DOE Exploration and Production Environmental Conference*. 2005.
38. Kinik, K. and A. Wojtanowicz. *Identifying environmental risk of sustained casing pressure*. in *SPE Americas E&P Health, Safety, Security, and Environmental Conference*. 2011.
39. Bourgoyne, A., S. Scott, and J. Regg. *Sustained casing pressure in offshore producing wells*. in *Offshore Technology Conference*. 1999.
40. *Code of Federal Regulations, title 30 § 250.525.a*. . 2013.
41. Orszulik, S.T., *Environmental technology in the oil industry*. 2008: Springer.
42. Wojtanowicz, A.K., S. Nishikawa, and X. Rong, *Diagnosis and remediation of sustained casing pressure in wells*. final report, United States Minerals Management Service (July 2001), 2001.
43. Wojtanowicz, A., et al. *Cement Pulsation Treatment in Wells*. in *SPE Annual Technical Conference and Exhibition*. 2002.
44. Goodwin, K. *Principles of Squeeze Cementing*. in *Permian Basin Oil and Gas Recovery Conference*. 1984.
45. Soter, K., *Removal of Sustained Casing Pressure Utilizing a Workover Rig*. 2003, Faculty of the Louisiana State University and Agricultural and Mechanical College in partial fulfillment of the requirements for the degree of Master of Science in Petroleum Engineering in The Department of Petroleum Engineering by Kevin Soter BS, University of Tulsa.
46. Rauchenstein, W. and C. Blount. *Cementing a Long Horizontal Wellbore Using CT-Squeeze Technology*. in *SPE/ICoTA Coiled Tubing Conference and Exhibition*. 2005.
47. CAMPO, D., et al., *Monodiameter drilling liner: From concept to reality*. *Journal of petroleum technology*, 2004. **56**(2): p. 37-38.

48. Chakrabarty, J., *Theory of plasticity*. 2006: Butterworth-Heinemann.
49. Lubliner, J., *Plasticity theory*. 2008: Courier Dover Publications.
50. Asahi, H., et al., *Effect of Metallurgical Factors on Expandability and Mechanical Properties after Expansion for Expandable Tubulars*. CORROSION 2005, 2005.
51. Beer, F.P. and E.R. Johnston, *Statics and mechanics of materials*. 1992: McGraw-Hill Companies.
52. Jabs, M. and B.O. Tools, *Using expandable metal technology to create a monobore well*. OTC, 2004. **16670**: p. 3-6.
53. Mack, R. *The Effect of Tubular Expansion on the Mechanical Properties and Performance of Selected OCTG-Results of Laboratory Studies*. in *Paper OTC 17622, presented at the Offshore Technology Conference*. 2005. Houston, Texas.
54. Pervez, T., *Experimental and numerical investigation of expandable tubular structural integrity for well applications*. Journal of Achievements in Materials and Manufacturing Engineering, 2010. **41**(1-2): p. 147-154.
55. Miessner, D., et al. *Solid Expandable Tubular Technology: Case histories of value adding & enabling applications in Sabah Deepwater*. in *IADC/SPE Asia Pacific Drilling Technology Conference and Exhibition*. 2006.
56. Gupta, Y. and S. Banerjee. *The application of expandable tubulars in casing while drilling*. in *Production and Operations Symposium*. 2007.
57. Grant, T. and M. Bullock. *The evolution of Solid Expandable Tubular Technology: Lessons Learned Over Five Years*. in *Offshore Technology Conference*. 2005.
58. Jennings, I. *Dynamic formations rendered less problematic with solid expandable technology*. in *IADC/SPE Asia Pacific Drilling Technology Conference and Exhibition*. 2008.
59. Fanguy, C., D. Mueller, and D. Doherty. *Improved method of cementing solid expandable tubulars*. in *SPE Annual Technical Conference and Exhibition*. 2004.
60. Heathman, J., et al. *Enhanced Cementing Practices Address Unique Issues Found with Solid Expandable Tubular Applications*. in *SPE/IADC Drilling Conference*. 2007.
61. Badrack, R.P., D.J. Hillis, and W.P. Howie, *Solid Expandable Technology? Testing and Application*. CORROSION 2005, 2005.
62. Dupal, K., et al. *Solid Expandable Tubular Technology-A Year of Case Histories in the Drilling Environment*. in *SPE/IADC drilling conference*. 2001.
63. Carstens, C. and K. Blasingame. *Solid Expandable Tubular Technology: The Value of Planned Installation vs. Contingency*. in *SPE/IADC Drilling Conference*. 2005.
64. Bargawi, R., et al. *Expandable Tubular Successfully Scab off Severe Casing Leaks*. in *SPE/IADC Middle East Drilling Technology Conference and Exhibition*. 2005.



65. DeLange, R., R. Gandikota, and S. Osburn, *A Major Advancement in Expandable Connection Performance, Enabling Reliable Gastight Expandable Connections*. SPE Drilling & Completion, 2011. **26**(3): p. 412-418.
66. Bourgoyne Jr, A.T., et al., *Applied drilling engineering*. . Vol. 2. 1986, Richardson, Texas: Society of Petroleum Engineers.
67. Oliver, W.C. and G.M. Pharr, *Measurement of hardness and elastic modulus by instrumented indentation: Advances in understanding and refinements to methodology*. Journal of materials research, 2004. **19**(01): p. 3-20.
68. Celestin, A., *Nanovea - Analytical Report*. 2013, Nanovea Inc. p. 10.
69. Kahraman, S., M. Fener, and E. Kozman, *Predicting the compressive and tensile strength of rocks from indentation hardness index*. Journal of the Southern African Institute of Mining and Metallurgy, 2012. **112**(5): p. 331-339.
70. García, R.-A., et al., *Development of experimental correlations between indentation parameters and unconfined compressive strength (UCS) values in shale samples*. CT & F Ciencia, Tecnología, Futuro, 2008. **3**(4): p. 61-81.
71. Szwedzicki, T. *Draft ISRM suggested method for determining the indentation hardness index of rock materials*. in *International Journal of Rock Mechanics and Mining Sciences and Geomechanics Abstracts*. 1998. Elsevier Science.
72. Earnest, C.M., *Compositional analysis by thermogravimetry*. Vol. 997. 1988: Astm International.
73. Aktas, M., C. Laskowski, and G. Volland, *Determination of portlandite and other cement compounds in hardened cement paste after squeezing pore solution with high pressure*. Otto Graf Journal(Germany), 1999. **10**: p. 38-49.
74. Thiercelin, M., et al. *Cement design based on cement mechanical response*. in *SPE Annual Technical Conference and Exhibition*. 1997.
75. Al-Abri, O.S. and T. Pervez, *Structural behavior of solid expandable tubular undergoes radial expansion process—Analytical, numerical, and experimental approaches*. International Journal of Solids and Structures, 2013. **50**(19): p. 2980-2994.
76. Engler, T., *Fluid Flow in Porous Media*. 2010, New Mexico Tech.

**APPENDIX A**  
**DETAILED INDENTATION RESULTS**

Table A.1: Detailed indentation results of the control sample. The hardness was highest on the third indent (middle of the cement sheath), while the lowest value was located on the outer pipe side of the cement sheath.

<b>Indentation</b>	<b>Hardness [Vickers]</b>	<b>Hardness [MPa]</b>	<b>Young's Modulus [MPa]</b>	<b>Max Depth [μm]</b>
1	3.284	34.75	4070	157.1
2	2.292	24.26	3767	186.8
3	4.435	46.93	4768	135.7
4	3.122	33.04	4110	160.8
5	2.074	21.95	3151	196.7
<b>Average</b>	<b>3.04</b>	<b>32.2</b>	<b>3973</b>	<b>167.4</b>
<b>Standard Deviation</b>	<b>0.94</b>	<b>9.90</b>	<b>587</b>	<b>244.5</b>

Table A.2: Detailed indentation results of the sample expanded with the 2% expansion ratio cone. The hardness was highest on the first indent (closest to the inner pipe side of the cement sheath), while the lowest value obtained was in the middle of the cement sheath.

<b>Indentation</b>	<b>Hardness [Vickers]</b>	<b>Hardness [MPa]</b>	<b>Young's Modulus [MPa]</b>	<b>Max Depth [μm]</b>
1	3.15	33.4	3138	161
2	2.98	31.6	1530	171
3	2.27	24.0	5596	187
4	2.63	27.9	3472	175
5	2.45	25.9	1445	187
<b>Average</b>	<b>2.70</b>	<b>28.5</b>	<b>3036</b>	<b>176</b>
<b>Standard Deviation</b>	<b>0.37</b>	<b>3.9</b>	<b>1700</b>	<b>11</b>

Table A.3: Detailed indentation results of the sample expanded with the 4% expansion ratio cone. The hardness was highest on the first indent (closest to the inner pipe side of the cement sheath), while the lowest value obtained was on the second indent.

<b>Indentation</b>	<b>Hardness [Vickers]</b>	<b>Hardness [MPa]</b>	<b>Young's Modulus [MPa]</b>	<b>Max Depth [<math>\mu\text{m}</math>]</b>
1	2.26	23.9	2332	190
2	1.48	15.6	2354	233
3	1.85	19.6	2311	209
4	2.23	23.6	1154	197
5	1.98	20.9	1653	205
<b>Average</b>	<b>1.96</b>	<b>20.7</b>	<b>1961</b>	<b>207</b>
<b>Standard Deviation</b>	<b>0.32</b>	<b>3.4</b>	<b>539</b>	<b>16</b>

Table A.4: Detailed indentation results of the sample expanded with the 8% expansion ratio cone. Hardness was highest on the fifth indent (closest to the outer pipe side of the cement sheath), while the lowest value was obtained in the middle of the cement sheath.

<b>Indentation</b>	<b>Hardness [Vickers]</b>	<b>Hardness [MPa]</b>	<b>Young's Modulus [MPa]</b>	<b>Max Depth [<math>\mu\text{m}</math>]</b>
1	1.67	17.7	750	162
2	2.26	23.9	1448	137
3	1.09	11.6	1030	274
4	1.50	15.9	1400	166
5	3.07	32.5	1353	120
<b>Average</b>	<b>1.92</b>	<b>20.3</b>	<b>1196</b>	<b>172</b>
<b>Standard Deviation</b>	<b>0.77</b>	<b>8.1</b>	<b>298</b>	<b>60</b>

Table A.5: Detailed indentation results of the sample six months post-expansion at 2% expansion ratio. The hardness was highest on the fifth indent (closest to the outer pipe side), while the lowest value obtained was in the middle of the cement sheath.

<b>Indentation</b>	<b>Hardness [Vickers]</b>	<b>Hardness [MPa]</b>	<b>Young's Modulus [MPa]</b>	<b>Max Depth [<math>\mu\text{m}</math>]</b>
1	3.35	35.4	5286	155
2	3.12	33.0	3850	161
3	2.93	31.0	5595	165
4	3.33	35.3	4268	156
5	3.36	35.6	6170	54
<b>Average</b>	<b>3.22</b>	<b>34.1</b>	<b>5034</b>	<b>158</b>
<b>Standard Deviation</b>	<b>0.19</b>	<b>2.0</b>	<b>956</b>	<b>5</b>

Table A.6: Detailed indentation results of the sample six months post-expansion at 4% expansion ratio. The hardness was highest on the third indent (middle of the cement sheath), while the lowest value obtained was on the outer pipe side of the cement sheath.

<b>Indentation</b>	<b>Hardness [Vickers]</b>	<b>Hardness [MPa]</b>	<b>Young's Modulus [MPa]</b>	<b>Max Depth [<math>\mu\text{m}</math>]</b>
1	3.32	35.2	3075	157
2	3.08	32.6	1779	167
3	3.53	37.4	1872	156
4	3.13	33.1	4163	161
5	2.75	29.1	3218	172
<b>Average</b>	<b>3.16</b>	<b>33.5</b>	<b>2823</b>	<b>163</b>
<b>Standard Deviation</b>	<b>0.29</b>	<b>3.1</b>	<b>1003</b>	<b>7</b>

Table A.7: Detailed indentation results of the sample six months post-expansion at 8% expansion ratio. Hardness was highest on the fourth indent (middle of the cement sheath), while the lowest value was obtained on point closest to inner pipe side of the cement sheath.

<b>Indentation</b>	<b>Hardness [Vickers]</b>	<b>Hardness [MPa]</b>	<b>Young's Modulus [MPa]</b>	<b>Max Depth [<math>\mu\text{m}</math>]</b>
1	3.19	33.8	3325	160
2	3.50	37.1	6369	151
3	3.33	35.2	3820	156
4	3.80	40.2	3335	148
5	3.73	39.5	6434	146
<b>Average</b>	<b>3.51</b>	<b>37.2</b>	<b>4656</b>	<b>152</b>
<b>Standard Deviation</b>	<b>0.26</b>	<b>2.7</b>	<b>1606</b>	<b>6</b>

**APPENDIX B**  
**MULTI-RATE GAS FLOW-THROUGH DATA**

**B.1 Gas Flow-through Test II – 2% Expansion**

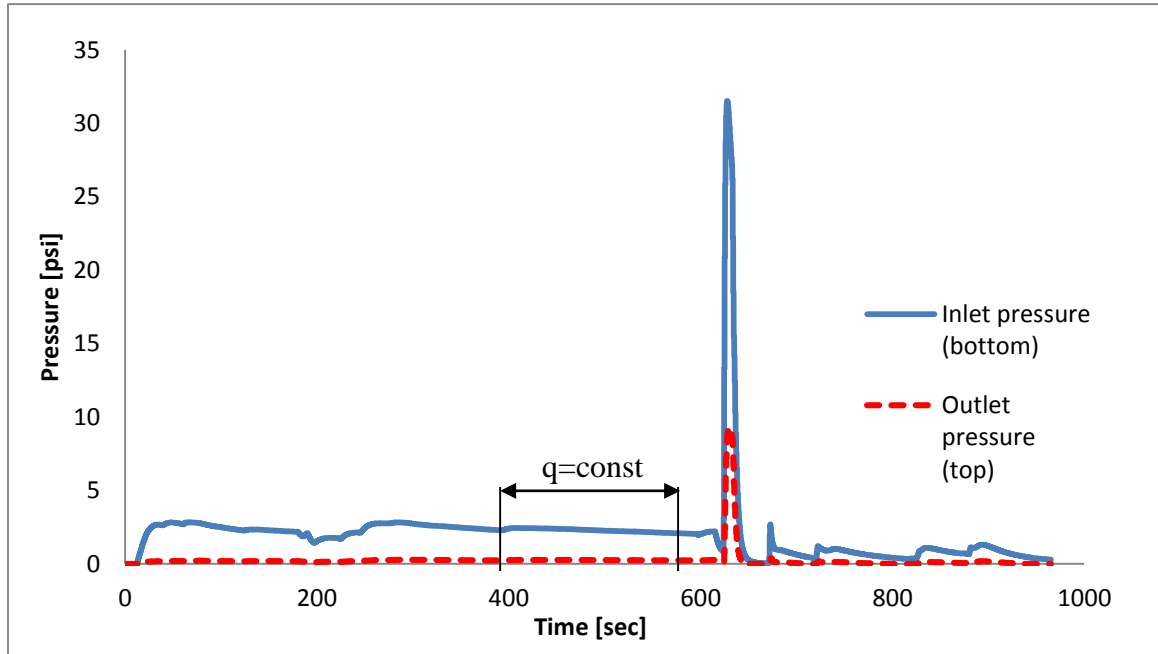


Figure B.1: Gas flow-through test data plot pre-expansion showing registered pressures on the inlet and outlet pressure transducers. The starting inlet pressure on the gas cylinder was 15 psi (103 kPa), and the flow was kept constant in the period from 7-10 minutes of the flow-through test. The inlet pressure was increased to 50 psi (345 kPa), which resulted in a spike of both pressures on the inlet and outlet ports, confirming the microannular gas flow through the composite sample.

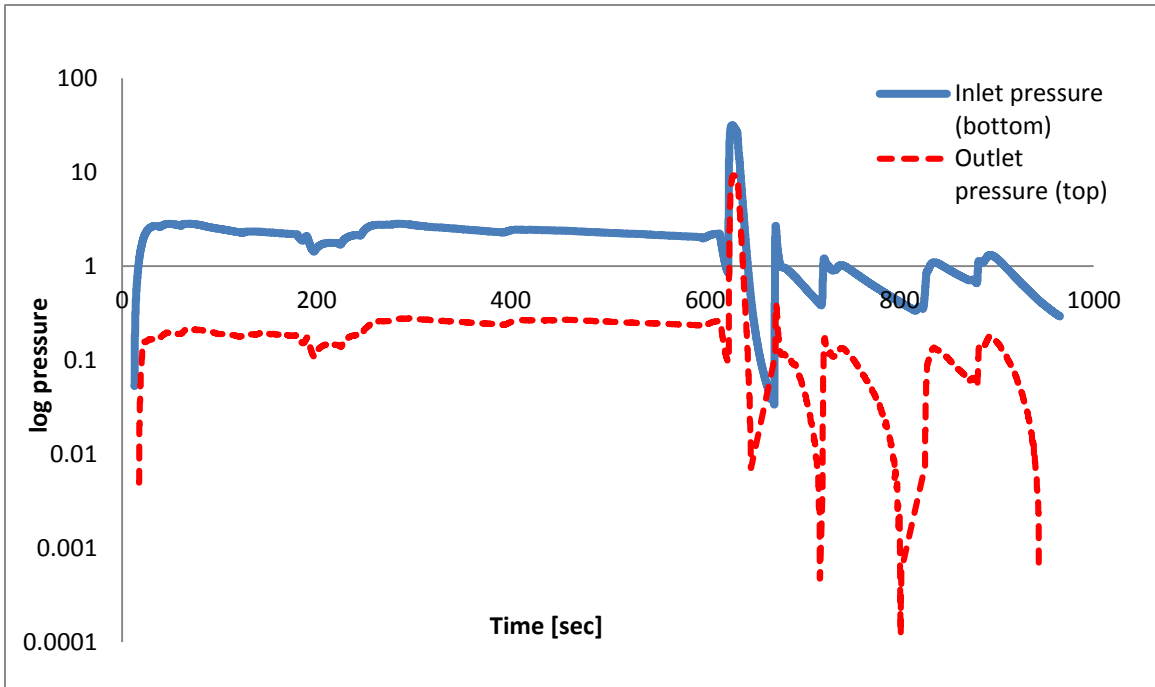


Figure B.3: Gas flow-through test data pre-expansion semi-log plot showing the pressure differential ( $\Delta P$ ) between pressures recorded on the inlet and outlet pressure transducers. The pressure differential in the first case was shown to have a relatively larger value, which after calculations indicated a microannulus with an effective permeability of 2.11 D.

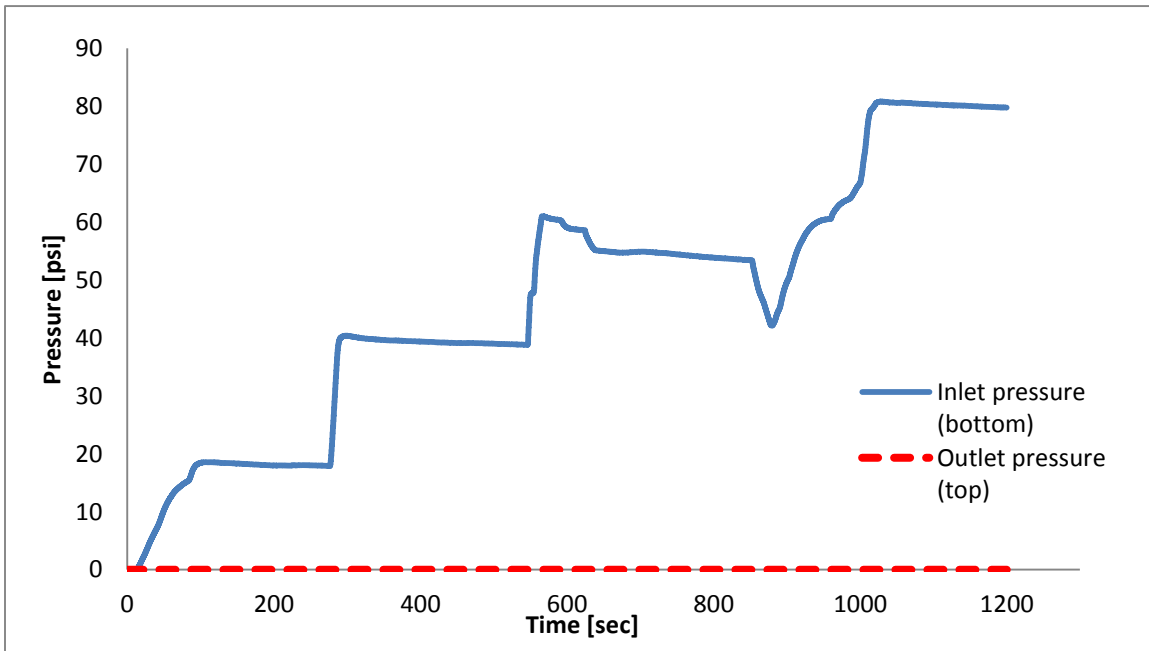


Figure B.2: Multi-rate gas flow-through test data plot recorded immediately after expansion with the 2% expansion ratio cone. After a gradual increase of 25 psi (172 kPa) in inlet pressure on the gas cylinder every five minutes from 25 psi (172 kPa) to 100 psi (690 kPa), there was no recorded pressure on the outlet pressure transducer, indicating successful remediation of the microannular gas flow.

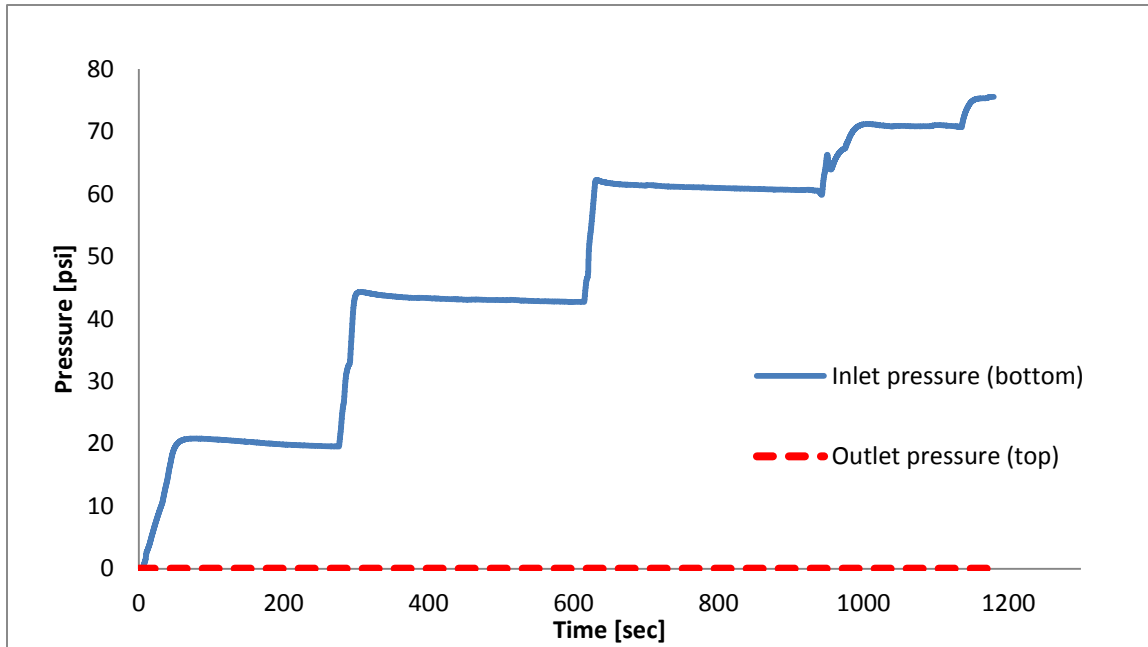


Figure B.4: Multi-rate gas flow-through test data plot recorded 24 hours after expansion with the 2% expansion ratio cone. After a gradual increase of 25 psi (172 kPa) in inlet pressure on the gas cylinder every five minutes from 25 psi (172 kPa) to 100 psi (690 kPa), there was no recorded pressure on the outlet transducer, confirming that the microannular seal was still effective.

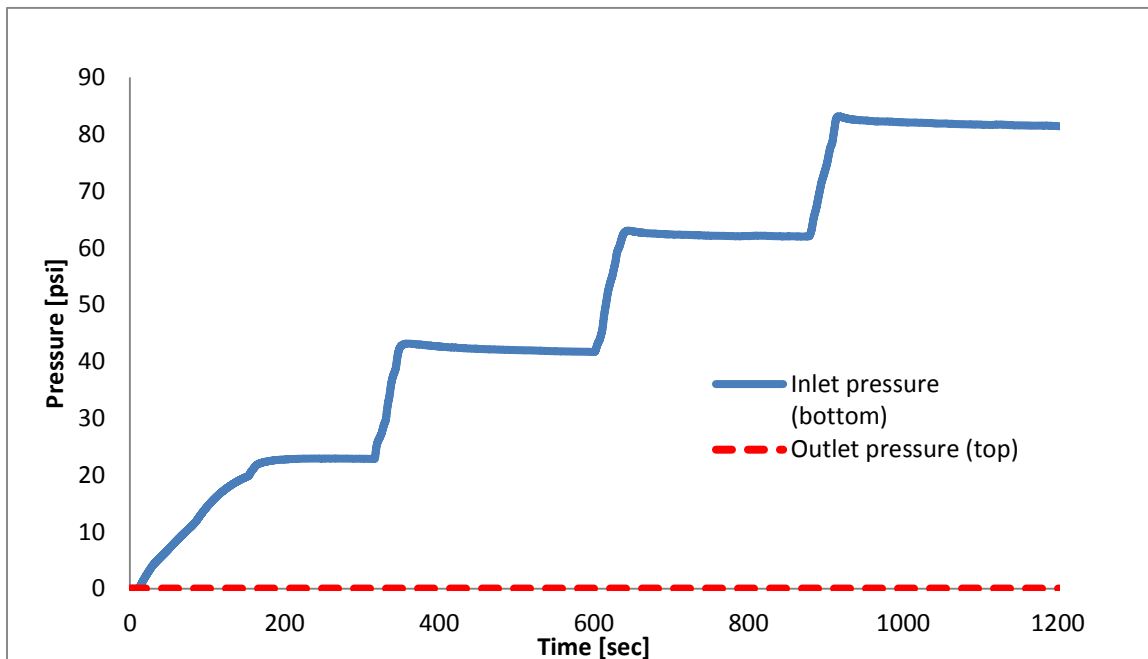


Figure B.5: Multi-rate gas flow-through test data plot recorded 60 days after expansion with the 2% expansion ratio cone. After a gradual increase of 25 psi (172 kPa) in inlet pressure on the gas cylinder every five minutes from 25 psi (172 kPa) to 100 psi (690 kPa), there was no recorded pressure on the outlet transducer, confirming the microannular seal after cement rehydration.



## B.2 Gas Flow-through Test III – 2% Expansion

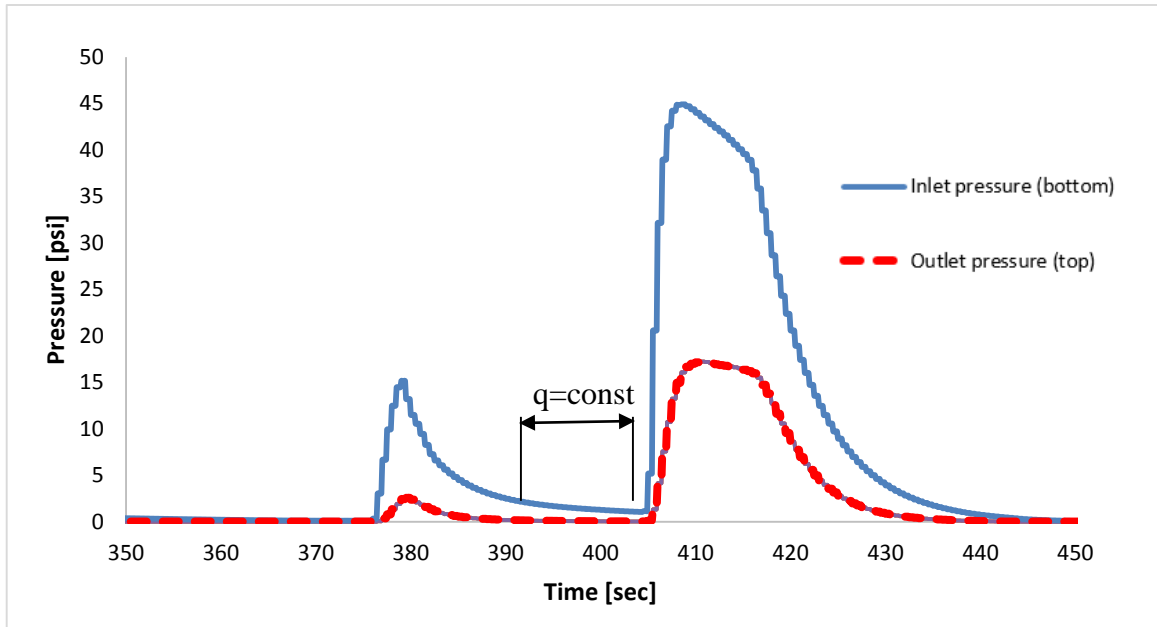


Figure B.6: Gas flow-through test data plot pre-expansion showing registered pressures on both inlet and outlet pressure transducers, which confirmed the microannular gas flow through the composite sample. The starting inlet pressure on the gas cylinder was 15 psi (103 kPa), and it was increased to 50 psi (172 kPa) which resulted in a spike of both pressures on the inlet and outlet ports.

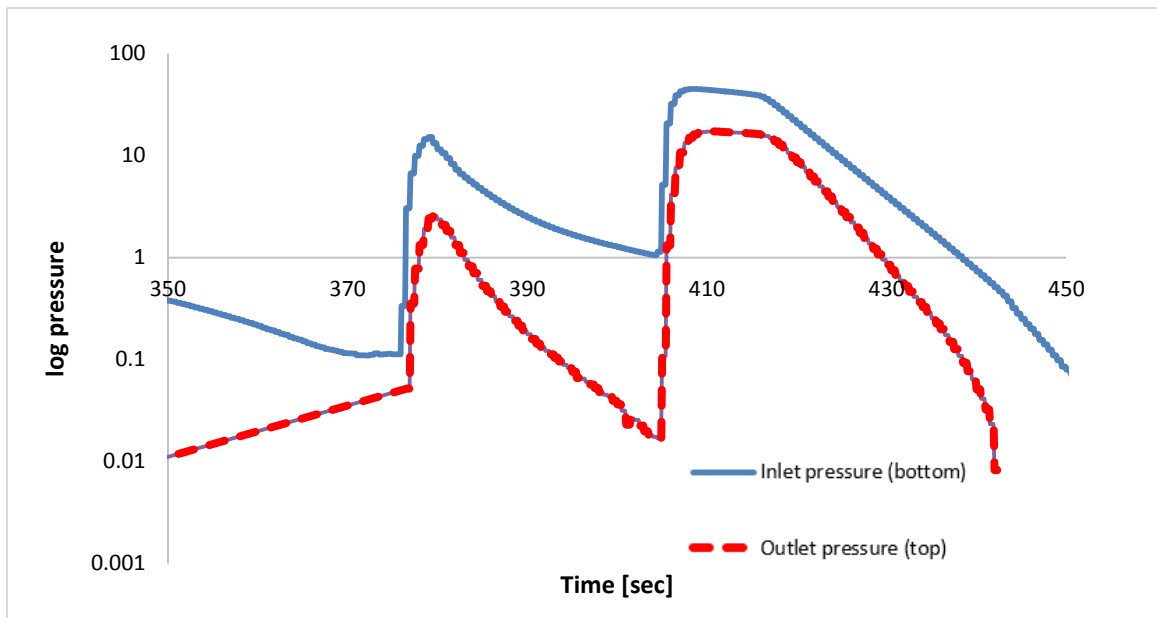


Figure B.7: Gas flow-through test data pre-expansion semi-log plot showing large pressure differential ( $\Delta P$ ) between pressures registered on the inlet and outlet pressure transducers. After calculations, results indicated the microannulus had an effective permeability of 2.31 D.

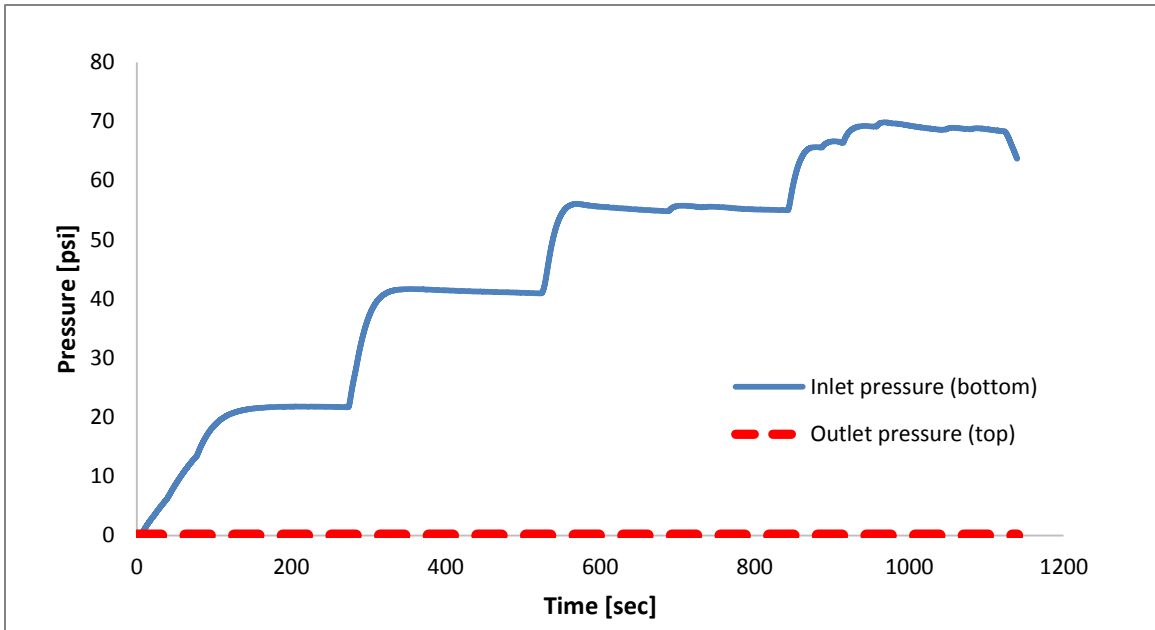


Figure B.8: Multi-rate gas flow-through test data plot recorded immediately after expansion with the 2% expansion ratio cone. After a gradual increase of 25 psi (172 kPa) in inlet pressure on the gas cylinder every five minutes from 25 psi (172 kPa) to 100 psi (690 kPa), there was no recorded pressure on the outlet pressure transducer, indicating successful remediation of the microannular gas flow.

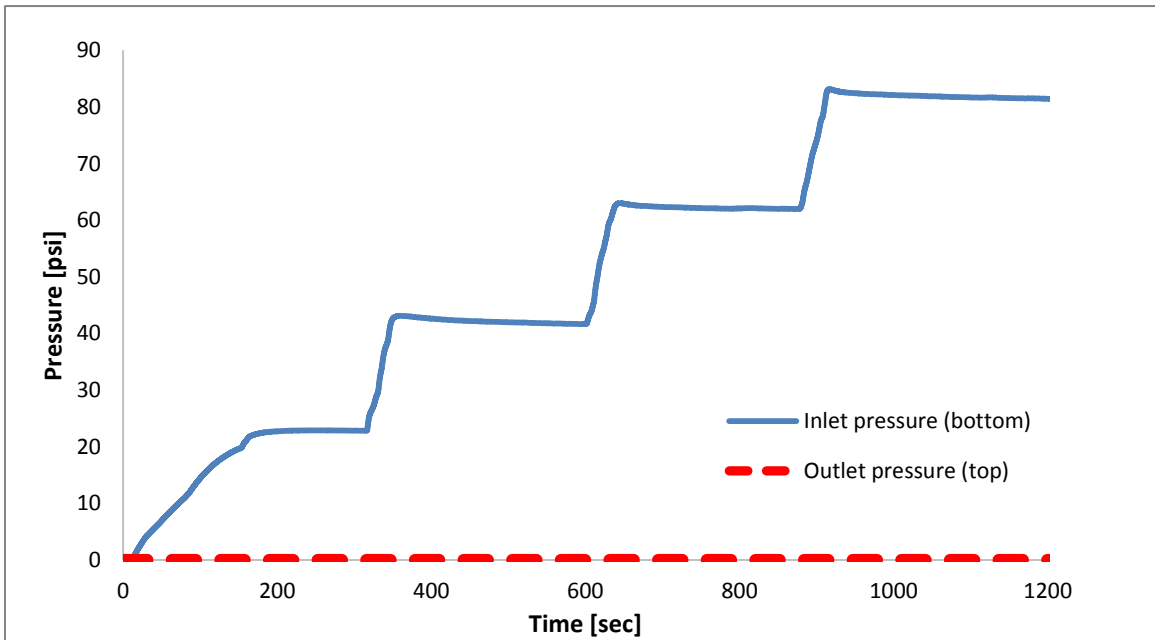


Figure B.9: Multi-rate gas flow-through test data plot recorded 24 hours after expansion with the 2% expansion ratio cone. After a gradual increase of 25 psi (172 kPa) in inlet pressure on the gas cylinder every five minutes from 25 psi (172 kPa) to 100 psi (690 kPa), there was no recorded pressure on the outlet transducer, confirming that the microannular seal was still present.

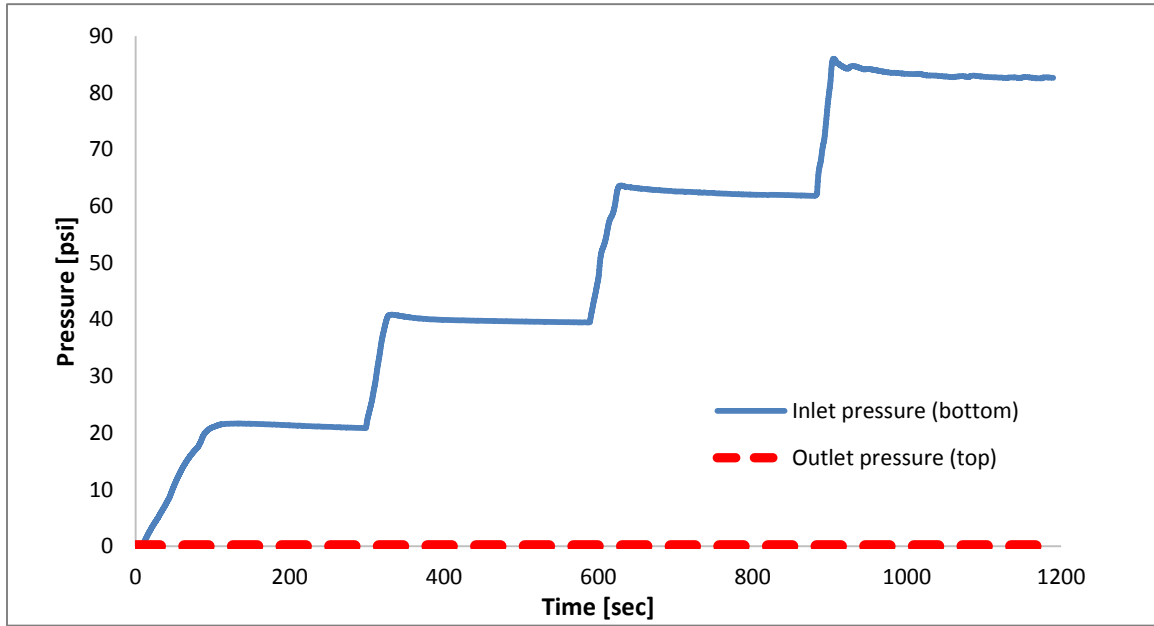


Figure B.10: Multi-rate gas flow-through test data plot recorded 60 days after expansion with the 2% expansion ratio cone. After a gradual increase of 25 psi (172 kPa) in inlet pressure on the gas cylinder every five minutes from 25 psi (172 kPa) to 100 psi (690 kPa), there was no recorded pressure on the outlet transducer, confirming the microannular seal after cement rehydration.

### B.3 Gas Flow-through Test IV – 4% Expansion

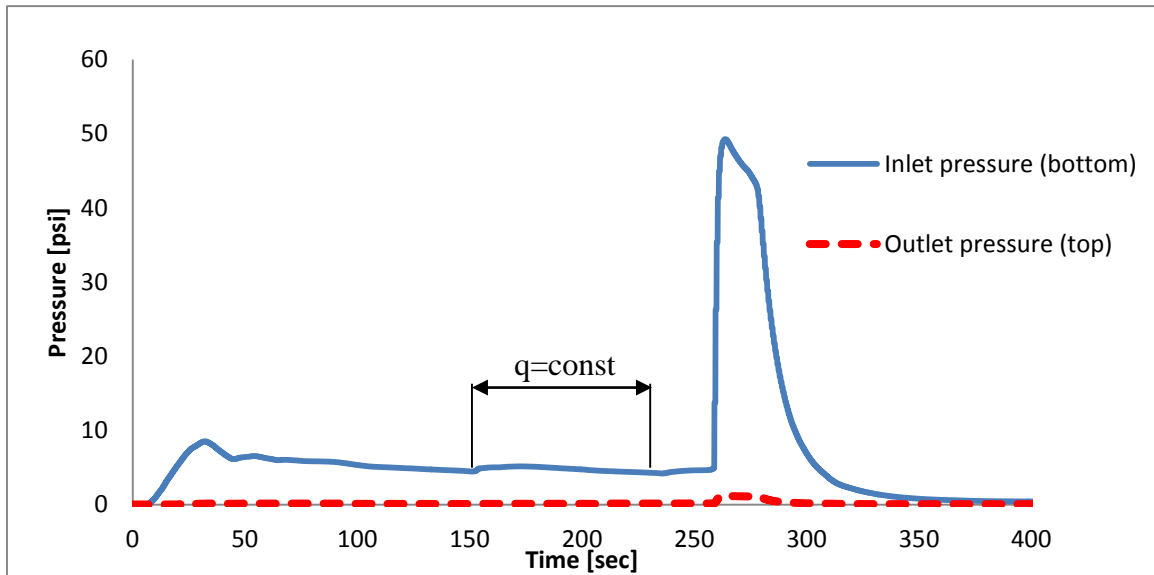


Figure B.11: Gas flow-through test data plot pre-expansion showing registered pressures on both the inlet and outlet pressure transducers, confirming the microannular gas flow through the composite sample. Starting inlet pressure on the gas cylinder was 15 psi (103 kPa), and the flow rate was kept constant in the period from 3-4 minutes of the flow-through test. The inlet pressure was then increased to 50 psi (345 kPa), which resulted in a spike of both pressures on the inlet and outlet ports.

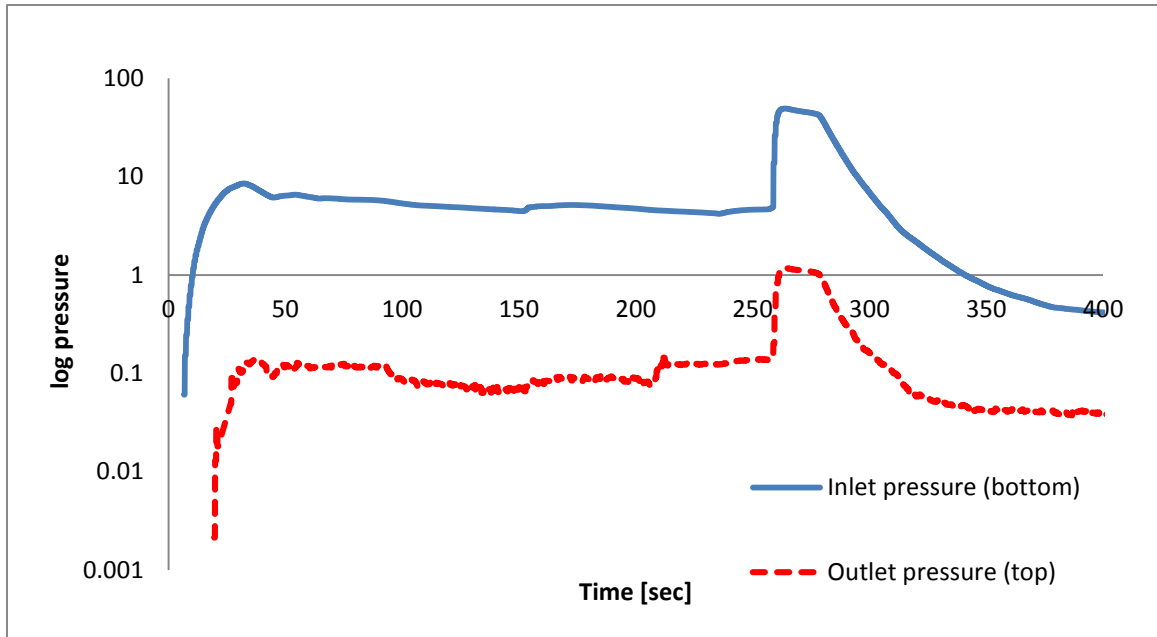


Figure B.12: Gas flow-through test data pre-expansion semi-log plot clearly showing the pressure differential ( $\Delta P$ ) between pressures registered on the inlet and outlet pressure transducers. The pressure differential in the third case was shown to have the largest value, which after calculations indicated a microannulus with an effective permeability of 140 mD.

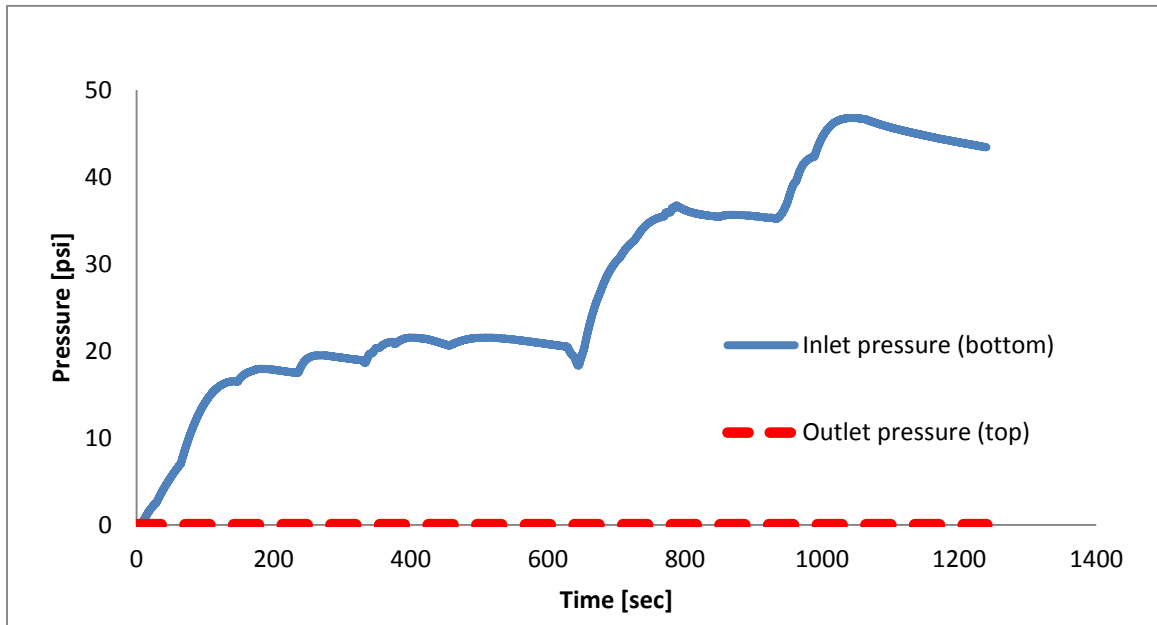


Figure B.13: Multi-rate gas flow-through test data plot recorded immediately after expansion with the 4% expansion ratio cone. After a gradual increase of 25 psi (172 kPa) in inlet pressure on the gas cylinder every five minutes from 25 psi (172 kPa) to 100 psi (690 kPa), there was no recorded pressure on the outlet pressure transducer, indicating successful remediation of the microannular gas flow.

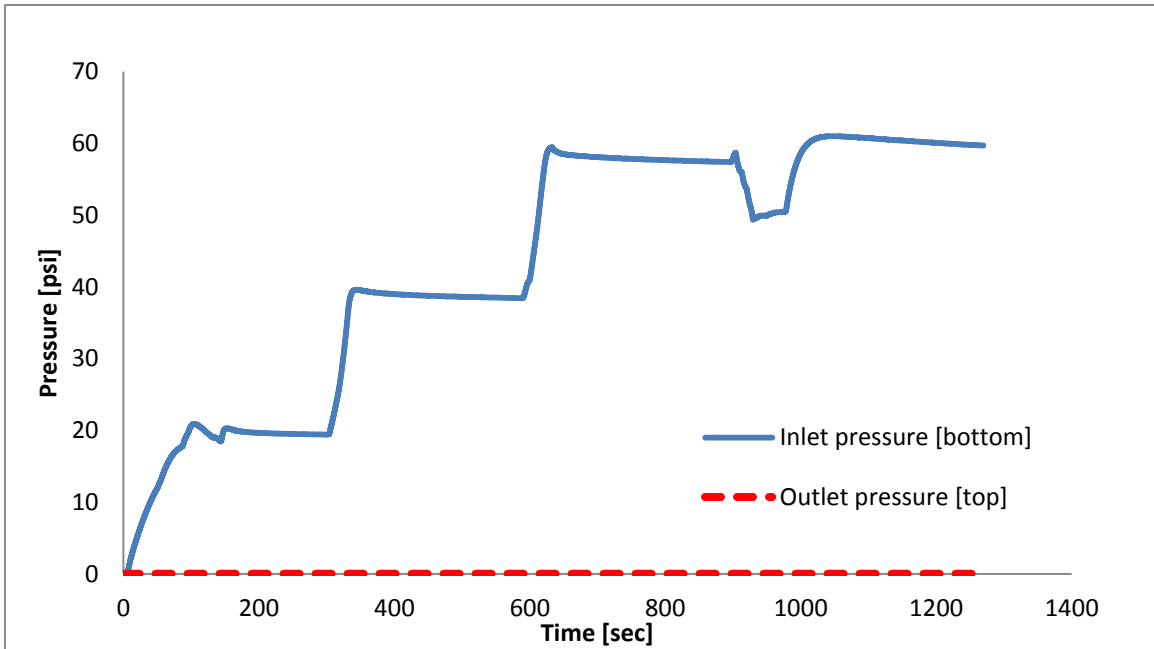


Figure B.14: Multi-rate gas flow-through test data plot recorded 24 hours after expansion with the 4% expansion ratio cone. After a gradual increase of 25 psi (172 kPa) in inlet pressure on the gas cylinder every five minutes from 25 psi (172 kPa) to 100 psi (690 kPa), there was no recorded pressure on the outlet transducer, confirming the presence of a microannular seal.

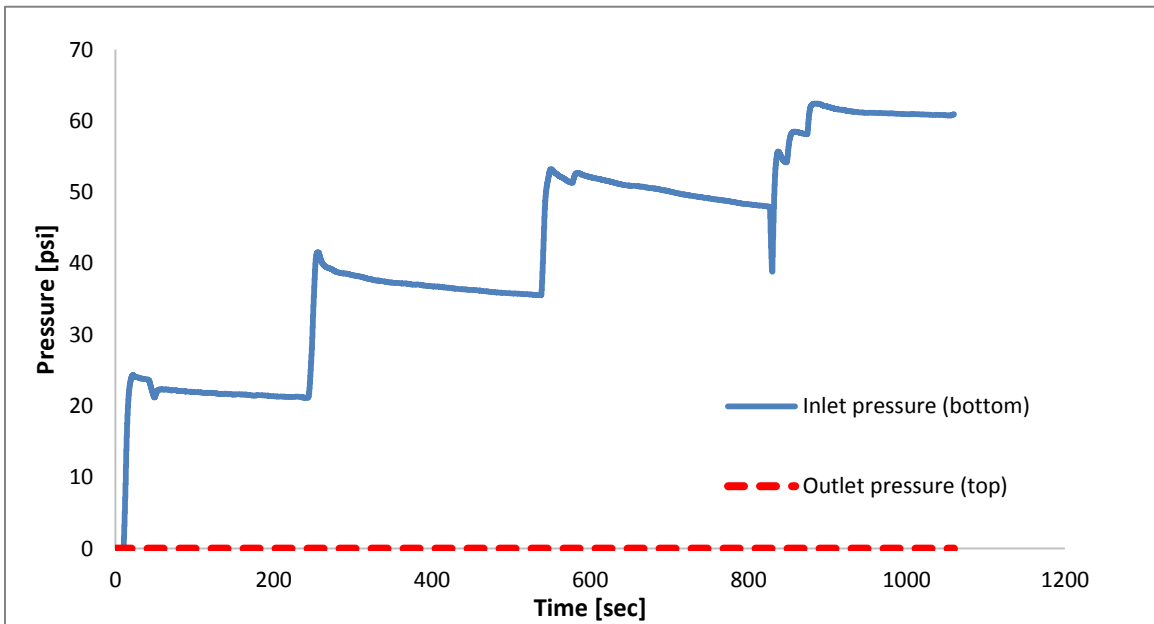


Figure B.15: Multi-rate gas flow-through test data plot recorded 60 days after expansion with the 4% expansion ratio cone. After a gradual increase of 25 psi (172 kPa) in inlet pressure on the gas cylinder every five minutes from 25 psi (172 kPa) to 100 psi (690 kPa), there was no recorded pressure on the outlet pressure transducer, confirming that the microannular seal was still in place.

#### B.4 Gas Flow-through Test V – 8% Expansion

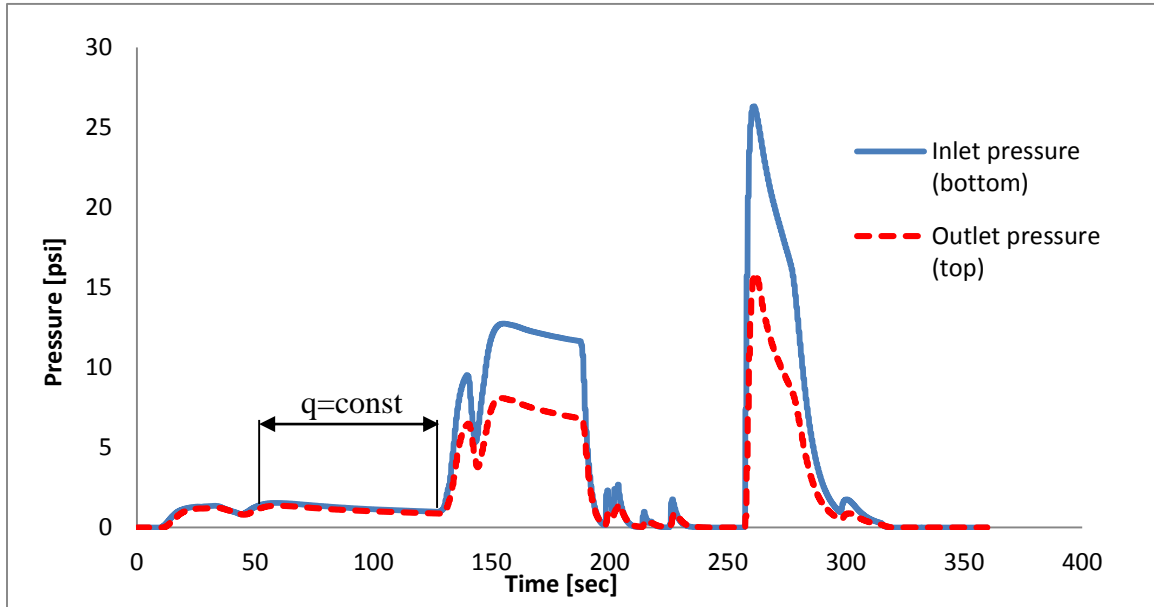


Figure B.16: Gas flow-through test data plot pre-expansion showing registered pressures on both the inlet and outlet pressure transducers, confirming the microannular gas flow through the composite sample. The starting inlet pressure on the gas cylinder was 15 psi (103 kPa), and the flow rate was kept constant in the period of 1-2 minutes of the flow-through test. The inlet pressure was then increased to 25 psi (172 kPa) (first spike) and finally to 50 psi (690 kPa) (second spike).

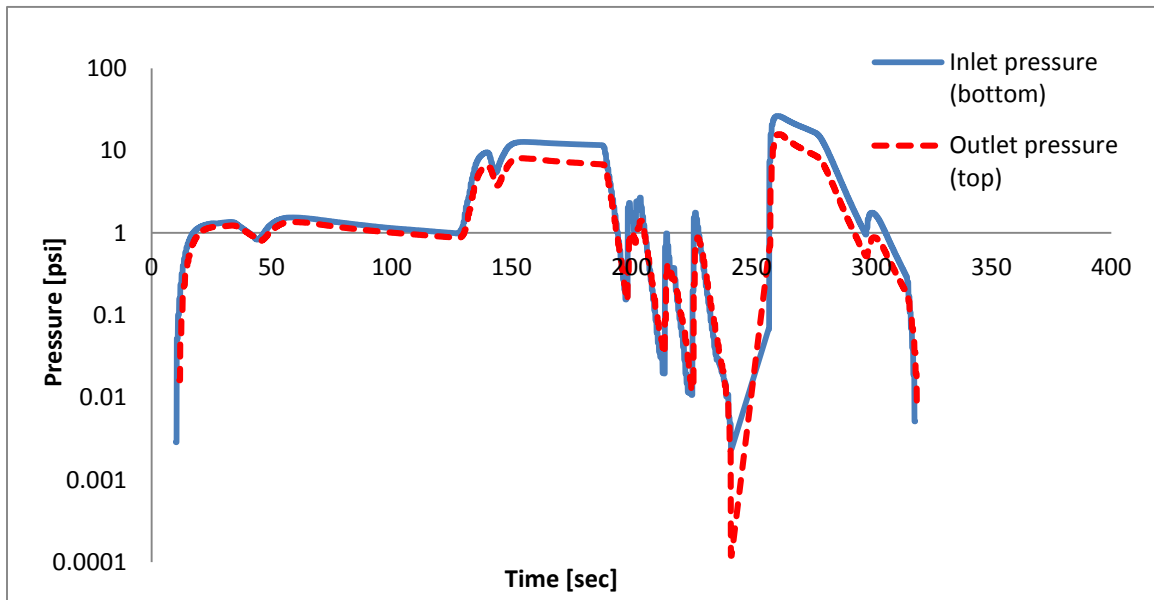


Figure B.17: Gas flow-through test data pre-expansion semi-log plot showing very small pressure differential ( $\Delta P$ ) between pressures registered on inlet and outlet pressure transducers. The pressure differential recorded in this case was the smallest value of all the samples, indicating the existence of a microannulus with the largest effective permeability (7.04 D).

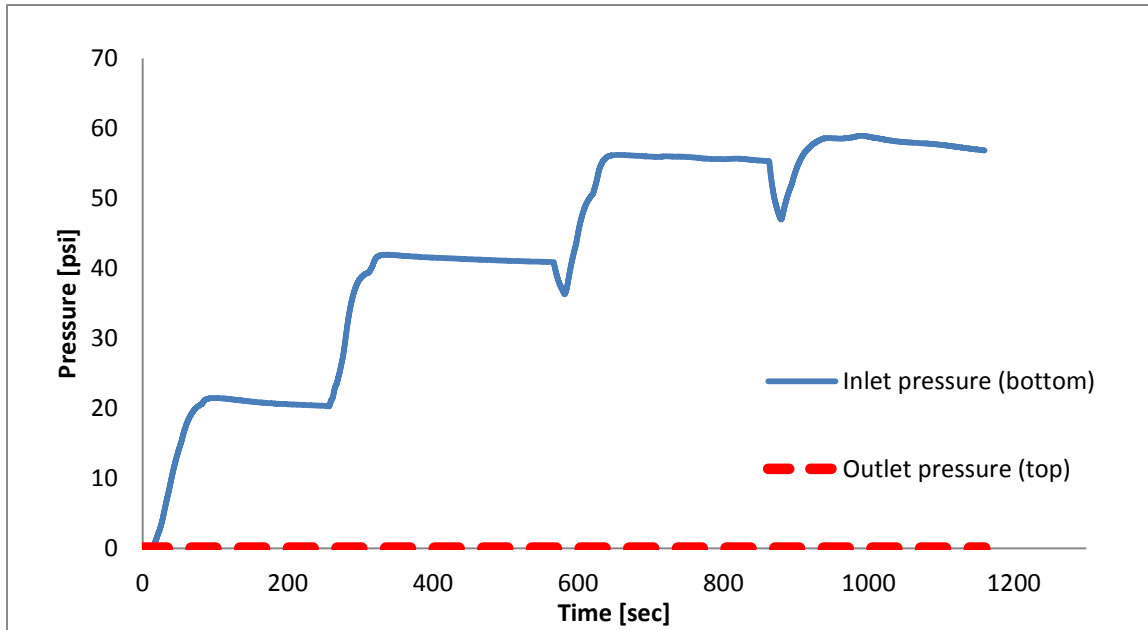


Figure B.18: Multi-rate gas flow-through test data plot recorded immediately after expansion with the 8% expansion ratio cone. After a gradual increase of 25 psi (172 kPa) in inlet pressure on the gas cylinder every five minutes from 25 psi (172 kPa) to 100 psi (690 kPa), there was still pressure recorded on the outlet pressure transducer of 0.214 psi (1.5 kPa), which can be classified as negligible.

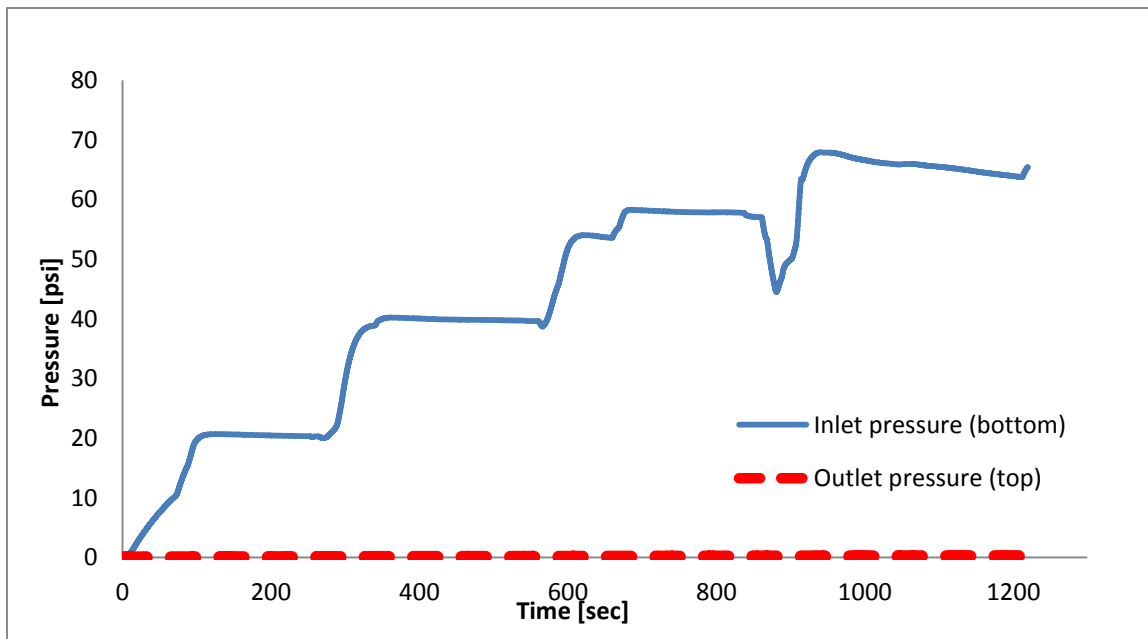


Figure B.19: Multi-rate gas flow-through test data plot recorded 24 hours after expansion with the 8% expansion ratio cone. After a gradual increase of 25 psi (172 kPa) in inlet pressure on the gas cylinder every five minutes from 25 psi (172 kPa) to 100 psi (690 kPa), there was no pressure recorded on the outlet pressure transducer, indicating successful remediation of the microannular flow after a 24-hour period of cement rehydration.

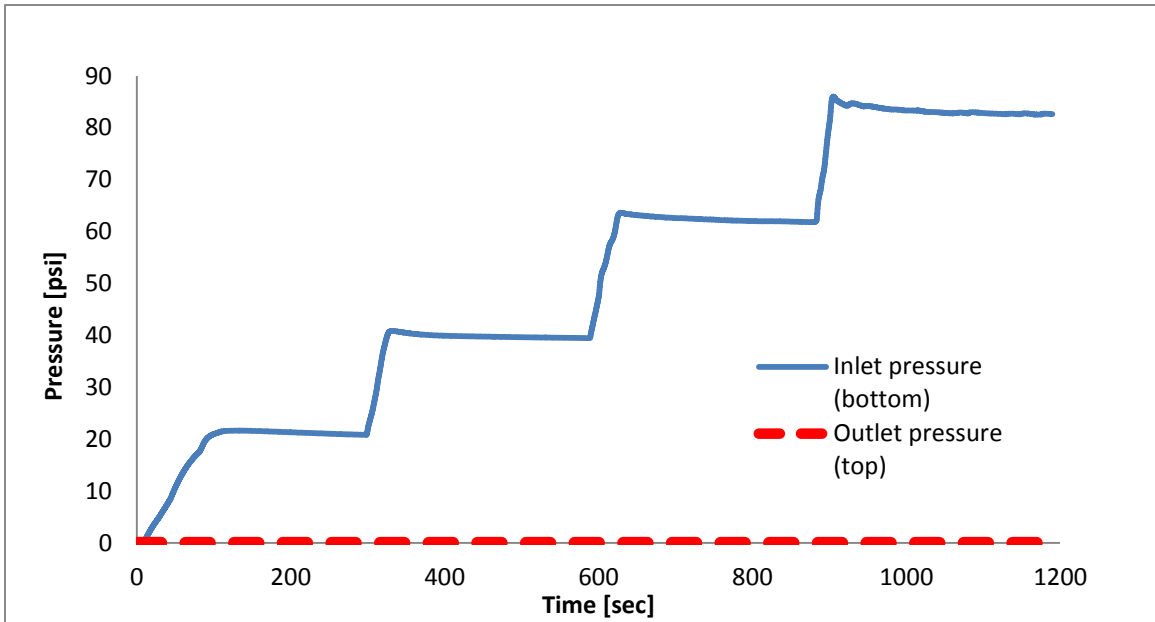


Figure B.20: Multi-rate gas flow-through test data plot recorded 60 days after expansion with the 8% expansion ratio cone. After a gradual increase of 25 psi (172 kPa) in inlet pressure on the gas cylinder every five minutes from 25 psi (172 kPa) to 100 psi (690 kPa), there was no recorded pressure on the outlet transducer, confirming the seal of the microannular gas flow.

### B.5 Gas Flow-through Test VI – 8% Expansion

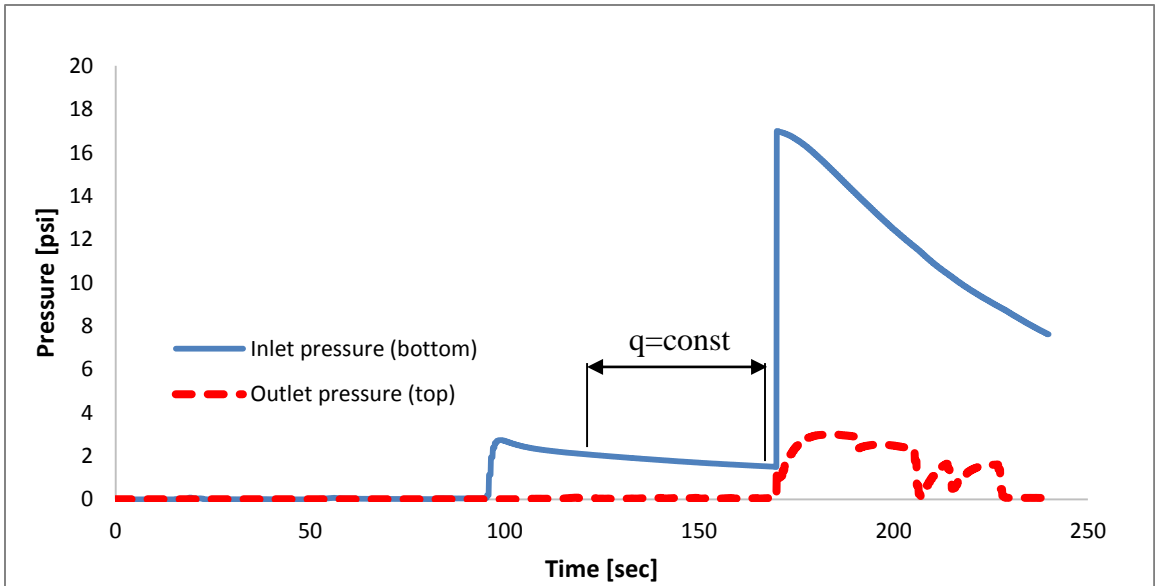


Figure B.21: Gas flow-through test data plot pre-expansion showing registered pressures on both the inlet and outlet pressure transducers, confirming the microannular gas flow through the composite sample. The starting inlet pressure on the gas cylinder was 15 psi (103 kPa), and the flow rate was kept constant in the period of 2-3 minutes of the flow-through test. The inlet pressure was then increased to 25 psi (172 kPa), which resulted in a spike of both pressures on inlet and outlet ports.



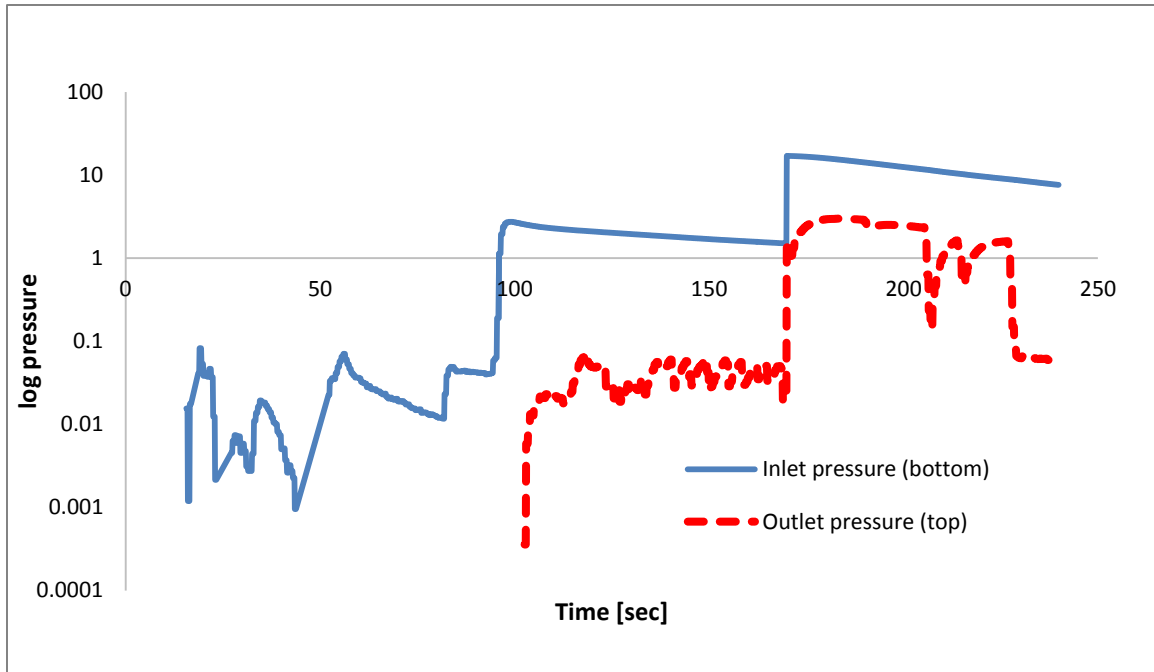


Figure B.22: Gas flow-through test data pre-expansion semi-log plot clearly showing a pressure differential ( $\Delta P$ ) between pressures registered on the inlet and outlet pressure transducers. After calculations, the effective permeability of the microannulus was found to be 660 mD.

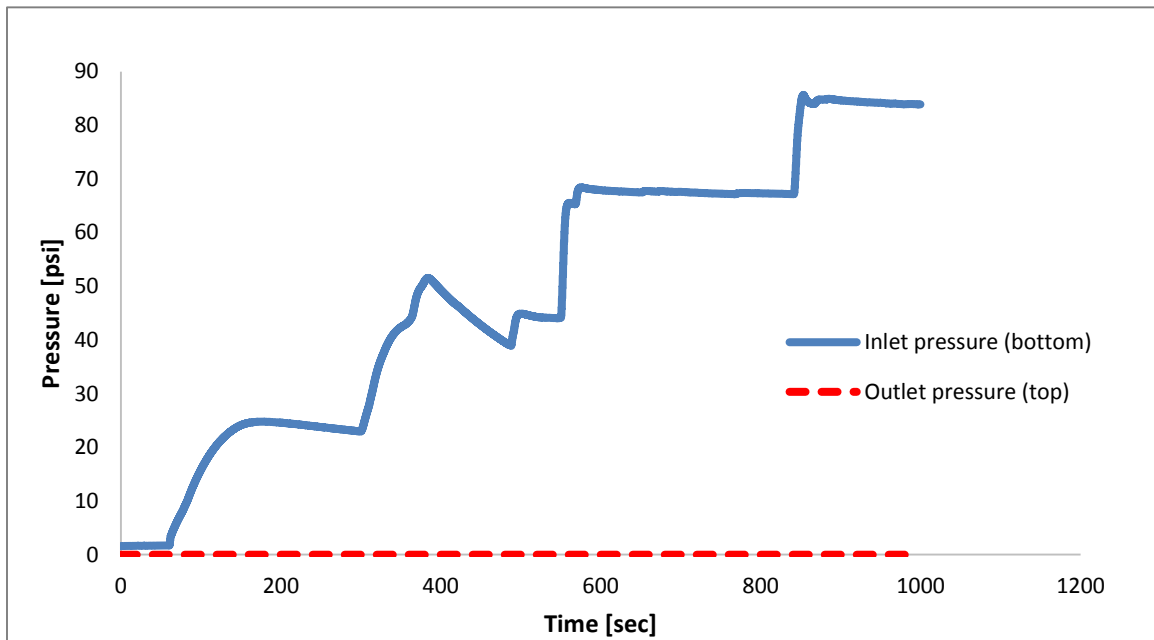


Figure B.23: Multi-rate gas flow-through test data plot recorded immediately after expansion with the 8% expansion ratio cone. After a gradual increase of 25 psi (172 kPa) in inlet pressure on the gas cylinder every five minutes from 25 psi (172 kPa) to 100 psi (690 kPa), there was no recorded pressure on the outlet pressure transducer, indicating successful remediation of the microannular gas flow.

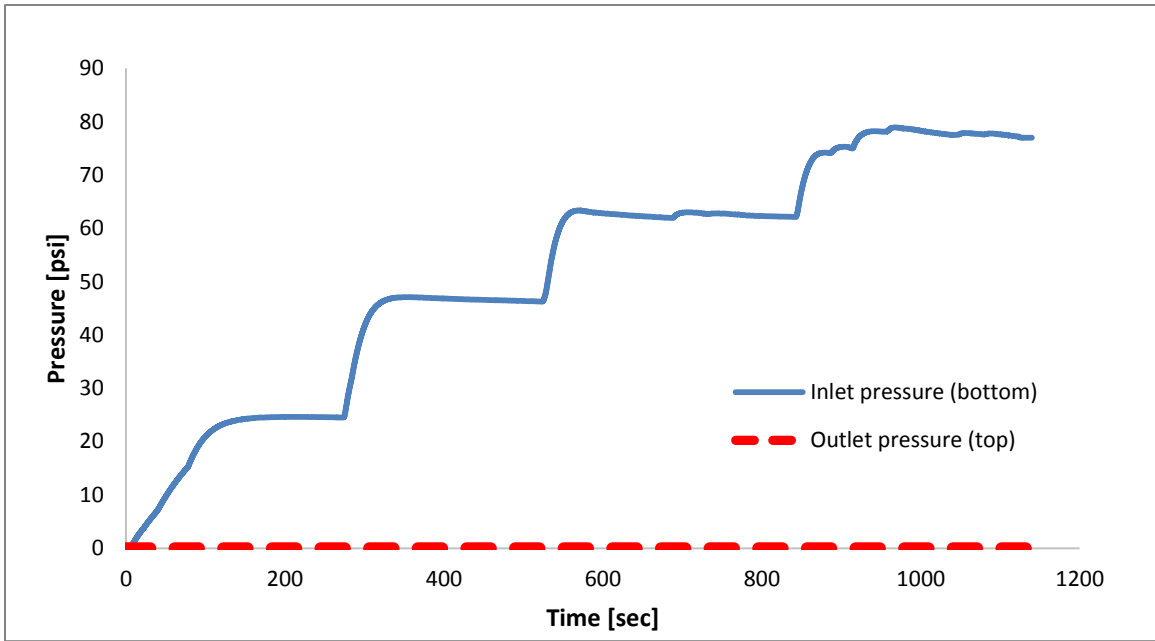


Figure B.24: Multi-rate gas flow-through test data plot recorded 24 hours after expansion with the 8% expansion ratio cone. After a gradual increase of 25 psi (172 kPa) in inlet pressure on the gas cylinder every five minutes from 25 psi (172 kPa) to 100 psi (690 kPa), there was no recorded pressure on the outlet pressure transducer, confirming that the microannular seal was still in place.

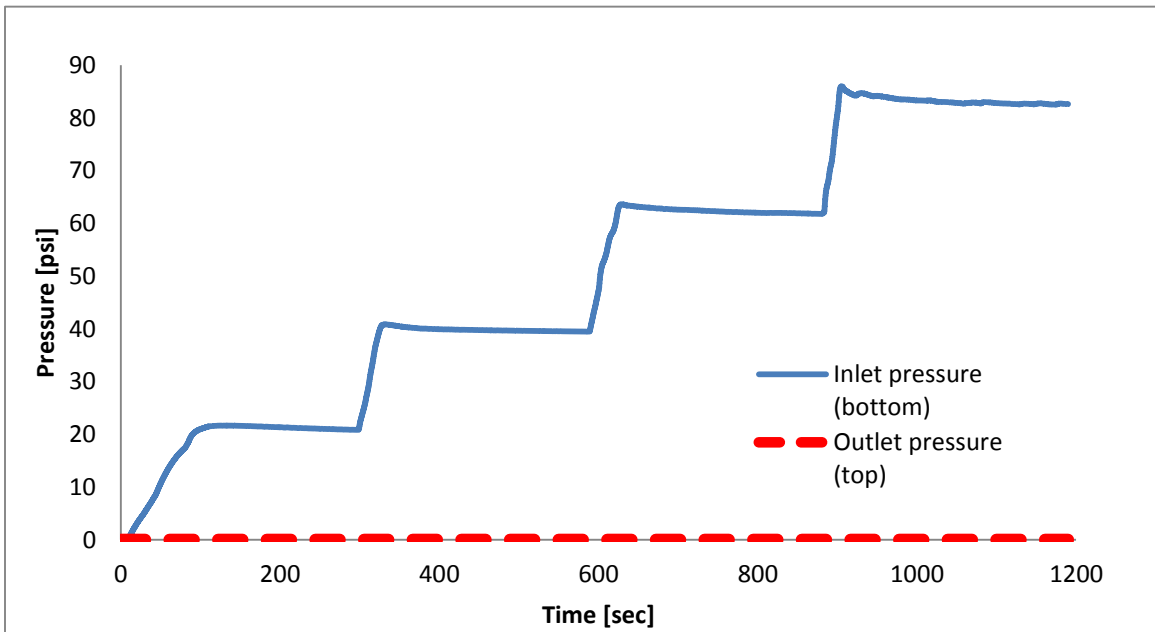


Figure B.25: Multi-rate gas flow-through test data plot recorded 60 days after expansion with the 8% expansion ratio cone. After a gradual increase of 25 psi (172 kPa) in inlet pressure on the gas cylinder every five minutes from 25 psi (172 kPa) to 100 psi (690 kPa), there was no recorded pressure on the outlet transducer, confirming the seal of the microannular gas flow.

**APPENDIX C**  
**EXPANSION CALCUALTIONS (SI UNITS)**

Table C.1: Force measurements obtained during expansion and calculated axial stresses. Values are for expansions with pipe only and for composite cement sample (SI units).

<b>Actual Expansion Ratio [%]</b>	<b>Cone OD [cm]</b>	<b>Fe - pipe [kN]</b>	<b><math>\sigma_z</math> – pipe [GPa]</b>	<b>Fe – sample [kN]</b>	<b><math>\sigma_z</math> – sample [psi]</b>
1.46	5.56	93.03	17.27	134.78	25.01
3.45	5.67	168.20	31.21	205.64	38.16
7.43	5.89	359.82	73.45	603.10	111.92

## APPENDIX D

### THERMOGRAVIMETRIC ANALYSIS

Results of the control sample showed weight loss in portlandite mineral of over 5%. Knowing that approximately 25% of total portlandite weight is being lost in that endothermal region, this means that there was 21% of portlandite in the cement sample prior to expansion. The weight loss below and up to 302°F (150°C) was 6%, which contained endothermal peaks of water, ettringite, gypsum and C-S-H. The last endothermal peak corresponds to weight percentage of calcite. The presence of calcite can be ascribed to carbonation of the sample during transport and preparation.

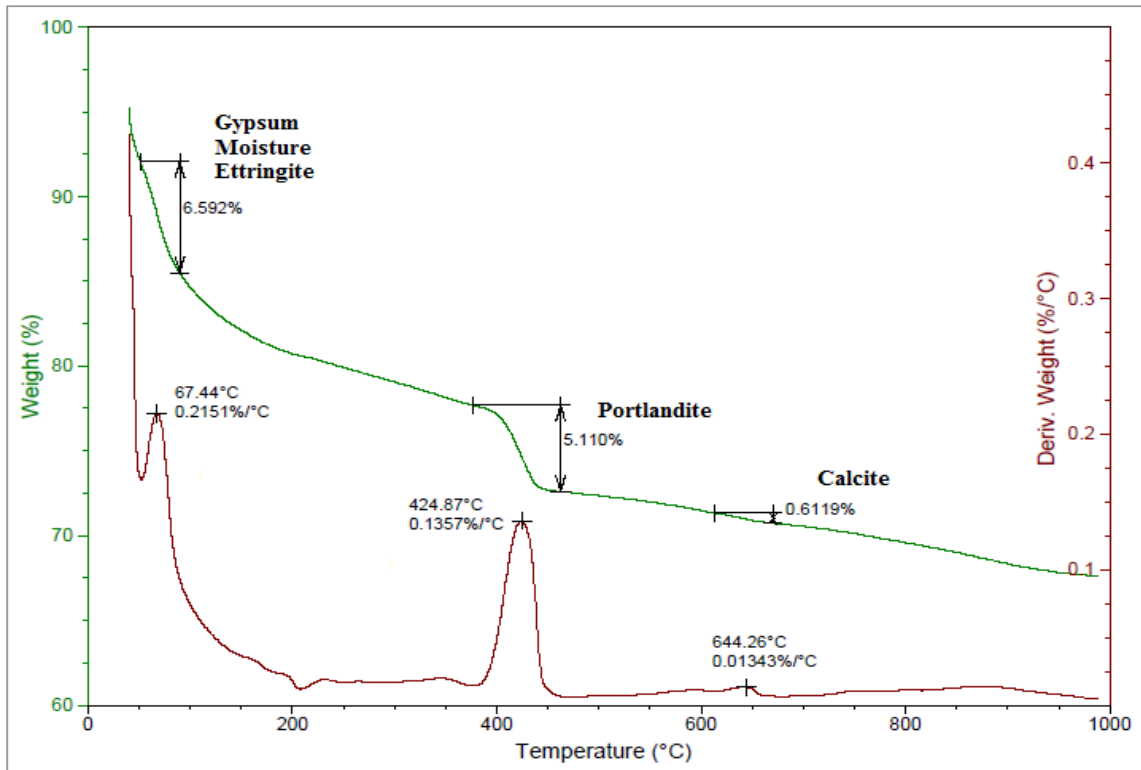


Figure D.1: Plot of TGA for control sample. The green (upper) line is showing weight percentage lost, while the red line shows endothermal peaks (°C) of the weight percentage lost per unit of heat. In the range of 122°F-302°F (50-150°C), the total weight loss was 6.5%. This loss corresponds to the amount of moisture, and mineral phases of gypsum, ettringite and C-S-H in the sample. The next endothermal peak at 797°F (425°C) is portlandite peak. The weight loss of 5% indicates that there was initially 21% portlandite in the control sample. Last endothermal peak at 1191°F (644°C) is calcite peak and small weight loss of 0.6% indicates minor presence of calcite due to carbonation of the sample.

Thermal analysis of the sample which was expanded at 4% expansion ratio showed weight losses at two different endothermal peaks under 302°F (150°C) (8% and 5%) meaning that both concentration of moisture and mineral group of ettringite, gypsum and C-S-H did not change significantly comparing to the control sample. The observed weight loss in portlandite mineral of 4.1%, indicated that the portlandite decreased to 17% after 4% expansion. Minor presence of calcite (0.7% weight loss) is negligible.

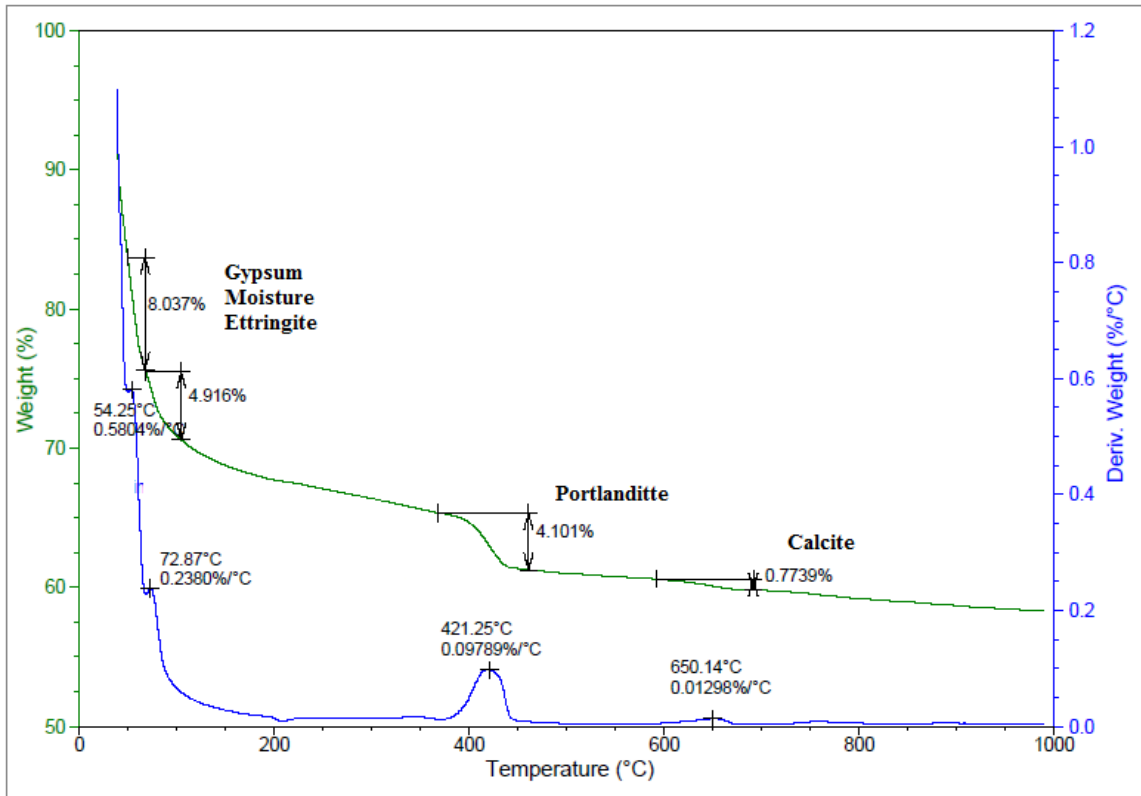


Figure D.2: TGA plot of cement sample after 4% expansion. The green (upper) line is showing weight percentage lost, while the blue line shows endothermal peaks (°C) of the weight percentage lost per unit of heat. Two distinctive peaks observed in the range of 122-302°F (50-150°C) correspond to the weight losses of moisture (8%) and mineral phases of gypsum, ettringite and C-S-H (5%). The portlandite peak at 790°F (421°C) showed weight loss of 4% indicating that there was 17% portlandite in the sample expanded with 4% expansion ratio cone. Last endothermal peak at 1202°F (650°C), corresponding to the calcite peak, showed weight loss of 0.77%, indicating minor presence of calcite due to carbonation of the cement sample during preparation.

Sample expanded with 8% expansion ratio cone had significantly different results than control and 4% expansion samples. Weight loss of 45% in minerals with endothermal peaks below 302°F (150°C) was observed, which corresponds to presence of moisture, gypsum, ettringite and/or C-S-H minerals. Weight loss of portlandite was registered to be 3.2%, indicating that after 8% expansion the concentration of this mineral decreased to 13% (compared to 25% in control sample).

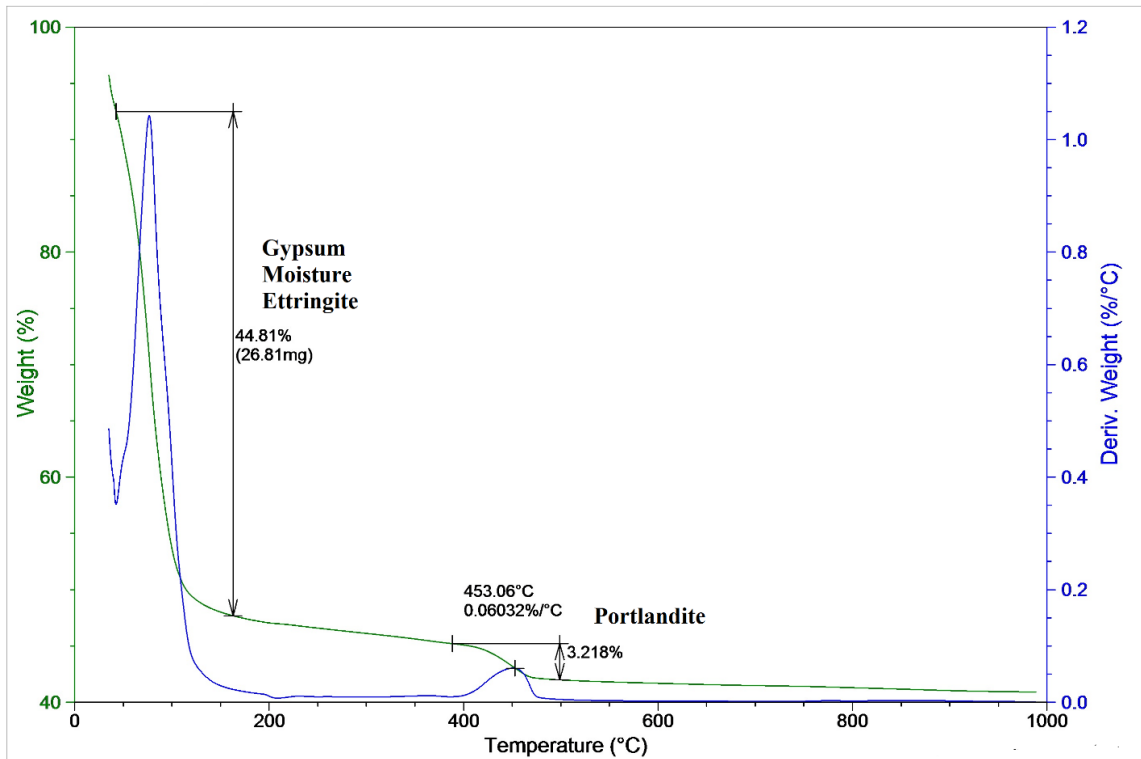


Figure D.3: TGA plot for cement sample expanded at 8% expansion ratio. The green line is showing weight percentage lost, while the blue line shows endothermal peaks (°C) of the weight percentage lost per unit of heat. In the range of 122-302°F (50-150°C), significant weight loss of 45% corresponds to the large amount of moisture within the sample, and also mineral phases of gypsum, ettringite and C-S-H. The next endothermal peak at 847°F (453°C) showed portlandite weight loss of 3.2% indicating decrease of the mineral from 25% to 13% after expansion with 8% expansion ratio cone.

**APPENDIX E**  
**FORCE AND STRESS CALCULATIONS DURING EXPANSION**

The balance of forces during expansion is shown on the figure below. In order to obtain the radial force ( $F_r$ ) experienced by cement sheath, contact force ( $F_c$ ) had to be calculated first from contact stress ( $\sigma_c$ ) [75]. The friction coefficient ( $\mu$ ) was taken to be 0.05 based on testing conducted with the used lubricant.

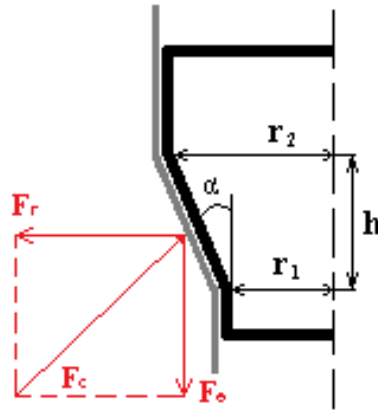


Figure E.1: Forces applied on the pipe during expansion.  $F_e$  represents the expansion force,  $F_c$  the contact force, and  $F_r$  the radial force.

$$\sigma_c = \frac{F_e}{\pi(r_2^2 - r_1^2)(1 + \mu(\cot \alpha))} \quad (E.1)$$

$\sigma_c$  – contact stress [psi]

$F_e$  – expansion force [lbf]

$r_1$  – radius of unexpanded section [in]

$r_2$  – radius of expanded section [in]

$\alpha$  – expansion angle [°]

$\mu$  – friction coefficient

After obtaining the contact stress, contact force was calculated with the following equation:

$$F_c = \sigma_c \cdot A_c \quad (E.2)$$

$F_c$  – contact force [lbf]

$A_c$  – surface area of the cone

Surface area of the cone ( $A_c$ ) is given with equation:

$$A_c = \pi(r_1 + r_2)\sqrt{(h^2 + (r_2 - r_1)^2)} \quad (\text{E.3})$$

where  $h$  is the height of the expansion area.

Finally the radial force ( $F_r$ ) is obtained from the equation of force balance:

$$F_r = \sqrt{(F_c^2 - F_e^2)} \quad (\text{E.4})$$

The radial stress ( $\sigma_r$ ) can be calculated with:

$$\sigma_r = \frac{F_r}{A_r} \quad (\text{E.5})$$

where  $A_r$  is the area of radial action:

$$A_r = 2\pi r_1 h \quad (\text{E.6})$$

The results of the force and stress calculations during expansion of the composite sample and the inner pipe alone, are shown in the following tables.

Table E.1: Results of force and stress calculations during expansion of the composite sample. Contact force and stress ( $F_c$ ,  $\sigma_c$ ) are used in calculations of radial force and stress ( $F_r$ ,  $\sigma_r$ ).

<b>Expansion ratio [%]</b>	<b><math>\sigma_c</math> [psi]</b>	<b><math>F_c</math> [lbf]</b>	<b><math>\sigma_r</math> [psi]</b>	<b><math>F_r</math> [lbf]</b>
2	7,652.7	12,588.3	7,756.4	12,269.5
4	11,676.1	27,598.5	12,129.7	27,262.2
8	34,242.7	124,847.8	36,649.8	124,210.8



Table E.2: Results of force and stress calculations during expansion of the inner pipe only. Contact force and stress ( $F_c$ ,  $\sigma_c$ ) are used in calculations of radial force and stress ( $F_r$ ,  $\sigma_r$ ).

<b>Expansion ratio [%]</b>	<b><math>\sigma_c</math> [psi]</b>	<b><math>F_c</math> [lbf]</b>	<b><math>F_r</math> [lbf]</b>	<b><math>\sigma_r</math> [psi]</b>
2	5,282.6	8,689.6	8,469.6	5,354.2
4	9,550.2	22,573.6	22,298.6	9,921.3
8	22,473.8	81,938.7	81,520.6	24,053.6

Table E.3: The difference in radial forces and stresses accounted for the cement sheath behind the pipe.

<b><math>\Delta F_r</math> [lbf]</b>	<b><math>\Delta \sigma_r</math> [psi]</b>
3,799.9	2,402.2
4,963.7	2,208.5
42,690.2	12,596.2

Based on these calculations the contact stress seems not to exceed the yield stress of the pipe (35,000 psi, 241 MPa), but the pipe clearly plastically deforms during expansion. This discrepancy is due to assumption that the entire contact area of the cone ( $A_c$ ) is in contact with the pipe during expansion. The contact area is in reality much smaller (even below 20% of the entire landing area) and this would create a contact stress much higher than 35,000 psi (241 MPa), thus yielding the pipe into the plastic region.

**APPENDIX F**  
**DERIVATION OF THE SLOT SIZE EQUATION**

The slot size of the flow can be correlated from permeability. From Buckingham's equation for flow through slots of fine clearance, making the assumption of slot porosity of 1 [76]:

$$q_f = \frac{A \cdot w^2 \Delta P}{12 \mu L} \quad (\text{F.1})$$

$q_f$ – flow through a slot [m <sup>3</sup> /s]	$A$ – area of flow [m <sup>2</sup> ]
$w$ – slot size [m]	$\Delta P$ – pressure differential [Pa]
$\mu$ - viscosity of the fluid [PaS]	$L$ – length of flow path [m]

from Darcy's equation for flow through porous media

$$q = -\frac{kA \Delta P}{\mu L} \quad (\text{F.2})$$

Where  $k$  is permeability in m<sup>2</sup>, we can then correlate the slot size with permeability:

$$k = \frac{w^2}{12} \quad (\text{F.3})$$

**APPENDIX G**  
**PREPARATION OF CEMENT THIN SECTIONS AND SAMPLES FOR**  
**MICROINDENTATION**

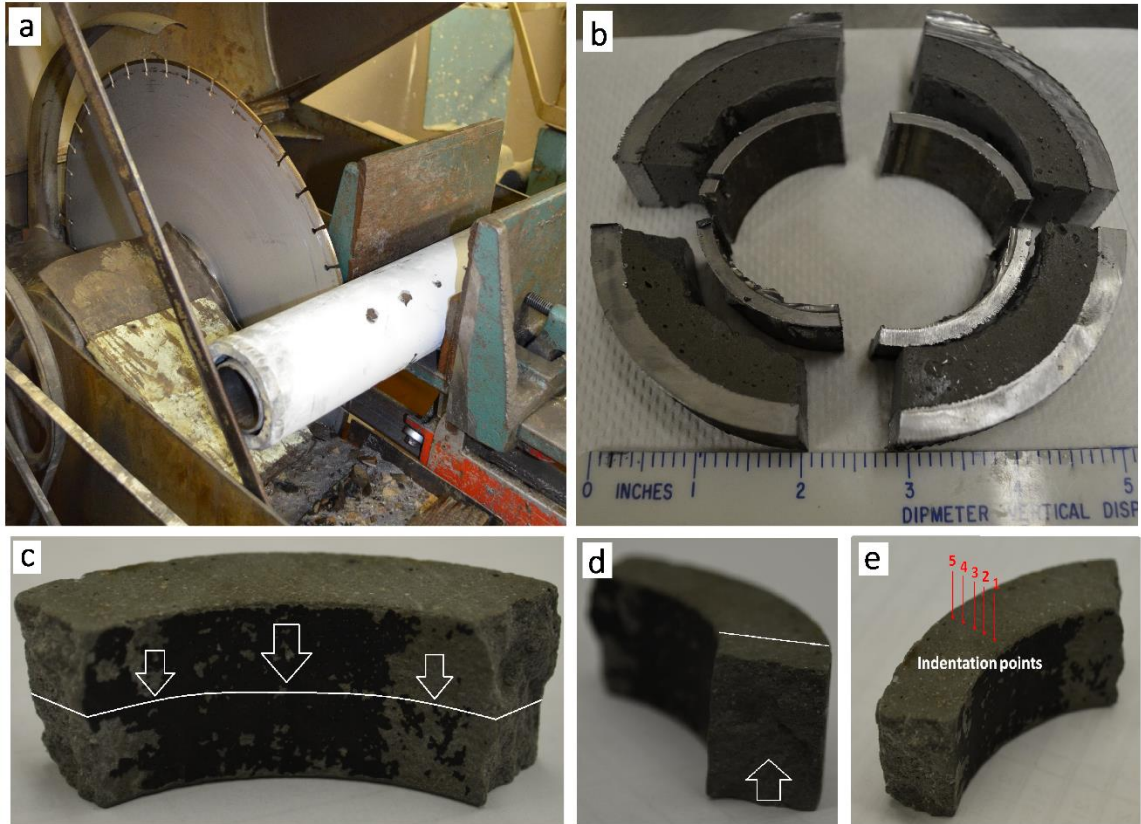


Figure G.1: Sample preparation for cement thin sections and microindentation. a. cutting of the composite sample into disks; b. cut disk into quarters and removing the cement sheath out of the composite disk; c. orientation of the horizontal (top) cut for thin sections; d. orientation for side (vertical) thin section cut; e. five indentation spots for microhardness measurements.

**APPENDIX H**  
**API CLASS H CEMENT - COMPOSITION**

Table H.1: Results of the used class H cement clinker analysis performed by LaFarge.

Silica Dioxide (SiO <sub>2</sub> )	21.4%
Aluminum Oxide (Al <sub>2</sub> O <sub>3</sub> )	2.7%
Ferric Oxide (Fe <sub>2</sub> O <sub>3</sub> )	4.5%
Calcium Oxide (CaO)	63.6%
Magnesium Oxide (MgO)	2.6%
Sulphur Trioxide (SO <sub>3</sub> )	2.9%
Loss on Ignition	0.83%
C <sub>4</sub> AF+2C <sub>3</sub> A	12.87%
Free Lime (XRD value)	0.96%
Tricalcium Silicate (C <sub>3</sub> S)	63%
Tricalcium Aluminate	0%
Total Alkali as Sodium Oxide	0.23%
Insoluble Residue	0.37%

## APPENDIX I

### LIST OF PUBLICATIONS AND PRESENTATIONS

Kupresan, D., Dussenova, D, Radonjic, M. 2011. *Experimental Investigation of Improved Cement Isolation by Expandable Technology*. Presented at Expandable Tubular Forum, Houston, Texas, 4-5 November.

Kupresan, D., Heathman, J., Tao, T., Radonjic, M. 2013. *Development of a New Physical Model for Experimental Assessment of Expandable Casing Technology Effect on Wellbore cement Integrity*. Paper OMAE 10846 presented at 32<sup>nd</sup> International Conference on Ocean, Offshore and Arctic Engineering, Nantes, France, 9-14 June.

Radonjic, M., Heathman, J., Kupresan, D. 2013. *Analysis of Defect-Free Wellbore Cement Microstructure Created by In-Situ Mechanical Manipulation*. Paper presented at 21<sup>st</sup> Annual International Conference on Composites/Nano Engineering, Tenerife, Spain, 21-27 July.

Kupresan, D., Heathman, J., Radonjic, M. 2013. *Experimental Assessment of Casing Expansion as a Solution for Microannular Gas Migration*. Second place at student session oral presentation competition at 17<sup>th</sup> Annual Gulf of Mexico Deepwater Technical Symposium, New Orleans, Louisiana, 21-22 August.

Kupresan, D., Heathman, J., Radonjic, M. 2013. *In-situ Mechanical Manipulation of Wellbore Cements as a Solution to Leaky Wells*. Presented at 2013 AGU Fall Meeting, San Francisco, California, 9-13 December.

Kupresan, D., Heathman, J., Radonjic, M. 2013. *Application of a New Physical Model of Expandable Casing Technology in Mitigation of Wellbore Leaks*. Journal of Canadian Energy Technology & Innovation (CETI), Vol. 1, No. 5, December.

Kupresan, D., Heathman, J., Radonjic, M. 2014. *Experimental Assessment of Casing Expansion as a Solution to Microannular Gas Migration*. Paper SPE 168056 presented at IADC/SPE Drilling Conference, Fort Worth, Texas, 4-6 March (this paper has also been submitted for peer review in SPE Drilling and Completion Journal).

Radonjic, M., Kupresan, D. 2014. *Remediation of Gas Leakage by Mechanical Manipulation of Wellbore Cement*. Abstract accepted for 48<sup>th</sup> US Rock Mechanics/Geomechanics Symposium, Minneapolis, Minnesota, 1-4 June.

Radonjic, M., Oyibo, A., Kupresan, D. 2014. *The Use of Expandable Casing Technology as a New Remediation Tool for Microannular Gas Migration*. Abstract accepted for 5<sup>th</sup> International Conference on Porous Media and Its Applications in Science, Engineering and Industry, Kona, HI, 22-27 June.

## VITA

Darko Kupresan was born in Belgrade, Serbia on June 23<sup>rd</sup> 1986. He received his Bachelor of Science degree in Petroleum Engineering from University of Belgrade, Faculty of Mining and Geology. After obtaining his B.Sc. degree in 2011 he then proceeded to Louisiana State University where he pursued his Master of Science degree in Petroleum Engineering. He worked on a Shell sponsored project investigating the impact of expandable casing technology on cement and remediation of microannular gas flow. Publications and presentations have been listed in Appendix G.